



**HAL**  
open science

# Structural and Morphological modification of TiO<sub>2</sub> doped metal ions and investigation of photo-induced charge transfer processes

Jesus Vargas Hernandez

► **To cite this version:**

Jesus Vargas Hernandez. Structural and Morphological modification of TiO<sub>2</sub> doped metal ions and investigation of photo-induced charge transfer processes. Physics [physics]. Le Mans Université; Instituto politécnico nacional (México), 2017. English. NNT : 2017LEMA1018 . tel-01954392

**HAL Id: tel-01954392**

**<https://theses.hal.science/tel-01954392>**

Submitted on 13 Dec 2018

**HAL** is a multi-disciplinary open access archive for the deposit and dissemination of scientific research documents, whether they are published or not. The documents may come from teaching and research institutions in France or abroad, or from public or private research centers.

L'archive ouverte pluridisciplinaire **HAL**, est destinée au dépôt et à la diffusion de documents scientifiques de niveau recherche, publiés ou non, émanant des établissements d'enseignement et de recherche français ou étrangers, des laboratoires publics ou privés.

## Thèse de Doctorat



IPN  
Mexico, CDMX.

# Jesús VARGAS HERNÁNDEZ

*Mémoire présenté en vue de l'obtention du  
Grade de Docteur de l'Université du Maine  
sous le sceau de l'Université Bretagne Loire  
Cotutelle IPN, México CDMX, Mexique*

*École doctorale: 3MPL*

*Discipline: Matière, Molécules, Matériaux  
Spécialité: PHYSIQUE  
Unité de recherche: IMMM-UMR 6283*

*Soutenu le 30/06/2017  
Thèse N°: (10)*

## Structural and morphological modification of TiO<sub>2</sub> doped metal ions and investigations of photo- induced charge transfer processes

### JURY

Rapporteurs: **Robert Kuszelewicz**, Directeur de recherche CNRS, Université PARIS-Descartes  
**Leticia Esperanza Hernández Cruz**, Professeur Université Autonome de l'Etat de Hidalgo

Examineurs: **Claudia Alicia Cortés Escobedo**, Professeur CIITEC, IPN, Mexico D.F  
**Ricardo Cuenca Alvarez**, Professeur CIITEC, IPN, Mexico D.F

Co-Encadrante: **Sandrine Coste**, Maître de Conférences, IMMM, Université du Maine, Le Mans, France

Co-Encadrant: **Felipe de Jesús Carillo Romo**, Professeur CIITEC, IPN, Mexico D.F

Directeur de Thèse: **Abdelhadi KASSIBA**, Professeur, IMMM, Université du Maine, Le Mans, France

Co-directeur de Thèse: **Antonieta García Murillo**, Professeur, CIITEC-IPN, Mexico D.F

# Structural and morphological modification of TiO<sub>2</sub> doped metal ions and investigations of photo-induced charge transfer processes

## Résumé

Le travail de thèse porte sur les méthodes de synthèse de nanostructures de dioxyde de titane et de leurs études physico-chimiques afin de préciser les corrélations entre la morphologie, le dopage métallique, les caractéristiques structurales avec l'efficacité photocatalytique. Le grand intérêt pour les nanomatériaux TiO<sub>2</sub> réside dans la mise au point de nouvelles sources d'énergie ou la conservation de l'environnement par des processus photocatalytiques. Cependant, la limitation principale de TiO<sub>2</sub> est du au large gap électronique (eV ~3,2) du polymorphe Anatase. Ainsi, un des objectifs importants pour l'amélioration de l'efficacité des nanomatériaux TiO<sub>2</sub> est d'augmenter leur photoactivité en décalant la création de paires d'électron-trou de l'UV à la gamme du visible. D'ailleurs, on a montré que l'utilisation de nanostructures 1D de TiO<sub>2</sub> (nanotubes) a amélioré la collection de charges, en favorisant leur transport dans les structures 1D, qui par conséquent réduit au minimum la recombinaison et prolonge les durées de vie des électrons.

La première partie de ce travail est dédiée à la synthèse des nanopoudres TiO<sub>2</sub> dopées par des ions métalliques (Ag, Cu, Eu) préparés par sol-gel. Même avec différents éléments de dopage qui apparemment peuvent adopter le même état de valence (2+) (Cu<sup>2+</sup>, Ag<sup>2+</sup>, Eu<sup>2+</sup>), différents comportements ont été démontrés pour l'incorporation efficace de ces ions dans la structure de TiO<sub>2</sub>. L'anomalie entre les rayons ioniques des différents éléments utilisés module le rapport du dopage substitutionnel. Ceci est en effet réalisé pour Cu<sup>2+</sup> mais dans moins d'ampleur pour Ag<sup>2+</sup> tandis que les ions d'europium forment une ségrégation de phase Eu<sub>2</sub>Ti<sub>2</sub>O<sub>7</sub>. La dégradation de colorants de bleu de méthylène (MB) a été améliorée légèrement avec les échantillons dopés Ag. La raison a été attribuée aux clusters métalliques Ag qui ont été en effet mis en évidence à travers leur bande d'absorption plasmonique.

La deuxième partie porte sur des couches minces de TiO<sub>2</sub> dopés (Cu, Ag, et Eu) qui ont été élaborés par sol-gel et spin-coating et dip-coating. Les paramètres optimaux ont été obtenus pour réaliser les films cristallins mais présentant une organisation mésoporeuse qui dépend également du processus de dopage. Des études de Photocatalyse ont été également réalisées et l'efficacité des films ont été comparées en fonction des éléments dopants.

La troisième partie de la thèse est liée à la modification morphologique des nanoparticules pour former des nanotubes à l'aide de la méthode hydrothermale sous pression contrôlée. Un plan d'expérience basé sur la méthode Taguchi a été utilisé pour la détermination des paramètres optimaux. Les nanotubes TiO<sub>2</sub> augmentent la surface spécifique en comparaison avec les nanoparticules. La dégradation de bleu de méthylène par les nanotubes a montré une efficacité photocatalytique plus élevée qu'avec les nanopoudres TiO<sub>2</sub> pures et dopés Ag.

**Mots clés :** Dopage métallique, TiO<sub>2</sub>, Photocatalyse, Nanopoudres, films minces, sol-gel, synthèse hydrothermale, spin-coating, dip-coating, mésoporeuse structures, colorants organiques, RPE, XRD, Raman, XPS, MEB, MET.

## Abstract

The thesis work is focused on the synthesis methods of titanium dioxide nanostructures and their physico-chemical studies in order to point out the correlations between the morphology, metal doping, structural features with the photocatalytic efficiency. The great interest on TiO<sub>2</sub> nanomaterials deals with new sources of energy or in the environment preservation through the photocatalytic properties. However, the main limitations is due to the wide band gap (~3.2 eV) of the anatase polymorph. Thus, a major objective for improvement of the performance of TiO<sub>2</sub> nanomaterials is to increase their photoactivity by shifting the onset of the electron-hole pairs creation from UV to the visible range. Moreover, it was found that using one-dimensional (1-D) TiO<sub>2</sub> (nanotubes) improved the charge collection by 1D nanostructures which consequently minimizes the recombination and prolongate the electron lifetimes.

The first part of this work is focused on the synthesis of TiO<sub>2</sub> nanopowders doped with metallic ions (Ag, Cu, Eu) prepared by Sol-gel. Even with different doping elements which apparently can adopt the same valence state (2+) such as (Cu<sup>2+</sup>, Ag<sup>2+</sup>, Eu<sup>2+</sup>), different behaviors were demonstrated for the effective incorporation of these ions in the host structure of TiO<sub>2</sub>. The discrepancy between ionic radii of the different used elements modulates the ratio of the substitutional doping. This is indeed achieved for Cu<sup>2+</sup> but in less extent for Ag<sup>2+</sup> while Europium ions form segregated phase as Eu<sub>2</sub>Ti<sub>2</sub>O<sub>7</sub>. The experiments on the degradation of methylene blue (MB) dyes have shown slight improvement with Ag-doped samples. The reason was tentatively attributed to the Ag clusters which were indeed demonstrated through their plasmon optical band. The second part of the work concerns thin films of TiO<sub>2</sub> doped (Cu, Ag, and Eu) which were elaborated by spin coating and dip coating. The optimal parameters were obtained to achieve crystalline films but presenting mesoporous organisation which also depends on the doping process. Photocatalysis investigations were also realized and the efficiency of the films compared as function of the doping elements.

The third part of the thesis is related to the morphological modification from nanoparticles to nanotubes by using the hydrothermal method with controlled pressure. An experimental design based on Taguchi Method was employed for the determination of the optimal parameters.

TiO<sub>2</sub> nanotubes increase the surface area in comparison with TiO<sub>2</sub> nanoparticles. TiO<sub>2</sub> nanotubes were tested for the methylene blue degradation and show a higher photocatalytic efficiency than TiO<sub>2</sub> nanopowders and TiO<sub>2</sub> doped with Ag.

**Key Words:** Metal doping, TiO<sub>2</sub>, Photocatalyst, Nanopowders, Thin films, Sol-gel, Hydrothermal, Spin coating, Dip coating, Methylene blue, EPR, XRD, Raman, XPS, SEM, TEM.

## Contents

Introduction. ....	1
Bibliography.....	4
I. Fundamentals .....	5
1.1. Titanium dioxide (TiO <sub>2</sub> ). ....	5
1.1.1 Crystal structure and properties. ....	6
1.1.2 Electronic properties of TiO <sub>2</sub> nanomaterials. ....	7
1.1.3 Optical properties. ....	8
1.2 Fundamentals and photocatalysis mechanism of TiO <sub>2</sub> . ....	11
1.3 Doping of TiO <sub>2</sub> . ....	14
1.3.1 Metal Doped TiO <sub>2</sub> . ....	14
1.3.2 System of TiO <sub>2</sub> doped with Cu. ....	18
1.3.3 System of TiO <sub>2</sub> doped with Ag. ....	19
1.3.4 Non-metal doping of TiO <sub>2</sub> . ....	22
1.3.5 Doping with rare earth. ....	23
1.3.6 System of TiO <sub>2</sub> doping with Eu. ....	24
1.4 Morphological modification of the semiconductors. ....	26
1.4.1 Unidimensional structure. ....	27
1.5 Bibliography.....	31
II. Metal doping of TiO <sub>2</sub> powders.....	34
2.1 Synthesis of TiO <sub>2</sub> doped with metallic ions.....	34
2.1.1 TiO <sub>2</sub> doping with Cu. ....	35
2.1.2 TiO <sub>2</sub> doping with Ag. ....	35
2.1.3 TiO <sub>2</sub> doping with Eu. ....	35
2.1.4 Experimental design. ....	35

2.1.5 Synthesis procedure of TiO <sub>2</sub> : Metal.....	37
2.1.5.1 Materials. ....	37
2.1.5.2. Synthesis of pure TiO <sub>2</sub> .....	37
2.1.5.3 Synthesis of TiO <sub>2</sub> doped with metallic ions powders. ....	37
2.2 Results and discussion: Pure TiO <sub>2</sub> particles.....	38
2.2.1 Phase identification by XRD of pure TiO <sub>2</sub> . <i>Effect of the temperature</i> .....	38
2.2.2 Phase identification of TiO <sub>2</sub> powders by Raman spectroscopy.....	39
2.2.3 Optical characterization of pure TiO <sub>2</sub> powders. ....	40
2.2.4 Chemical Analysis by X-ray Photoelectron Spectroscopy of pure TiO <sub>2</sub> powders.....	41
2.2.5 Photocatalytic evaluation of pure TiO <sub>2</sub> powder. ....	41
2.3 Phase identification by XRD of TiO <sub>2</sub> : Cu powders. <i>Effect of the temperature</i> .....	43
2.3.2 Phase identification by XRD of TiO <sub>2</sub> :Cu powders. <i>Effect of the concentration</i> .....	45
2.3.3 Phase identification by Raman spectroscopy of TiO <sub>2</sub> :Cu powders.....	47
2.3.4 BET surface area measurements of TiO <sub>2</sub> :Cu powders.....	48
2.3.5 EPR evaluation of TiO <sub>2</sub> :Cu powders. ....	49
2.3.6 Optical characterization of TiO <sub>2</sub> :Cu powders. ....	51
2.3.7 Chemical Analysis by XPS of TiO <sub>2</sub> :Cu powders.....	53
2.3.8 Photocatalytic evaluation of TiO <sub>2</sub> : Cu powders. ....	55
2.4.1 Phase identification by XRD of TiO <sub>2</sub> :Ag Powders. <i>Effect of the temperature</i> .....	57
2.4.2 Phase identification by XRD of TiO <sub>2</sub> :Ag powders. <i>Effect of the concentration</i> .....	59
2.4.3 Phase identification by Raman spectroscopy of TiO <sub>2</sub> :Ag powders.....	61
2.3.4 BET surface area measurements of TiO <sub>2</sub> :Ag powders.....	62
2.4.5 EPR investigations of TiO <sub>2</sub> :Ag powders. ....	63
2.4.6 Optical characterization of TiO <sub>2</sub> :Ag powder. ....	65
2.4.7 Chemical Analysis by XPS of TiO <sub>2</sub> :Ag powders.....	66

2.4.8 Photocatalytic evaluation of TiO <sub>2</sub> :Ag powders. ....	67
2.5.1 Phase identification by XRD of TiO <sub>2</sub> :Eu powders. <i>Effect of the temperature</i> .....	69
2.5.2 Phase identification by XRD of TiO <sub>2</sub> :Eu powders. <i>Effect of the concentration</i> .....	70
2.5.3 Phase identification by Raman spectroscopy of TiO <sub>2</sub> :Eu powders.....	72
2.5.4 BET surface area measurements of TiO <sub>2</sub> :Eu powders.....	74
2.5.5 EPR evaluation of TiO <sub>2</sub> :Eu powders.....	74
2.5.6 Optical characterization of TiO <sub>2</sub> :Eu powders.....	76
2.5.7 Chemical Analysis by XPS of TiO <sub>2</sub> :Eu powders.....	77
2.5.8 Photocatalytic evaluation of TiO <sub>2</sub> :Eu powders. ....	78
2.6 .Conclusions.....	80
2.6.1 Comparative conductivity versus doping. ....	80
2.6.2 Comparative performance versus doping.....	81
2.7 Bibliography.....	83
III. TiO <sub>2</sub> :M films elaborated by spin coating and dip coating. ....	87
3. Introduction.....	87
3.1 Surfactants and nanoscience. ....	88
3.2 Experimental design. ....	89
3.3 Synthesis of TiO <sub>2</sub> :Metal thin films.....	89
3.3.1 Materials. ....	89
3.3.2. Preparation of the sol for TiO <sub>2</sub> thin films elaboration. ....	90
3.3.3 Preparation of the sol for TiO <sub>2</sub> doped with metallic ions.....	90
3.3.4 Cleaning of the substrates.....	90
3.3.5 TiO <sub>2</sub> films elaborated by dip coating.....	90
3.3.6 TiO <sub>2</sub> films elaborated by spin coating. ....	91
3.4 Phase identification by XRD of TiO <sub>2</sub> :M films elaborated by spin coating. ....	92

3.5 Phase identification by Raman spectroscopy of pure TiO <sub>2</sub> and TiO <sub>2</sub> :M 3% mol, elaborated by spin coating. ....	94
3.6 Morphological analysis of TiO <sub>2</sub> :M films elaborated by dip coating and spin coating. ....	95
3.7 Optical characterization of TiO <sub>2</sub> :M films elaborated by spin coating and dip coating. ....	98
3.8 Photocatalytic evaluation of TiO <sub>2</sub> : M films. ....	99
3.9 Conclusions.....	102
3.10 Bibliography.....	103
IV. TiO <sub>2</sub> nanotubes for photocatalysis applications.....	104
4. Introduction.....	104
4.1 Experimental design. ....	107
4.2 Synthesis of TiO <sub>2</sub> nanotubes. ....	108
4.2.1. Materials. ....	108
4.2.2 Sol-Gel method. ....	108
4.2.3 Hydrothermal method. ....	109
4.3 Results and discussion of TiO <sub>2</sub> nanotubes.....	110
4.3.1 Phase identification of TiO <sub>2</sub> nanotubes by X-ray Diffraction.....	110
4.3. Phase identification of TiO <sub>2</sub> nanotubes by Raman spectroscopy.....	111
4.3.3 Optical analysis of TiO <sub>2</sub> nanotubes.....	113
4.3.4 Morphology analysis of TiO <sub>2</sub> nanotubes. ....	114
Surface Area Determination of TiO <sub>2</sub> nanotubes by the BET method (Branauer, Emmety Teller). .....	117
4.3.5 Photocatalytic degradation of methylene blue in water by TiO <sub>2</sub> nanotubes.....	118
4.4 Conclusions.....	121
4.5 Bibliography.....	122
V General conclusions.....	125

VI. Appendix.....	127
6.1 Synthesis methods.....	127
6.1.1 Sol-Gel.....	127
6.1.2 Hydrothermal method.....	129
6.2 Characterization techniques.....	132
6.2.1 X-ray Diffraction.....	132
6.2.2 BET surface area analysis.....	135
6.2.3 Atomic force microscope.....	137
6.2.4 Electron Paramagnetic Resonance.....	139
6.2.5 Raman spectroscopy.....	143
6.2.6 Diffuse reflectance spectroscopy.....	145
6.2.7 Photocatalysis test.....	146
6.3 Bibliography.....	148



## LIST OF FIGURES

Fig. 1. Crystalline structure of TiO <sub>2</sub> anatase (a), rutile (b).	6
Fig. 2. Molecular-orbital bonding structure of anatase TiO <sub>2</sub> : (a) atomic levels; (b) crystal-field split levels; (c) final interaction states. The thin solid line and dashed line represent large and small contributions, respectively.	8
Fig. 3. Crystalline size effect on optical properties of nanocrystals; For ZnO: $m_e^*=10$ , $m_h^*=0.8$ , $E_g=3.2$ eV, and $\epsilon=86$ ; para TiO <sub>2</sub> : $m_e^*=10$ , $m_h^*=0.8$ , $E_g=3.2$ eV, and $\epsilon=86$ ; and for SnO <sub>2</sub> : $m_e^*=0.3$ , $m_h^*=0.8$ , $E_g=3.6$ eV and $\epsilon=12$ .	9
Fig. 4. Illustration of the modification paths for TiO <sub>2</sub> nanomaterials.	10
Fig. 5. Photoinduced processes on TiO <sub>2</sub> .	11
Fig. 6. Photocatalytic process.	13
Fig. 7. Schematic representation of the energy levels of doped semiconductors: p-type doping (left) and n-type doping (right).	16
Fig. 8. Schematic representation of the distortion of the TiO <sub>6</sub> octahedra on doping Cu <sup>2+</sup> ion on the Ti <sup>4+</sup> lattice site.	18
Fig. 9. Schematic diagram of photocatalysis mechanism Ag/TiO <sub>2</sub> photocatalyst under artificial visible light irradiation.	19
Fig. 10. Schematic illustration of the possible mechanism of energy transfer from the TiO <sub>2</sub> host to Eu <sup>3+</sup> .	25
Fig. 11 Models of charge recombination in a semiconductor particle; a) Surface trapping sites and b) Within particle trapping sites.	27
Fig. 12. The key difference between the (a) particulate and (b) nanotubular film architecture is the large presence of inter-particle grain boundaries as shown in this representative schematic with TiO <sub>2</sub> films as an example oxide photocatalyst.	28
Fig. 13 X-ray diffractogram of TiO <sub>2</sub> pure at different thermal treatments.	38
Fig. 14. Raman spectra of pure TiO <sub>2</sub> heat treated at 500°C and 800°C.	39
Fig. 15. Optical spectroscopy. a) Diffuse reflectance (%) spectra of pure TiO <sub>2</sub> powders with the corresponding b) Kubelka-Munk absorption curves, c) Determination of band gap.	40
Fig. 16. XPS spectra of pure TiO <sub>2</sub> .	41
Fig. 17. Absorption spectra of methylene blue photodegradation by pure TiO <sub>2</sub> powder.	42
Fig. 18 First order Kinetics of methylene blue photodegradation by pure TiO <sub>2</sub> powder..	43
Fig. 19. X-ray diffractograms of 3%Cu-TiO <sub>2</sub> annealed at different temperatures.	44
Fig. 20. X-ray diffractogram of TiO <sub>2</sub> doped with copper (1, 2 and 3% mol) annealed at 500°C.	45
Fig. 21. Raman spectra of TiO <sub>2</sub> doped with copper (1, 2 and 3% mol) annealed at 500°C.	47
Fig. 22. EPR spectrum of Cu <sup>2+</sup> ions in TiO <sub>2</sub> with the experimental (continuous) and the simulated one (dashed).	49
Fig. 23. Optical spectroscopy. a) Diffuse reflectance (%) spectra of TiO <sub>2</sub> doped powders with copper (1, 2 and 3% mol) with the corresponding b) Kubelka-Munk absorption curves, c) Determination of band gap.	51
Fig. 24. Jahn-Teller(J-T) distortion of the octahedral symmetry of TiO <sub>6</sub> and changes in the d-d transition from octahedral to tetragonal phase. In undistorted octahedral coordination, only a single electronic transition occurs	52
Fig. 25. XPS spectra of 3%Cu-TiO <sub>2</sub> annealed at 500°C.	53
Fig. 26. Absorption spectra of methylene blue photodegradation by TiO <sub>2</sub> doped with copper (1, 2 and 3% mol).	55
Fig. 27. First order Kinetics of methylene blue photodegradation by TiO <sub>2</sub> doped with copper (1, 2 and 3% mol).	56
Fig. 28. X-ray diffractograms of 3%Ag-TiO <sub>2</sub> annealed at different temperatures.	57
Fig. 29. X-ray diffractogram of TiO <sub>2</sub> doped with silver (1, 2 and 3% mol) annealed at 500°C.	59
Fig. 30. Raman spectra of TiO <sub>2</sub> doped with silver (1, 2 and 3% mol) annealed at 500°C.	61
Fig. 31. EPR spectra of 3 at.% Ag doped TiO <sub>2</sub> powder with the experimental (tick line) and simulation (thin line).	64
Fig. 32. Optical spectroscopy. a) Diffuse reflectance (%) spectra of TiO <sub>2</sub> doped with silver (1, 2 and 3% mol) with the corresponding b) Kubelka-Munk absorption curves, c) Determination of band gap.	65
Fig. 33. XPS spectra of 3%Ag-TiO <sub>2</sub> annealed at 500°C.	66
Fig. 34. Absorption spectra of methylene blue photodegradation by TiO <sub>2</sub> doped with silver (1, 2 and 3% mol).	67

Fig. 35. First order Kinetics of methylene blue photodegradation by TiO <sub>2</sub> doped with silver (1, 2 and 3% mol).	68
Fig. 36. X-ray diffractograms of 3%Eu-TiO <sub>2</sub> annealed at different temperatures.	69
Fig. 37. X-ray diffractogram of TiO <sub>2</sub> doped with europium (1, 2 and 3% mol) annealed at 800°C.	70
Fig. 38. Raman spectra of TiO <sub>2</sub> doped with europium (1, 2 and 3% mol) annealed at 800°C.	72
Fig. 39. EPR spectra of Eu-TiO <sub>2</sub> at different concentrations 3 at.% (grey line), 2at.% (thick black line), 1 at.% (dashed line).	75
Fig. 40. Optical spectroscopy. a) Diffuse reflectance (%) spectra of TiO <sub>2</sub> doped with europium (1, 2 and 3% mol) with the corresponding b) Kubelka-Munk absorption curves, c) Determination of band gap.	76
Fig. 41. XPS spectra of 3%Eu-TiO <sub>2</sub> annealed at 500°C.	77
Fig. 42. Absorption spectra of methylene blue photodegradation by TiO <sub>2</sub> doped with europium (1, 2 and 3% mol).	78
Fig. 43. First order Kinetics of methylene blue photodegradation by TiO <sub>2</sub> doped with silver (1, 2 and 3% mol).	79
Fig. 44. Semi-log plot of $\sigma_{dc}$ conductivity versus inverse temperature for pure and metal-doped TiO <sub>2</sub> .	80
Fig. 45 First order Kinetics of methylene blue photodegradation by 3% M-TiO <sub>2</sub> (M=Cu, Ag, and Eu).	82
Fig. 46 X-ray diffractograms of 3%M-TiO <sub>2</sub> films (Cu, Ag, and Eu) annealed at 450 °C elaborated by spin coating.	92
Fig. 47. Raman spectra of TiO <sub>2</sub> pure and doped (Cu, Ag, and Eu) elaborated by a) dip coating and b) spin coating, annealed at 450 °C.	94
Fig. 48. AFM morphology of TiO <sub>2</sub> film elaborated by spin coating, (10 $\mu$ m x 10 $\mu$ m): a) Pure TiO <sub>2</sub> , b) TiO <sub>2</sub> : Cu 3% mol, c) TiO <sub>2</sub> :Ag 3% mol and d) TiO <sub>2</sub> :Eu.	96
Fig. 49. Doping effect in the contact angle for films elaborated by spin coating: a) Pure TiO <sub>2</sub> and b) Doped TiO <sub>2</sub> .	96
Fig. 50. AFM morphology of TiO <sub>2</sub> film elaborated by dip coating (10 $\mu$ m x 10 $\mu$ m): a) Pure TiO <sub>2</sub> , b) TiO <sub>2</sub> : Cu 3% mol, c) TiO <sub>2</sub> :Ag 3% mol and d) TiO <sub>2</sub> :Eu.	97
Fig. 51. Doping effect in the contact angle for films elaborated by spin coating: a) Pure TiO <sub>2</sub> and b) Doped TiO <sub>2</sub> .	97
Fig. 52. Optical characterization of M-TiO <sub>2</sub> films. Transmittance spectra and band gap determination of a) and c) respectively of M-TiO <sub>2</sub> films elaborated by spin coating. Transmittance spectra and band gap determination of b) and d) respectively of M-TiO <sub>2</sub> films elaborated by dip coating.	99
Fig. 53. Absorbance spectra of the methylene blue by the photodegradation with M-TiO <sub>2</sub> films elaborated by spin coating.	99
Fig. 54. Absorbance spectra of the methylene blue by the photodegradation with M-TiO <sub>2</sub> films elaborated by dip coating.	100
Fig. 55. First order Kinetics of methylene blue photodegradation with M-TiO <sub>2</sub> films elaborated by a) dip coating and b) spin coating.	101
Fig. 56. Formation mechanism of TiO <sub>2</sub> nanotubes using hydrothermal method	105
Fig. 57. X-ray diffractogram of TiO <sub>2</sub> nanotubes (TG1-TG9).	110
Fig. 58. Raman spectra of TiO <sub>2</sub> nanotubes (TG1-TG9).	111
Fig. 59. Diffuse reflectance spectroscopy; a) Diffuse reflectance (%R) spectra, b) Kubelka-Munk absorption curves and determination of band gap of TiO <sub>2</sub> nanotubes.	113
Fig. 60. SEM image of TiO <sub>2</sub> nanoparticles annealed at 500°C.	114
Fig. 61. SEM images of the samples treated by hydrothermal method (TG1-TG9).	115
Fig. 62. TEM image of the TiO <sub>2</sub> nanotube (TG5).	116
Fig. 63. Influence of design parameters on the formation of TiO <sub>2</sub> nanotubes.	116
Fig. 64. Evolution of the optical absorption of methylene blue degradation by TiO <sub>2</sub> nanoparticles.	118
Fig. 65 Evolution of the optical absorption of methylene blue degradation by TiO <sub>2</sub> nanotubes (TG1-TG9)	119
Fig. 66.Pseudo first-order kinetics of degradation of Methylene Blue solutions.	120
Fig. 67. Conventional autoclave type Tuttle Roy	129
Fig. 68. Phase diagram of water.	130
Fig. 69. Variation of the dielectric constant of water with temperature and pressure.	131
Fig. 70. Schematic diagram of an X-ray diffractometer.	133
Fig. 71. PANalytical $\theta/\theta$ Bragg- Brentano X'pert MDP PRO diffractometer for measurements of powders.	134
Fig. 72. PANalytical diffractometer with a design of low incidence X-ray.	134

<i>Fig. 73. Molecules on the surface (in blue) are experiencing a bond deficiency, thus it is energetically favorable for them to adsorb molecules (in yellow).</i>	135
<i>Fig. 74. Working steps of the BET equipment.</i>	136
<i>Fig. 75. Schematic representation of the AFM, a) contact mode and b) tapping mode</i>	138
<i>Fig. 76 Energy levels for an electron spin (<math>S=\pm \frac{1}{2}</math>) in an applied magnetic field <b>B</b>.</i>	141
<i>Fig. 77. EPR equipment, Bruker EMX.</i>	142
<i>Fig. 78. Scattering events occurring in an excited material.</i>	143
<i>Fig. 79. Raman spectroscopy equipment XploRA (Jobin-Yvon-Horiba).</i>	144
<i>Fig. 80. Schematic diagram of UV-vis diffuse reflectance measurement system.</i>	145
<i>Fig. 81. UV-Vis spectrometer Ocean Optics HR4000.</i>	146
<i>Fig. 82. Illustration of the photocatalysis test design-</i>	147



# Introduction.



## Introduction.

TiO<sub>2</sub> powders have been commonly used as white pigments from ancient times. They are inexpensive, chemically stable and harmless, and have no absorption in the visible region. Therefore, they have a white color. However, the chemical stability of TiO<sub>2</sub> holds only in the dark. Instead, it is active under UV light irradiation, inducing some chemical reactions. Such activity under sunlight was known from the flaking of paints and the degradation of fabrics incorporating TiO<sub>2</sub>. Scientific studies on such photoactivity of TiO<sub>2</sub> have been reported since the early part of the 20<sup>th</sup> century [1, 2]. For example, there was a report on the photobleaching of dyes by TiO<sub>2</sub> both in vacuo and in oxygen in 1938. It was reported that UV absorption produces active oxygen species on the TiO<sub>2</sub> surface, causing the photobleaching of dyes. It was also known that titania itself does not change through the photoreaction, although the “photocatalyst” terminology was not used for TiO<sub>2</sub> in the report, but called a photosensitizer [3].

It is equivocal when and who started utilizing first such a photochemical power of TiO<sub>2</sub> to induce chemical reactions actively, but at least in Japan, there were a series of reports by Mashio et al.,

from 1956, entitled “Autooxidation by  $\text{TiO}_2$  as a photocatalyst” [4]. They dispersed  $\text{TiO}_2$  powders into various organic solvents such as alcohols and hydrocarbons followed by the UV irradiation with an Hg lamp. They observed the autooxidation of solvents and the simultaneous formation of  $\text{H}_2\text{O}_2$  under ambient conditions. It is interesting to note that they had already compared the photocatalytic activities of various  $\text{TiO}_2$  powders using twelve types of commercial anatase and three types of rutile, and concluded that the anatase activity of the autooxidation is much higher than that of rutile, suggesting a fairly high degree of progress of the research.

In 1972, Fujishima and Honda discovered the phenomenon of the photocatalytic splitting of water on a  $\text{TiO}_2$  electrode under ultraviolet (UV) light. Since then, enormous efforts have been devoted to the research of  $\text{TiO}_2$  material, which has led to many promising applications in areas ranging from photovoltaics and photocatalysis to photo-/electrochromics and sensors. These applications can be roughly divided into “energy” and “environmental” categories, many of which depend not only on the properties of the  $\text{TiO}_2$  material itself but also on the modifications of the  $\text{TiO}_2$  material host (e.g., with inorganic and organic dyes) and on the interactions of  $\text{TiO}_2$  materials with environment [5]. One of the most interesting aspects of  $\text{TiO}_2$  is that the types of photochemistry responsible for photocatalysis and hydrophilicity are completely different, even though both can occur simultaneously on the same surface [6].

New physical and chemical properties emerge when the size of the material becomes smaller and smaller, and down to the nanometer scale. Properties also vary as the shapes of the shrinking nanomaterials change. Among the unique properties of nanomaterials, the movement of electrons and holes in semiconductor nanomaterials is primarily governed by the well-known quantum confinement, and the transport properties related to phonons and photons are largely affected by the size and geometry of the materials. The specific surface area and surface-to-volume ratio increase dramatically as the size of material decreases. The high surface area brought about by small particle size is beneficial to many  $\text{TiO}_2$ -based devices, as it facilitates reaction/interaction between the devices and the interacting media, which mainly occurs on the surface or at the interface and strongly depends on the surface area of the material. As the most promising photocatalyst,  $\text{TiO}_2$  materials are expected to play an important role in helping solve many serious environmental and pollution challenges [5].

Since the bulk of the terrestrial solar energy is in the visible spectrum, any shift in the optical response of titania, or its high-bandgap energy metal oxide counterparts, from the UV towards the visible spectrum offers the potential for a significant, positive impact on the photocatalytic and photoelectrochemical utility of the material(s) [7]. Some studies about morphological modification have shown that one-dimensional structures have a better performance for photovoltaic and photocatalytic applications [8-10]. The doping process is an effective approach to improve the visible light activity. Doping with cations or anions may alter the band gap or introduction of intraband gap states which may make  $\text{TiO}_2$  absorb the visible light.[11].

The present thesis is focused on the morphology and structural study of  $\text{TiO}_2$ . The morphological modification from nanoparticles to nanotubes by the hydrothermal method with control of pressure was studied. The other path followed, is the study of additions of other elements to the crystal structure of  $\text{TiO}_2$  (doping) through ions which promising increase the photochemical properties of the semiconductor, synthesized by the sol-gel method. Thin films from the same systems doping were fabricated by dip coating, and spin coating techniques through a stable sol.

## Bibliography.

1. Keidel, E., *Die Beeinflussung der Lichtecktheit von Teerfarblacken durch Titanweiss*. Farben-Zeitung, 1929. **34**: p. 1242-1243.
2. Hashimoto, K., H. Irie, and A. Fujishima, *TiO<sub>2</sub> photocatalysis: a historical overview and future prospects*. Japanese journal of applied physics, 2005. **44**(12R): p. 8269.
3. Goodeve, C.F. and J.A. Kitchener, *Photosensitisation by titanium dioxide*. Transactions of the Faraday Society, 1938. **34**(0): p. 570-579.
4. Kato, S. and F. Mashio, *Autooxidation by TiO<sub>2</sub> as a photocatalyst*. Abtr Book Annu Meet Chemical Society of Japan, 1956. **223**.
5. Chen, X. and S.S. Mao, *Titanium dioxide nanomaterials: synthesis, properties, modifications, and applications*. Chem Rev, 2007. **107**(7): p. 2891-959.
6. Fujishima, A., T.N. Rao, and D.A. Tryk, *Titanium dioxide photocatalysis*. Journal of Photochemistry and Photobiology C: Photochemistry Reviews, 2000. **1**(1): p. 1-21.
7. Grimes, C.A., O.K. Varghese, and S. Ranjan, *Oxide Semiconductors Nano-Crystalline Tubular and Porous Systems*, in *Light, Water, Hydrogen: The Solar Generation of Hydrogen by Water Photoelectrolysis*, C.A. Grimes, O.K. Varghese, and S. Ranjan, Editors. 2008, Springer US: Boston, MA. p. 257-369.
8. Flores, I.C., J.N. de Freitas, C. Longo, M.-A. De Paoli, H. Winnischofer, and A.F. Nogueira, *Dye-sensitized solar cells based on TiO<sub>2</sub> nanotubes and a solid-state electrolyte*. Journal of Photochemistry and Photobiology A: Chemistry, 2007. **189**(2-3): p. 153-160.
9. Sathish, M., B. Viswanathan, R.P. Viswanath, and C.S. Gopinath, *Synthesis, Characterization, Electronic Structure, and Photocatalytic Activity of Nitrogen-Doped TiO<sub>2</sub> Nanocatalyst*. Chemistry of Materials, 2005. **17**(25): p. 6349-6353.
10. Xu, H., X. Tao, D.-T. Wang, Y.-Z. Zheng, and J.-F. Chen, *Enhanced efficiency in dye-sensitized solar cells based on TiO<sub>2</sub> nanocrystal/nanotube double-layered films*. Electrochimica Acta, 2010. **55**(7): p. 2280-2285.
11. Prakash, T., *Review on nanostructured semiconductors for dye sensitized solar cells*. Electronic Materials Letters, 2012. **8**(3): p. 231-243.



# CHAPTER I

## Fundamentals

### I. Fundamentals



#### 1.1. Titanium dioxide (TiO<sub>2</sub>).

TiO<sub>2</sub> is a chemically stable, nontoxic, biocompatible, inexpensive material with very high dielectric constant and interesting photocatalytic activities. It is a wide-gap semiconductor, and depending on its chemical composition, it shows a large range of electrical conductivity. In general, TiO<sub>2</sub> has two stable crystalline structures: anatase and rutile. Usually, natural rutile crystals are impure, and, therefore, early investigations were limited to ceramic samples only, but later (around 1950s), a colorless, large, single crystal of synthetic rutile was grown by the Boule technique [1]. Thereafter, most of the research was done on the electro-optical characterization and defect chemistry of single rutile crystals. The stoichiometry of the rutile TiO<sub>2</sub> is highly dependent on its deposition parameters, especially on annealing conditions and atmosphere [2]. Earlier, it was assumed that the properties of anatase would be similar to those of rutile until a new solar cell concept was reported using anatase, which cannot be realized by rutile structure. [3].



### 1.1.1 Crystal structure and properties.

Besides the four polymorphs of  $\text{TiO}_2$  found in nature (i.e., anatase (tetragonal), brookite (orthorhombic), rutile (tetragonal), and  $\text{TiO}_2$  (B) (monoclinic)), two additional high-pressure forms have been synthesized starting from rutile:  $\text{TiO}_2$ (II) [103], which has the  $\text{PbO}_2$  structure, and  $\text{TiO}_2$ (H) with the hollandite structure [4, 5].

Rutile and anatase structures can be described regarding chains of  $\text{TiO}_6$  octahedra, where each  $\text{Ti}^{4+}$  ion is surrounded by an octahedron of six  $\text{O}^{2-}$  ions. The two crystal structures differ in the distortion of each octahedron and by the assembly pattern of the octahedral chains. In rutile, the octahedron shows a slight orthorhombic distortion; in anatase, the octahedron is significantly distorted so that its symmetry is lower than orthorhombic. The Ti-Ti distances in anatase are larger, whereas the Ti-O distances are shorter than those in rutile. In the rutile structure, each octahedron is in contact with ten neighbor octahedrons (two sharing edge oxygen pairs and eight sharing corner oxygen atoms), while, in the anatase structure, each octahedron is in contact with eight neighbors (four sharing an edge and four sharing a corner). These differences in lattice structures cause different mass densities and electronic band structures between the two forms of  $\text{TiO}_2$  [6].

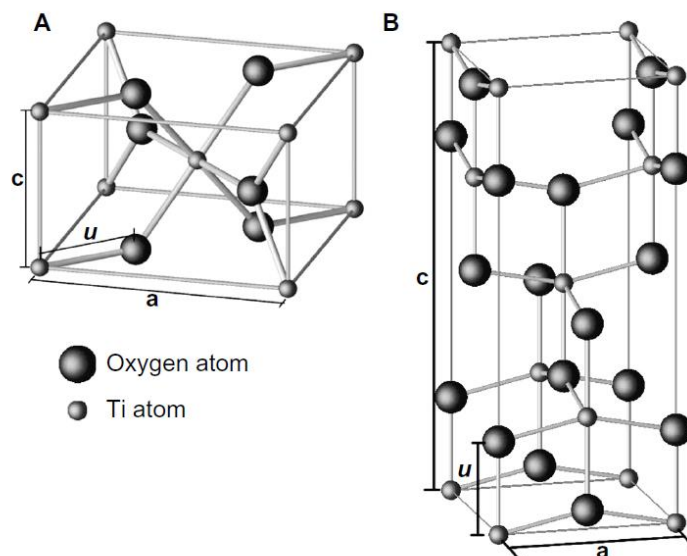


Fig. 1. Crystalline structure of  $\text{TiO}_2$  anatase (a), rutile (b).

Among these structures, rutile is the most stable phase, whereas anatase is metastable at room temperature and transforms irreversibly into rutile upon heating above a threshold temperature around 1000 °C (which is in atmospheric conditions, but the threshold temperature can vary from 400 °C to 1200 °C, depending on the grain size, ambient conditions, and impurities). Natural rutile crystals exhibit predominantly (110) surface, which is considered to be the most stable surface of stoichiometric rutile, whereas anatase is the most stable with (101) surface [2].

The application of anatase phase or rutile phase depends on its crystallinity and isomorphism. Therefore the application can vary. For example, the anatase phase is most used in charge separation devices, while rutile is predominantly used in gas sensors and dielectric layer [7].

### 1.1.2 Electronic properties of TiO<sub>2</sub> nanomaterials.

The density of states of TiO<sub>2</sub> is composed of Ti e<sub>g</sub>, Ti t<sub>2g</sub> (d<sub>yz</sub>, d<sub>zx</sub>, and d<sub>xy</sub>), O p<sub>σ</sub> (in the Ti<sub>3</sub>O cluster plane), and O p<sub>π</sub> (out of the Ti<sub>3</sub>O cluster plane), as shown in Fig. 2. The upper valence bands can be decomposed into three main regions; the σ bonding in the lower energy region mainly due to O p<sub>σ</sub> bonding; the π bonding in the middle energy region; and O p<sub>π</sub> states in the higher energy region due to O p<sub>π</sub> nonbonding states at the top of the valence bands where the hybridization with d states is almost negligible. The contribution of the π bonding is much weaker than that of the σ bonding. The conduction bands are decomposed into Ti e<sub>g</sub> (>5 eV) and t<sub>2g</sub> bands (<5 eV). The d<sub>xy</sub> states are dominantly located at the bottom of the conduction bands (the vertical dashed line). The rest of the t<sub>2g</sub> bands are antibonding with p states. The main peak of the t<sub>2g</sub> bands is identified to be mostly d<sub>yz</sub> and d<sub>zx</sub> states [6].

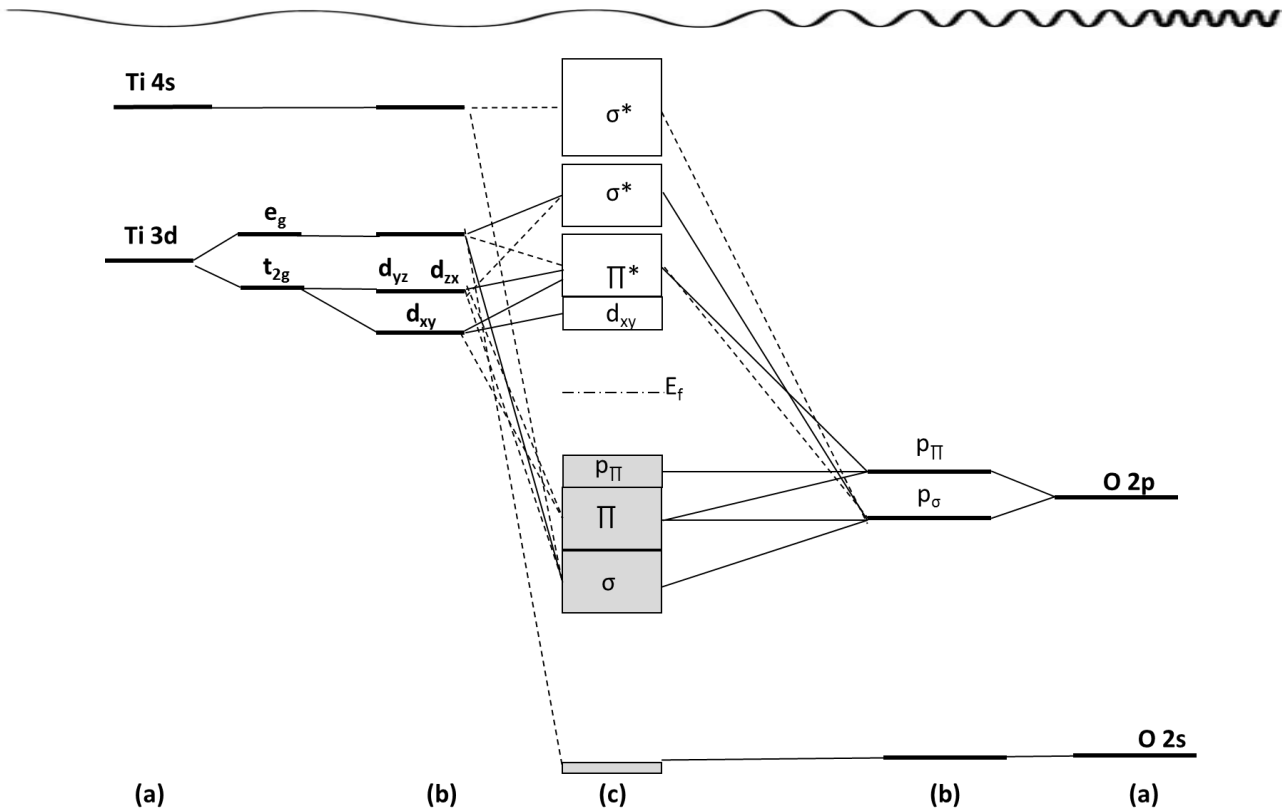


Fig. 2. Molecular-orbital bonding structure of anatase  $\text{TiO}_2$ : (a) atomic levels; (b) crystal-field split levels; (c) final interaction states. The thin solid line and dashed line represent large and small contributions, respectively.

### 1.1.3 Optical properties.

The optical properties of semiconductors, such as the absorbance and emission, result from the excitonic transitions. The influence of size on these properties occurs when the diameter is comparable to or smaller than the exciton diameter; the consequent changes in the electronic structure are called the confinement effect. Excitons are imaginary quasiparticles produced by the pairing of an electron (from the conduction band) and a hole (from the valence band) resulting from the Coulomb interaction. Such crystallite size in semiconductor nanocrystals is understandable from the work of Brus [8], and his effective mass approximation theory. According to the theory, model

$$E_g^* = E_g + \frac{\pi^2 \hbar^2}{2R^2} \left[ \frac{1}{m_e} \frac{1}{m_h} \right] - \left[ \frac{1.786e^2}{\epsilon R} \right] \quad \text{Equation 1}$$

where  $E_g$  and  $E_g^*$  are the bandgap value of the bulk and confined crystallite, respectively;  $\epsilon$  is the dielectric constant;  $R$  is the radius of the crystallite;  $m_e$  is the effective mass of electron; and  $m_h$  is the effective mass of the hole. This theory has also been applied to determine the bandgap widening ( $\Delta E_g = E_g^* - E_g$ ) in ZnO, SnO<sub>2</sub>, and TiO<sub>2</sub> nanocrystals. A plot between the crystallite diameter and bandgap widening is presented in Fig. 3 [9].

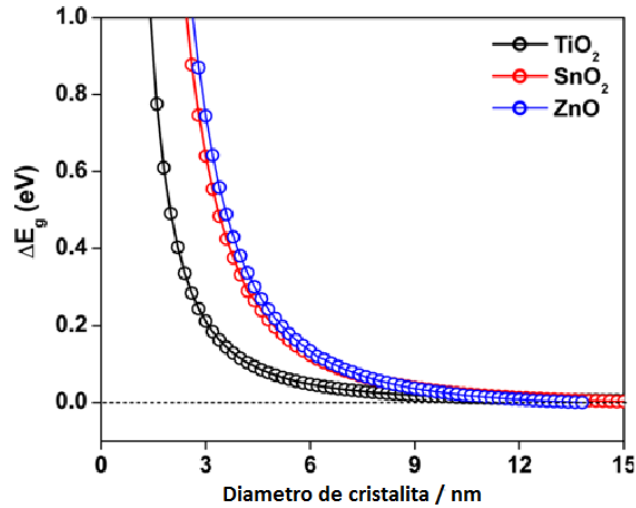


Fig. 3. Crystalline size effect on optical properties of nanocrystals; For ZnO:  $m_e^*=10$ ,  $m_h^*=0.8$ ,  $E_g=3.2$  eV, and  $\epsilon=86$ ; para TiO<sub>2</sub>:  $m_e^*=10$ ,  $m_h^*=0.8$ ,  $E_g=3.2$  eV, and  $\epsilon=86$ ; and for SnO<sub>2</sub>:  $m_e^*=0.3$ ,  $m_h^*=0.8$ ,  $E_g=3.6$  eV and  $\epsilon=12$ .

The main mechanism of light absorption in pure semiconductors is direct interband electron transitions. This absorption is especially small in indirect semiconductors, e.g. TiO<sub>2</sub>, where the direct electron transitions between the band centers are prohibited by the crystal symmetry. Indirect electron transitions with the momentum nonconservation at the interface can enhance the light absorption in small TiO<sub>2</sub> crystallites. This effect increases at a rough interface when the share of the interface atoms is larger. The indirect transitions are allowed due to a large dipole matrix element and a large density of states for the electron in the valence band. Considerable enhancement of the absorption is expected in small TiO<sub>2</sub> nanocrystals, as well as in porous and microcrystalline semiconductors when the share of the interface atoms is sufficiently large. Electron transitions to the conduction band become possible when  $h\nu = E_g + W_c$ . Further enhancement of the absorption occurs due to an increase in the electron density of states in the valence band. The interface absorption becomes the main mechanism of light absorption for the crystallites that are smaller than 20 nm. Due to lower dimensionality, the band gap of TiO<sub>2</sub> nanomaterials is larger than the band gap of bulk TiO<sub>2</sub> [10].

Many applications of TiO<sub>2</sub> nanomaterials are closely related to their optical properties. However, the highly efficient use of TiO<sub>2</sub> nanomaterials is sometimes prevented by the wide band gap of TiO<sub>2</sub>. The band gap of bulk TiO<sub>2</sub> lies in the UV regime (3.0 eV for rutile phase and 3.2 eV for anatase phase), which is only a small fraction of the sun's energy (<10%). Thus, one of the goals for improvement of the performance of TiO<sub>2</sub> nanomaterials is to increase their optical activity by shifting the onset of the response from the UV to the visible region. There are several ways to achieve this goal. First doping TiO<sub>2</sub> nanomaterials with other elements can modify the electronic properties and thus alter the optical properties of TiO<sub>2</sub> nanomaterials. Second, sensitizing TiO<sub>2</sub>, with other colorful inorganic or organic compounds can improve its optical activity in the visible light region [11-13]. Third, coupling collective oscillations of the electrons in the conduction band of metal nanoparticle surfaces to those in the conduction band of TiO<sub>2</sub> nanomaterials in metal-TiO<sub>2</sub> nanocomposites can improve the performance. Also, the modification of TiO<sub>2</sub> nanomaterial surface with other semiconductors can alter the charge transfer properties between TiO<sub>2</sub> and the surrounding environment, thus improving the performance of TiO<sub>2</sub> nanomaterials based devices. Fig. 4 illustrates the modification paths in improving the properties (mainly the optical properties) of TiO<sub>2</sub> nanomaterials [10].

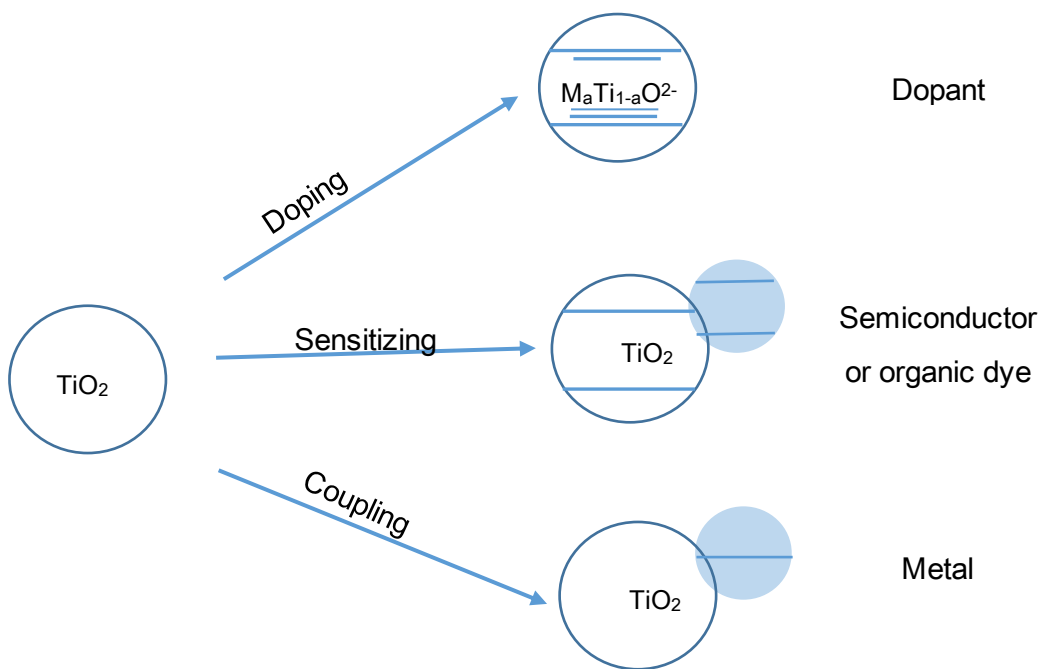


Fig. 4. Illustration of the modification paths for TiO<sub>2</sub> nanomaterials.

## 1.2 Fundamentals and photocatalysis mechanism of $\text{TiO}_2$ .

$\text{TiO}_2$  is characterized by the presence of photoinduced phenomena. These are depicted in Fig. 5. All these photoinduced processes originate from the semiconductor band gap. When photons have a higher energy than this band gap, they can be absorbed, and an electron is promoted to the CB, leaving a hole in the VB. This excited electron can either be used directly to create electricity in photovoltaic solar cells or drive a chemical reaction, which is called photocatalysis. A special phenomenon was recently discovered: trapping of holes at the  $\text{TiO}_2$  surface causes a high wettability and is termed 'photoinduced super hydrophilicity' (PSH). All photoinduced phenomena involve surface bound redox reactions. [5].

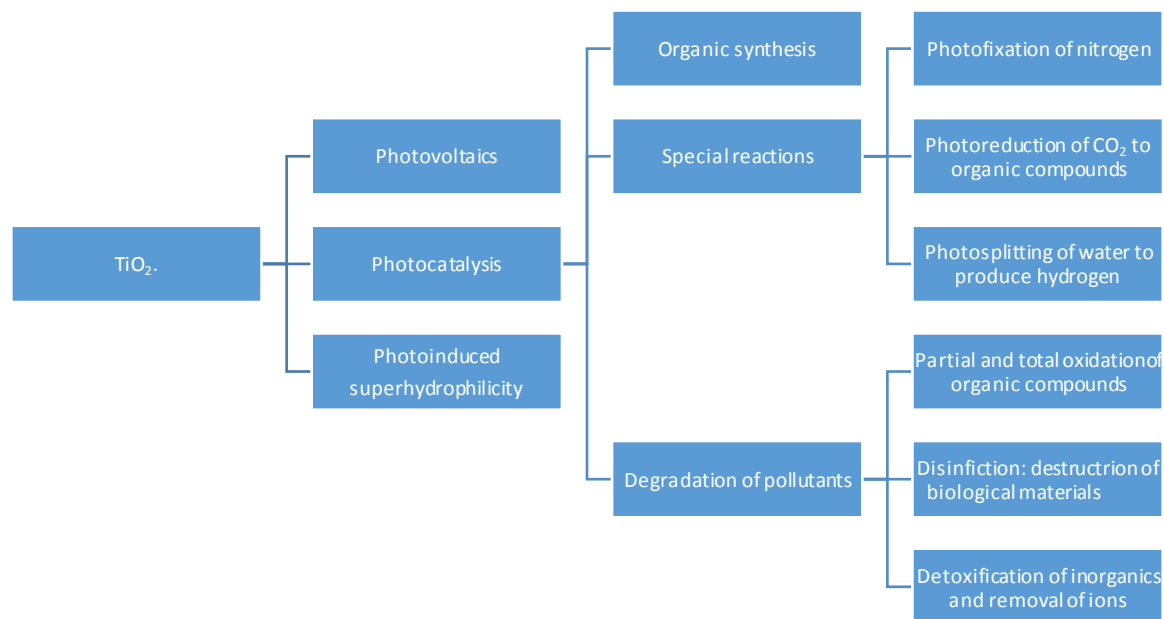


Fig. 5. Photoinduced processes on  $\text{TiO}_2$ .

The first report on the efficient hydrogen production from water and organic compounds was published in *Nature* at the time of the second oil crisis [14], and  $\text{TiO}_2$  photocatalysis drew the attention of many people as one of the promising methods for hydrogen production. However, even though the reaction efficiency is very high,  $\text{TiO}_2$  can absorb only the UV light contained in a solar spectrum, which is only about 3%. Therefore, from the viewpoint of  $\text{H}_2$  production technology,  $\text{TiO}_2$  photocatalysis is not very attractive. Various other semiconductors with a small band gap, such as CdS and CdSe, were investigated, but their efficiency and stability were much

lower than those of  $\text{TiO}_2$ , and the enthusiasm in the research of the  $\text{H}_2$  production was over in the middle of the 1980s.

Instead, the research shifted to the utilization of the strong photoproduced oxidation power of  $\text{TiO}_2$  for the destruction of pollutants. The first such reports were those of Frank and Bard in 1977, in which they described the decomposition of cyanide in the presence of aqueous  $\text{TiO}_2$  suspensions. In the 1980s, detoxications of various harmful compounds in both water and air were demonstrated using powdered  $\text{TiO}_2$  actively as potential purification methods of wastewater and polluted air. The platinization of  $\text{TiO}_2$  was not necessary in this case, and  $\text{TiO}_2$  powder itself was used under ambient condition [15][16].

Photocatalysis is based on the excitation of a semiconductor material with irradiation of light energy at least equal or greater to that of the band gap energy of the material. An electron in an electron filled valence band (VB) is excited upon irradiation of light to a vacant conduction band (CB) and leave behind a positive hole ( $\text{h}^+$ ) in the VB. These electrons and holes ( $\text{e}^-$  and  $\text{h}^+$ ) are mainly responsible for the generation of active species which degrade the target molecules. These charge carriers  $\text{e}^-$  and  $\text{h}^+$  drive the reduction and oxidation, respectively. These charge carriers migrate to the photocatalyst surface and indicate the secondary reactions with the adsorbed components on the surface of the solid semiconductor. The photoexcited  $\text{e}^-$  in CB changes oxygen to the superoxide radicals and hydroperoxide radicals while positive  $\text{h}^+$  in VB can oxidize the adsorbed water or hydroxyl ions to form hydroxyl radicals Fig. 6. These reactive species (superoxide radicals or hydroperoxide radicals and hydroxyl radicals) can be involved in the degradation of surface adsorbed compounds.

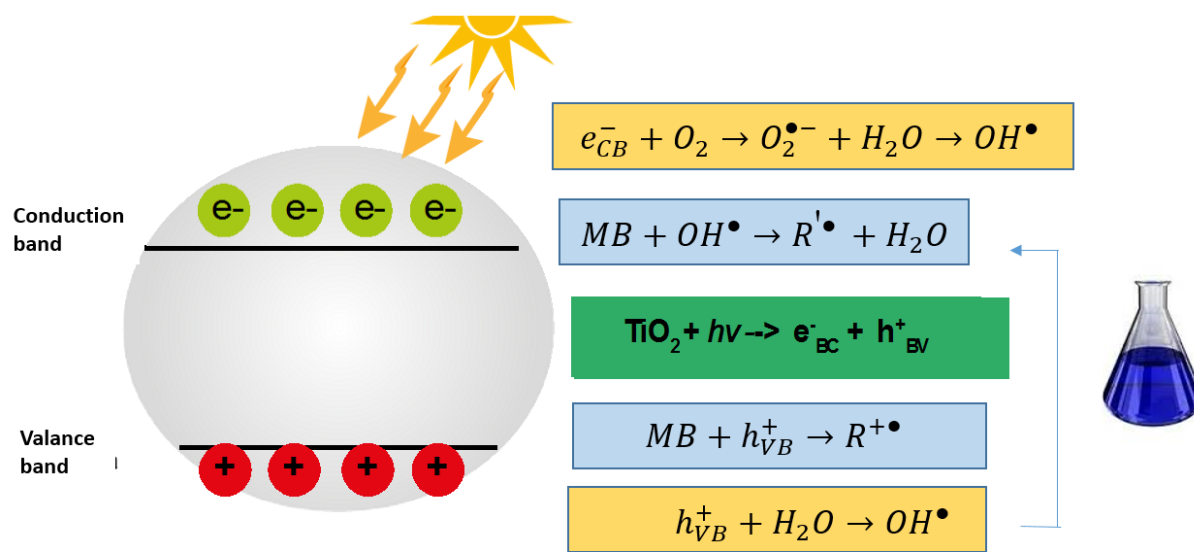
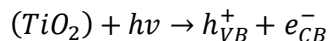


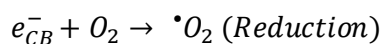
Fig. 6. Photocatalytic process.

The overall process can be summarized as follows:

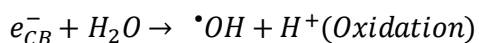
Semiconductor material



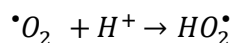
Equation 2



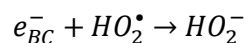
Equation 3



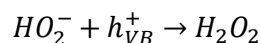
Equation 4



Equation 5



Equation 6



Equation 7

TiO<sub>2</sub> photocatalyst is only restricted to absorb the light in the ultraviolet region (wavelength < 390 nm) due to the wide band gap (3.2 eV for anatase and 3.0 eV for rutile). The photoexcitation of TiO<sub>2</sub> generates the electron/hole pairs. The UV light activity and fast recombination of



electron/hole pairs limit the use of  $\text{TiO}_2$  in visible light and the photocatalytic efficacy, respectively. Because of solar light contains only about 2-3 % UV light, it is necessary to develop  $\text{TiO}_2$  based material which can harvest solar light. Modifications by various strategies have been applied to make the  $\text{TiO}_2$  as visible light active material such as doping with metal and non-metals, co-doping, coupling, etc [17].

## 1.3 Doping of $\text{TiO}_2$

The optical response of any material is largely determined by its underlying electronic structure. The electronic properties of material are closely related to its chemical composition (chemical nature of the bonds between the atoms or ions), its atomic arrangement, and its physical dimension (confinement of carriers) for nanometer-sized materials. The chemical composition of  $\text{TiO}_2$  can be altered by doping. Specifically, the metal (titanium) or the nonmetal (oxygen) component can be replaced to alter the material's optical properties. It is desirable to maintain the integrity of the crystal structure of the photocatalytic host material and to produce favorable changes in electronic structure. It appears easier to substitute the  $\text{Ti}^{4+}$  cation in  $\text{TiO}_2$  with other transition metals, and it is more difficult to replace the  $\text{O}^{2-}$  anion with other anions due to differences in charge states and ionic radii. The small size of the nanoparticle is beneficial for the modification of the chemical composition of  $\text{TiO}_2$  due to the higher tolerance of the structural distortion than that of bulk materials induced by the inherent lattice strain in nanomaterials [6].

### 1.3.1 Metal Doped $\text{TiO}_2$ .

Metal doping has proved to be a successful approach for obtaining photocatalysts with improved photonic efficiencies, generally using less than 10 % of doping species for modifying the semiconductor. With this strategy, it is possible to shift the optical response towards higher wavelengths, increasing the photoactivity under visible irradiation, and to hinder electron-hole recombination. This may allow using sunlight as an inexpensive and renewable energy source in photocatalytic applications. Besides optical absorption, other properties that strongly influence the photocatalytic activity, such as surface area, pore size, density of hydroxyl groups, surface acidity, and adsorption/desorption properties, can also be modulated by incorporating a dopant into the photocatalyst structure.

Impregnation, co-precipitation, ion implantation technique, and sol–gel methods can be employed to incorporate cationic dopants into TiO<sub>2</sub> [18].

Doping by metal ions into the TiO<sub>2</sub> structure (Cationic doping) has demonstrated the efficient method for enhancing the visible light absorption. The electrons injected into CB from VB can be easily transported to the surface of the catalyst and electrons can be easily trapped by doping with transition metals, noble metals, other metals, rare earth elements. Doping of metallic cations enhance the redox potential of the radicals generated during photocatalysis and reduce the e<sup>-</sup>/h<sup>+</sup> recombination lifetime.[17].

### *Surface Dispersion versus Lattice Incorporation*

The presence of dopants can alter the charge transfer properties of TiO<sub>2</sub>, modify the adsorption capacity of its surface, or produce a shift of the absorption edge of the photocatalyst to the visible range. This last modification is highly desirable for a more efficient use of sunlight. It can be associated with a decrease in the band gap, by the interaction of the cation states with the valence or conduction bands of anatase, or with the creation of intra-band-gap states, induced by the incorporation of the dopant ions.

Pronounced redshifts can be obtained using ion implantation processes, which consist of the acceleration of the dopant ions in an electric field and their impact on the semiconductor.

In 1994 [19], a systematic study of quantum-sized (3–4 nm) doped TiO<sub>2</sub> with 21 cations was conducted by Hoffmann and co-workers, who reported on the influence of the metal dopants on the photoreactivity by acting as electron and hole traps, and by altering the electron–hole recombination rate as follows:



with the energy level of M<sup>n+</sup>/M<sup>(n-1)+</sup> located below the conduction band edge and the energy level of M<sup>(n+1)+</sup>/M<sup>n+</sup> above the valence band edge. The presence of these intra-band-gap energy levels would lead to the already mentioned red shift and the photocatalytic response under visible light.

They also observed the existence of an optimum dopant concentration, above which the photoactivity decreases. In the case of quantum-sized particles, this behavior has been attributed to an increasing recombination rate with dopant concentration due to the concomitant decrease in the average distance between trap sites.

An effective absorption of visible light does not always guarantee an enhanced photocatalytic activity under visible irradiation. A dopant can act as an effective mediator of interfacial charge transfer, inhibiting the electron–hole recombination, or it can produce the opposite effect. Despite an extended response in the visible range, metal ions can act as recombination centers, decreasing the photocatalytic activity of the catalyst under UV irradiation

Depending on the dopant, two different situations can be reached, as schematically represented in Fig. 7: (1) a p-type doping, by the introduction of cations with a lower valence than that of  $\text{Ti}^{4+}$  ( $\text{M}^{n+}, n \leq 4$ ), which act as acceptors of electrons; (2) an n-type doping by incorporating electron donors, cations with higher valence than  $\text{Ti}^{4+}$  ( $\text{M}^{n+}, n \geq 5$ ).

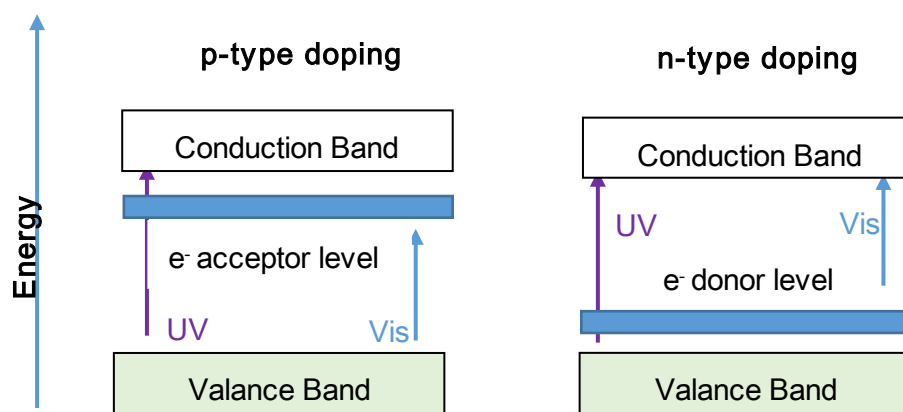


Fig. 7. Schematic representation of the energy levels of doped semiconductors: p-type doping (left) and n-type doping (right).

Metal dopants can occupy substitutional or interstitial sites in the titania lattice or form segregated metal oxide clusters or islands on the surface, depending on nature (primarily electronegativity and ionic radius) and concentration of the doping metal and the synthesis procedure. The inherent lattice strain of nanomaterials facilitates the structural distortion of nanosized  $\text{TiO}_2$  produced by the modification of its chemical composition. Substitutional doping of  $\text{TiO}_2$  will tend to occur when the electronegativity and ionic radius of the doping metal cations match those of  $\text{Ti}^{4+}$ , while

interstitial doping will be preferred if the electronegativity of the doping metal ions approaches that of  $\text{Ti}^{4+}$ , but its ionic radius is smaller. On the other hand, metal ions with larger ionic radii than  $\text{Ti}^{4+}$  present lower solubility in the  $\text{TiO}_2$  lattice, which hinders their substitutional incorporation, and will be more probably found as dispersed metal oxides. In contrast to substitutional doping, a red shift in the absorption spectrum is not expected in the case of surface dispersion. To keep the charge neutrality in the structure of doped  $\text{TiO}_2$ , cation or anion vacancies are created. In these cases, the presence of defects associated with the creation of oxygen vacancies may also contribute to the visible light absorption of the modified  $\text{TiO}_2$ .

The solubility of the metal cations in the anatase structure is governed by parameters such as the primary particle size, the  $M^{n+}/\text{Ti}^{4+}$  radius ratio, and the structural strain, the latter influenced in turn by factors such as the metal oxidation state. A large  $M^{n+}/\text{Ti}^{4+}$  radius ratio favors the presence of oxygen vacancies, which efficiently release strain in the anatase structure. The solubility of  $M^{n+}$  will determine the tendency of the dopant element to form solid solutions, with a homogeneous chemical composition throughout the particle ( $\text{Ti}_{1-x}\text{M}_x\text{O}_2$ ), or to segregate at the surface of  $\text{TiO}_2$ . In any case, at concentrations above the solubility limit of each metal ion, an enrichment of the dopant at the surface is expected, finally leading to the formation of pure  $\text{MO}_x$  phases.

Furthermore, surface or bulk metal doping can stabilize the anatase or the rutile phases of titania and modify the temperature of the anatase-to-rutile transformation. This effect has been ascribed to a hindered crystal growth due to the formation of  $\text{Ti-O-M}$  bonds. It has been suggested that the creation of oxygen vacancies, derived from the incorporation of ions of lower valence than  $\text{Ti}^{4+}$  and relatively small ionic radius, accelerates the phase transition by reducing the strain energy that must be overcome for the rearrangement of the  $\text{Ti-O}$  octahedra and the other way around for ions of higher valence and larger ionic radius. Thus, for instance, the presence of  $\text{Zr}^{4+}$  seems to inhibit this transition, stabilizing the anatase phase at higher temperatures than for bare  $\text{TiO}_2$ . Similarly, doping with Al, Ni, Ga, Nb, Ta, and W has proved to retard the anatase-to-rutile transformation, while Mn, Fe, Cu, or Zn promote, generally, this transition [18].

### 1.3.2 System of TiO<sub>2</sub> doped with Cu.

The metal doping is known as the second generation of photocatalysts and has shown high activity for pollutants degradation. Copper is an important dopant because of its high electronic conductivity; low-cost and is highly available in the earth crust.

Nagaveni et al., [20] doped the titania with metal ions Cu<sup>2+</sup>, V<sup>5+</sup>, Fe<sup>3+</sup>, Zr<sup>4+</sup> by the combustion method, and found that metal ions improve the performance in the 4-nitrophenol degradation in comparison with the commercial TiO<sub>2</sub> pure, Degussa P25.

Xiaoqing Qiu et al., [21], found that the combined effect of Cu in the TiO<sub>2</sub> is beneficial for the photooxidation of the volatile organic compounds.

Wu et al., [22], synthesized a compound of TiO<sub>2</sub> with Cu<sub>2</sub>O clusters for carbon dioxide reduction by the sol-gel method. The study showed that the presence of copper clusters, electrons are enriched owing to the alignment of Fermi levels of the metal and the semiconductor, which is the Schottky barrier. An optimal Cu-loaded titania is a highly efficient photocatalyst for CO<sub>2</sub> reduction since copper is an effective electron trapper, able to reduce the recombination of electron-hole.

Biswakit Choudhury et al., [23], doped TiO<sub>2</sub> with copper by the sol-gel method. The study revealed that copper in the TiO<sub>2</sub> lattice introduces structural defects and promotes the decreasing of crystallite size. Copper introduces d states at the intermediate of the TiO<sub>2</sub> band gap. A simple electron in the orbital d, due to the Jahn-Teller distortion, create a wide absorption peak in the visible region. The octahedral distortion due to the copper doping can be observed in the Fig. 8.

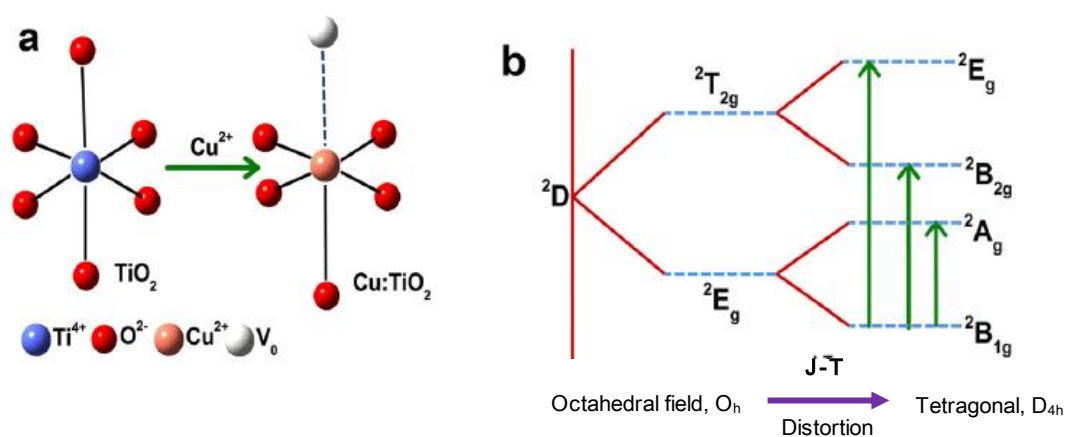


Fig. 8. Schematic representation of the distortion of the TiO<sub>6</sub> octahedra on doping Cu<sup>2+</sup> ion on the Ti<sup>4+</sup> lattice site.

### 1.3.3 System of TiO<sub>2</sub> doped with Ag.

One of the alternative approaches for achieving the threshold of the photo-response of TiO<sub>2</sub> into the visible region is to make a composite semiconductor by modifying TiO<sub>2</sub> with noble metals. These noble metals act separately or simultaneously depending on the photoreaction conditions, experimental methods used and they may (i) enhance the electron-hole separation by acting as electron traps [8–11], (ii) extend the light absorption into the visible range and enhance surface electron excitation by size- and shape-dependent plasmon resonances excited by visible light and/or (iii) modify the surface properties of TiO<sub>2</sub>, [24].

Thus, remarkable efforts have been devoted to overcoming all these limitations by doping/composite with metal, non-metal (NPs), noble metal inclusion or deposition to gain plasmonic property. Decorating with single or bi-noble metal(s) onto semiconductor spinal had proven to trigger the localized surface plasmon resonance (LSPRs) for enhanced visible light photocatalytic activities. A plasmon band is generated due to the collective oscillations of conduction electron induced by the electric field of the incident visible light photons and further potentially declines the recombination rate of photogenerated electron–hole pairs of the semiconductor, as is illustrated in Fig. 9, [25].

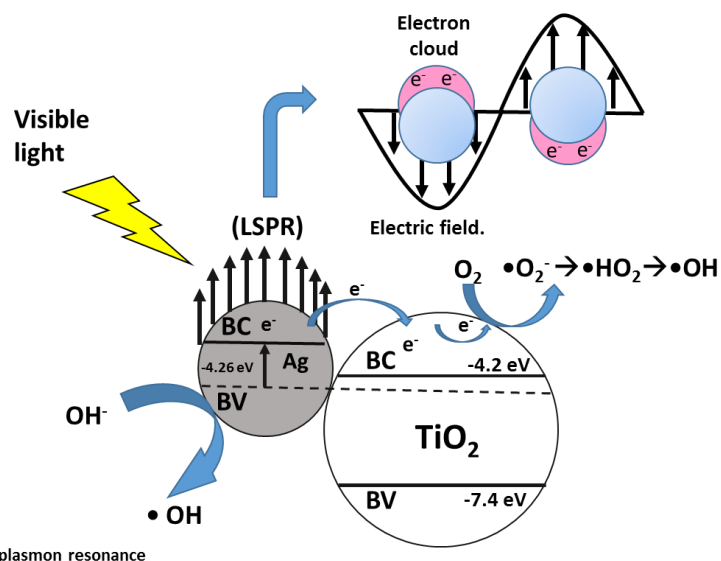


Fig. 9. Schematic diagram of photocatalysis mechanism Ag/TiO<sub>2</sub> photocatalyst under artificial visible light irradiation.

Silver nanoparticles have prospective applications including biosensing, biodiagnostics, optical fibers, and antimicrobial and photocatalytic uses. Silver ions are known to cause denaturation of proteins present in bacterial cell walls and slow down bacterial growth. The simplest photocatalytic mechanism of silver ions is that it may take part in catalytic oxidation reactions between oxygen molecules in the cell and hydrogen atoms of thiol groups, i.e., two thiol groups become covalently bonded to one another through disulfide bonds ( $R-S-S-R$ ), which leads to blocking of respiration and cell death of the bacteria, [26].

Mitsunobu Sato et al., [24], examined thin films of a composite of  $TiO_2$  with silver nanoparticles by the Molecular Precursor method. The study showed that the thin films with silver loading less than 40% mol are not effective under vis-irradiation, though they can work as a photocatalyst under UV-irradiation. Contrarily, the composite thin films of Ag content larger than 50 mol% showed the vis-responsive activity, whose level was slightly lower than the decreased UV-sensitivity.

Ashutosh Pandey et al., [26], synthesized  $TiO_2$  doping with silver by the sol-gel method for antibacterial purpose. The results showed that the doping systems have a shifting of the absorption edge to the visible region. The antibacterial efficiency increase for the  $TiO_2$  doping with silver in comparison with the  $TiO_2$  pure, due to decreasing of electron/hole recombination, according to the photoluminescence test.

Surface deposition of silver nanoparticles (Ag NPs) onto the 100% anatase titania ( $Ag/TiO_2$ ) for the evolution of surface plasmon resonance (SPR) was achieved sustainably with the assistance of solar energy was studied by Pichiah Saravanan et al., [25]. The synthesized plasmonic photocatalyst  $Ag/TiO_2$  unveiled an impressive photocatalytic activity for EDCs degradation under artificial visible light. Beside they established the photocatalysis mechanism of  $TiO_2$  doping with silver. When  $Ag/TiO_2$  is exposed to visible light irradiation, the electrons below the Fermi level ( $E_f$ ) of the Ag NPs will be excited to the surface plasmon states, leaving positive charges ( $h^+$ ) below the  $E_f$ . Thus, with the contact of Ag NPs on the surface of  $TiO_2$ , the energetic electrons from Ag will be excited to the CB of  $TiO_2$ . As the CB of  $TiO_2$  is an electron acceptor, it readily accepts the electrons and forms superoxide anion radicals ( $\bullet O_2^-$ ) and followed by the protonation that yields  $\bullet HO_2$  radicals. This  $\bullet HO_2$  radicals easily combines with the trapped electrons resulting into  $H_2O_2$  and finally forming a photodegradation active species  $\bullet OH$  radicals. Moreover, the Schottky

barrier was formed at the interface of Ag–TiO<sub>2</sub> because the Fermi level of TiO<sub>2</sub> is higher than that of Ag which will hinder the transfer of an electron from the Ag to TiO<sub>2</sub>. However, it is proven that electrons can transfer from the Ag to TiO<sub>2</sub> due to its strong electron oscillating collectively on the SPR excitation. These lead to interband excitation giving sufficient energy to the electrons to overcome the Schottky barrier at the interface. Thus it triggers the energetic electron to be transferred to the CB of TiO<sub>2</sub> and lead to the enriched formation of •OH radicals thus enhancing the photocatalytic oxidation.



### 1.3.4 Non-metal doping of TiO<sub>2</sub>.

Nonmetal-doped TiO<sub>2</sub> nanomaterials have been regarded as the third generation photocatalyst. Various nonmetal doped TiO<sub>2</sub> nanomaterials have been widely studied for their visible light photocatalytic activities. Nonmetal-doped TiO<sub>2</sub> nanomaterials have been demonstrated to have improved photocatalytic activities compared to those for pure TiO<sub>2</sub> nanomaterials, especially in the visible light region.[6].

It is known that the TiO<sub>2</sub> doped with Nitrogen, has a higher photocatalytic activity under the visible than pure TiO<sub>2</sub>. However, it showed less activity in the UV light, [27].

Titania doping with Sulphur has shown a very similar behavior, with high activity in the visible region and low activity in the UV light, however, depending on the synthesis conditions the visible light absorption will change, due to the different charge behavior of the samples, [28].

In metal-doped TiO<sub>2</sub>, the cations replace titanium atoms; meanwhile, in the non-metal-doped TiO<sub>2</sub>, the anionic dopants are expected to substitute the oxygen atoms, although cationic substitutions may take place as well with some non-metals. Even though titania with partial substitution at the oxygen sites is usually represented in the literature as TiO<sub>2-x</sub>A<sub>x</sub>, where A is the anion, this representative formula must be carefully employed and seems questionable for very low A/Ti ratios.

The aim of absorbing radiation less energetic than UV-A requires the band-gap narrowing, by the elevation of the valence band maximum, the lowering of the conduction band minimum or the introduction of localized energy levels, [18].

The main requirements for the anionic dopant to elevate the valence band maximum are the following [29]:

1. Lower electronegativity than oxygen, so that the dopant states can be involved in the formation of a new valence band at a higher energy level. The Pauling electronegativity of O is 3.4, higher than that of all non-metals, except F, with an electronegativity of 3.98.
2. Similar size to that of lattice O atoms, so that the substitutional anions do not alter the structure uniformity and, thus, the intrinsic properties of the semiconductor. N presents the most similar anionic radius.

Many successful photocatalysts have been synthesized. The main challenge remains to achieve higher photocatalytic activity under visible than under ultraviolet light. Therefore, the optimization of the dopants choice and doping strategies continues, [18].

### 1.3.5 Doping with rare earth.

Luminescent nanomaterials have gained considerable attention in recent years due to the breakthrough developments of technology in various areas such as electronics, photonics, displays, optical amplifications, lasers, fluorescent sensing, biomedical engineering, [9] and environmental control. The long emission lifetime and rich spectral properties of certain rare-earth [RE] ions are highly attractive in many ways. However, RE ions alone are weakly fluorescent due to the parity forbade f-f transitions. Therefore, the use of host materials is crucial to excite the RE ions efficiently in a wide spectral range to utilize their full potential in optoelectronic devices. Oxide lattices have proved to be an excellent host material due to their good thermal, chemical, and mechanical stabilities. Among them,  $\text{Y}_2\text{O}_3$  is a promising host for RE ions due to its low phonon frequencies, which make the nonradiative relaxation of the excited states inefficient. However, the high costs associated with synthesis have restricted its further use. As an alternative,  $\text{TiO}_2$ , a well-known wide bandgap semiconductor, has demonstrated the possibility to be a good sensitizer to absorb light and transfer energy to RE ions. Moreover, the high refractive index and high transparency of  $\text{TiO}_2$  in the visible and infrared regions make it possible to use in optical devices, [30].

Doping  $\text{TiO}_2$  with rare earth metals increases the photoactivity of nitrite oxidation in the following order:  $\text{Gd}^{3+} > \text{Nd}^{3+} > \text{La}^{3+} > \text{Pr}^{3+} (\text{Er}^{3+}) > \text{Ce}^{3+} > \text{Sm}^{3+}$ . The photodegradation rate is higher than that for bare  $\text{TiO}_2$  due to the higher absorption (red shift) and an increase of interfacial electron rate. The highest enhancement in photoactivity is obtained for ca. 0.5 wt% rare-earth-ion doping (which may favor an efficient separation of the charge carriers), [31].

Furthermore, owing to its good mechanical, optical, and thermal properties,  $\text{TiO}_2$  is believed to be the ideal host system for incorporating rare-earth (RE) impurity ions as dopants. One of the major advantages offered by these materials is the ability to tailor size dependent optical properties and to achieve high luminescence response through the sensitization by the host. Several reports have demonstrated the intense  $\text{RE}^{3+}$  emission of RE incorporated  $\text{TiO}_2$  nanoscale systems along

with a suitable explanation of the energy transfer mechanism. On the other hand, the RE ions can promote the degradation process (photocatalysis) of many hazardous pollutants and dyes through active interaction with the organic molecules of the pollutants. The incorporation of lanthanide ions into the  $\text{TiO}_2$  host may help organic pollutants to concentrate on the semiconductor surface, [32].

Substitution of  $\text{Ti}^{4+}$  by  $d^n$  metallic ions in the  $\text{TiO}_2$  lattice creates allowed energy states in the band gap of  $\text{TiO}_2$ , which may induce photoactive transitions in the visible light, due to an excitation of an electron from this energy level into the  $\text{TiO}_2$  conduction band [5, 33].

Lanthanide ions are known for their ability to form complexes with various Lewis bases (e.g., acids, amines, aldehydes, alcohols, thiols, etc.) through the interaction of these functional groups with the f-orbitals of the lanthanides [5].

### 1.3.6 System of $\text{TiO}_2$ doping with Eu.

Compared to other trivalent RE ions,  $\text{Eu}^{3+}$  gives strong red emission due to intra 4f carrier transitions thus making the system more useful in technologically important optoelectronic and display elements. Besides that, Eu-doped  $\text{TiO}_2$  nanomaterials could exhibit better photocatalytic activity as compared to their undoped counterpart. This is because of generation of an adequate number of electron trap centers by  $\text{Eu}^{3+}$  ions [32].

However, due to the large mismatch of ionic radii ( $\text{Eu}^{3+} = 0.95 \text{ \AA}$  and  $\text{Ti}^{4+} = 0.68 \text{ \AA}$ ) and charge imbalance between the  $\text{Ti}^{4+}$  and  $\text{Eu}^{3+}$  ions, successful incorporation of Eu ions into  $\text{TiO}_2$  nanocrystals through a soft, wet-chemical route remains a great challenge. In most of the cases,  $\text{Eu}^{3+}$  ions either tend to locate on a crystal surface, causing an undesired Eu-Eu interaction, or form  $\text{Eu}_2\text{O}_3$  aggregates, which act as quenching sites, resulting in a drastic decrease in the luminescent intensity, [30].

Mou Pal et al., [30], doped  $\text{TiO}_2$  with Eu by the sol-gel method with different doping concentrations, and shown that as the Europium content increase the size of the particles decrease, suggesting that Europium suppresses the growth of  $\text{TiO}_2$  nanoparticles. Besides, the induced crystallization reduces the photoluminescence intensity, suggesting amorphous  $\text{TiO}_2$  as an ideal framework for an efficient energy transfer between the titania host and incorporated  $\text{Eu}^{3+}$  ions. Electrons are

initially excited to the conduction band of  $\text{TiO}_2$  on irradiating UV light and then relaxed to the defect states. Since the defect states of  $\text{TiO}_2$  are located at higher energies than those of the emitting state ( $^5\text{D}_0$ ) of  $\text{Eu}^{3+}$  ions, energy transfer to the crystal field states ( $^7\text{F}_j$ ) of  $\text{Eu}^{3+}$  occurs, resulting in efficient PL.

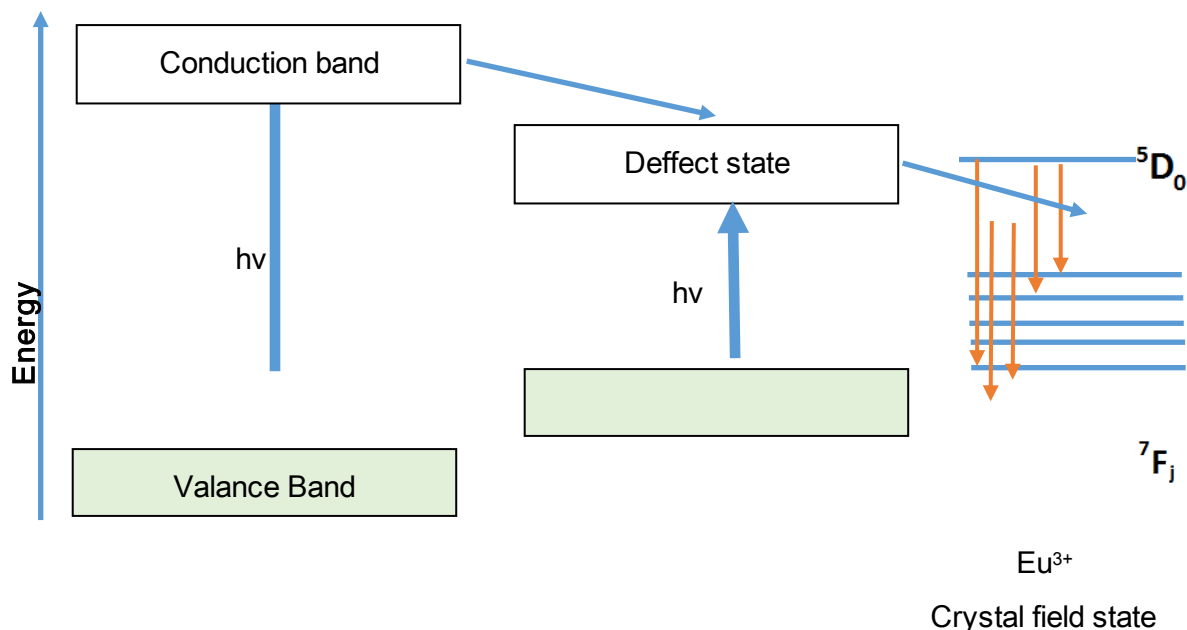


Fig. 10. Schematic illustration of the possible mechanism of energy transfer from the  $\text{TiO}_2$  host to  $\text{Eu}^{3+}$ .

Dambarudhar et al., [32], doped  $\text{TiO}_2$  by the sol-gel method, and found that systems with Europium content of 1 to 5 %mol increased the photocatalytic activity,. The reason for the increased photodegradation efficiency is ascribed to the introduction of  $\text{Eu}^{3+}$  doping states, which helped to inhibit  $e^-/h^+$  pair recombination while enhancing interfacial charge.  $\text{Eu}$ -doped  $\text{TiO}_2$  nanoparticles is a better choice over the undoped ones, owing to the effective free radical generation via participation of new energy levels and lower rate of  $e^-$  and  $h^+$  recombination that would facilitate photocatalytic reactions.

## 1.4 Morphological modification of the semiconductors.

The uses of different types of nanostructured materials in dye-sensitized solar cells (DSSC) have attracted worldwide attention as a low-cost alternative to traditional photovoltaic devices.

Typically, nanoporous film based on  $\text{TiO}_2$  nanoparticles ( ~20 nm in diameter) has shown high energy conversion efficiency due to large amounts of adsorbed dye molecules. However, when the photoexcited electrons are excited and pass through the interparticle grain boundaries or suffer surface trapping/detrapping effects, the subsequent electron accumulation can enhance the recombination probability, causing restricted performance of solar cells, [34].

Nowdays a model exists for the recombination explanation. In a solar cell when current is drawn from the cell, injected electrons move toward the anode contact either by hopping between sites (the hopping model) or by a random walk process in which the electrons spend some time immobilized in trap sites from which they are excited thermally back to the conduction band (the multiple trapping model). In either model, the electrons may be localized near the surface or in bulk, [35, 36].

However it was found that using one-dimensional (1-D)  $\text{TiO}_2$  (in the form of nanotubes, nanowires, nanofibers, and nanorods) as the photoanode material for DSSCs significantly improved the charge collection, by providing a highway to transport photoelectrons, which consequently minimizes the recombination and increase the electron lifetime [34]. The Fig. 11 shows two models of charge recombination in a semiconductor nanoparticle. In both cases, cations are immobile, while electrons can move between trap sites on the surface of the nanoparticle by thermal activation to the conduction band. The model of Nelson et al., is shown on the left and corresponds to the nearest neighbor random walk. The random flight model on the right corresponds to a completely random choice of the next trapping site for an electron within the nanoparticle after its detrapping and diffusion in the conduction band [36].

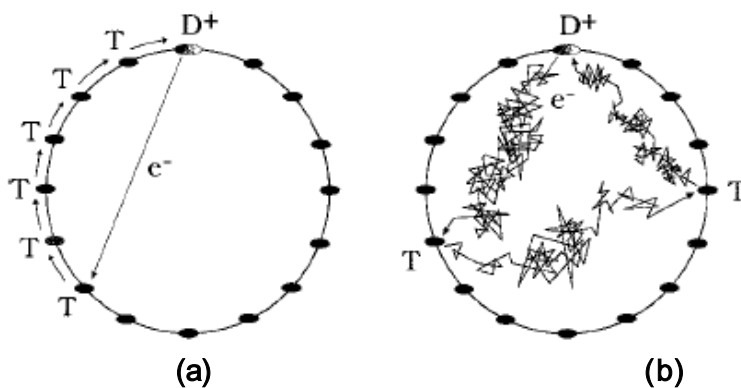


Fig. 11 Models of charge recombination in a semiconductor particle; a) Surface trapping sites and b) Within particle trapping sites.

### 1.4.1 Unidimensional structure.

Recently, various one-dimensional (1D) nanostructures, including nanowires (NW), nanorods (NR), and nanotubes (NT), have attracted much interest due to their advantages for charge carrier transport and interfacial recombination. However, there are still some technical problems and challenges in these pure 1D nanostructures, such as lower dye loading and lower effective surface area, resulting in lower energy conversion efficiency compared with the 3D-TiO<sub>2</sub> nanoparticles. The combined nanostructure (TP) consisted of 1D-nanotubes and 3D-nanoparticles can combine each advantage of 1D and 3D nanostructure, and thus is promising to exhibit higher energy conversion efficiency, [37].

In the last 30 years of research, the particulate form of titanium dioxide (TiO<sub>x</sub>; x~2) has been the most widely studied photocatalyst for a variety of light-driven reactions. Admittedly, some pressing and yet-to-be-resolved issues regarding TiO<sub>2</sub> nanoparticles (T\_NPs), nanoparticulate films, and monoliths include inefficient light absorption and e<sup>-</sup>/h<sup>+</sup> separation deficiency.

In contrast, the performance of one-dimensional (1D) nanostructures of TiO<sub>x</sub>—nanotubes or nanorods—has been reported to exhibit much better performance than nanoparticulate systems; the much lower number of grain boundaries in the 1D nanostructures is believed to allow improved charge separation as shown in Fig. 12, [38].

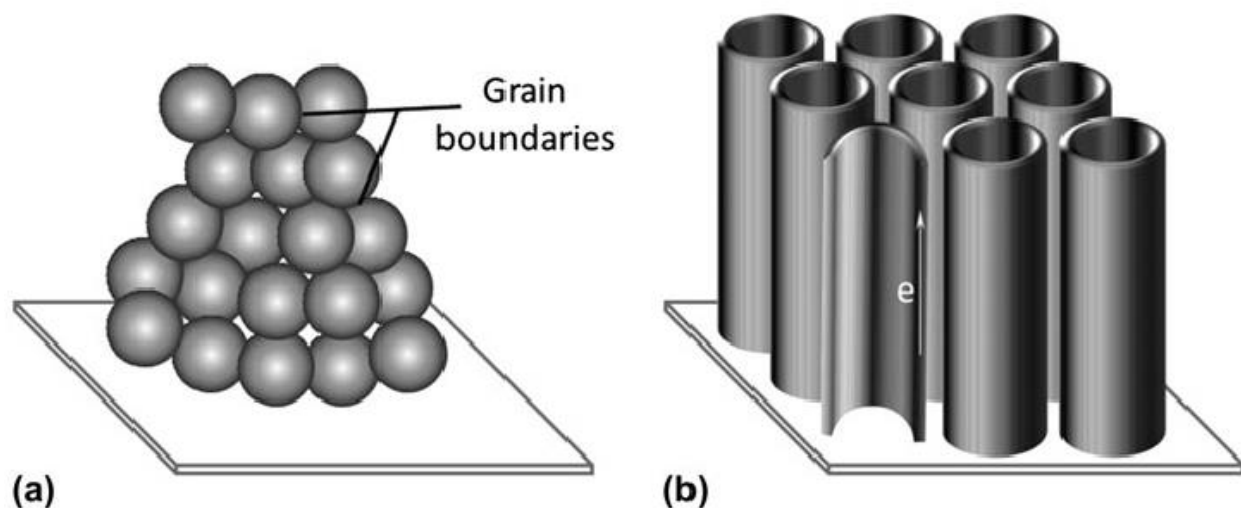


Fig. 12. The key difference between the (a) particulate and (b) nanotubular film architecture is the large presence of inter-particle grain boundaries as shown in this representative schematic with  $\text{TiO}_2$  films as an example oxide photocatalyst.

### ***Tubular morphology for photovoltaic applications.***

$\text{TiO}_2$  nanotubes (TNTs) have recently garnered considerable interest as an effective photocatalyst due to their various advantages promoted by their microstructure, such as a large specific surface area and high pore volume. TNTs can absorb a considerable amount of pollutants because of their large specific surface areas and high pore volumes, and this adsorption plays an important role in the degradation of those pollutants, [39].

$\text{TiO}_2$  nanotubes are expected to have advantages over  $\text{TiO}_2$  particles. First, their one-dimensional structure can reduce the transport dimensionality and recombination of the photoinjected electrons. Second, their tubular structure provides a large area for hosting dye molecules and receiving illumination. Nonetheless, many technical issues remain to be dealt with before the  $\text{TiO}_2$  nanotube-based DSSCs can finally mature, [40].

Hoda S. Hafez [41], synthesized  $\text{TiO}_2$  nanotubes by the hydrothermal method in a KOH/NaOH solution. The semiconductor was successfully tested in the degradation of the commercial

Cibacrown Red (FN-R) textile dye, under UV radiation. Single crystalline anatase  $\text{TiO}_2$  nanorods are more efficient for the dye removal.

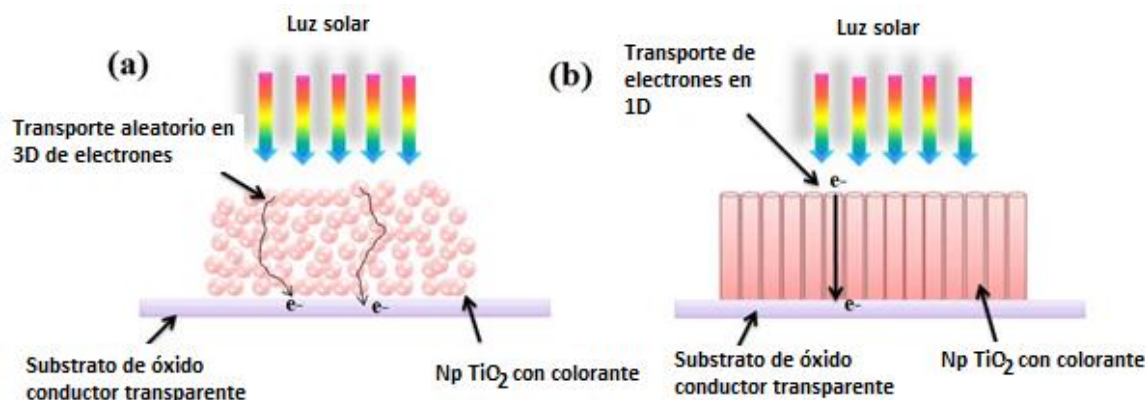


Figure 3 Dye sensitized solar cell: a) particles b) nanotubes [42].

Wook Choi *et al.*, [11], found that the efficiency of dye-sensitized solar cells [DSSCs] was enhanced by combining the use of  $\text{TiO}_2$  nanotubes [TNTs] and nanoparticles. The nanotubes were fabricated by the hydrothermal method. Besides the study showed that the morphology properties changes depending on the hydrothermal temperature conditions. The major photovoltaic performance was achieved when a mix of nanotubes and nanoparticles is used in the DSSC.

Ana Flávia Nogueira *et al.*, [43], fabricated nanotubes by the sol-gel and hydrothermal method, and found that nanotubes have a high superficial area allowing much more dye to be chemically absorbed and creates an ample ion path for fast ionic motion from the bulk to the inner parts of the film. Solar cells assembled by combining the  $\text{TiO}_2$  nanotubes and the plasticized polymer electrolyte exhibited an overall efficiency of 4.03% at  $100 \text{ mW cm}^{-2}$ , higher than the devices assembled solely with  $\text{TiO}_2$  nanoparticles.

Changjian Lin *et al.*, [37], fabricated a combined structure with a mixture of  $\text{TiO}_2$  nanotubes and particles by anodization of a dispersion of  $\text{TiO}_2$  nanoparticles were uniformly dispersed on the surface of  $\text{TiO}_2$  nanotubes with the diameter of 110-130 nm and the length of 15  $\mu\text{m}$ . It was found



that the energy conversion efficiency of the solar cell with composite photoanode was 5.75%, enhanced up to 25.8% compared to that of the photoanode of pure TiO<sub>2</sub> nanotube structure in the same condition.

*Yuan Lin* et al., [44], prepared an electrophoretical deposition of nanoparticles inside the nanotubes to increase the surface area for dye loading. The dye loading increased 47.2% after depositing the nanoparticles. A conversion efficiency of 6.28% was achieved for DSSCs with a flexible photoanode.


*Xia Tao* et al., [45], fabricated a photoanode with bilayer-structured film with TiO<sub>2</sub> nanocrystals as underlayer and TiO<sub>2</sub> nanotubes as overlayer. The charge recombination behavior of cells was investigated by electrochemical impedance spectra, and the results showed that double layer-TiO<sub>2</sub> film-based cell possessed the lowest transfer resistance and the longest electron lifetime.

## 1.5 Bibliography.

1. Cronemeyer, D.C., *Electrical and optical properties of rutile single crystals*. Physical Review, 1952. **87**(5): p. 876.
2. Banerjee, A.N., *The design, fabrication, and photocatalytic utility of nanostructured semiconductors: focus on TiO<sub>2</sub>*. Nanotechnology, science and applications, 2011. **4**: p. 35-65.
3. Brian, O.R. and G. Michael, *A low-cost, high-efficiency solar cell based on dye-sensitized colloidal TiO<sub>2</sub> films*. Nature, 1991. **353**(6346): p. 737-740.
4. Perez-Flores, J.C., C. Baehtz, A. Kuhn, and F. Garcia-Alvarado, *Hollandite-type TiO<sub>2</sub>: a new negative electrode material for sodium-ion batteries*. Journal of Materials Chemistry A, 2014. **2**(6): p. 1825-1833.
5. Carp, O., C.L. Huisman, and A. Reller, *Photoinduced reactivity of titanium dioxide*. Progress in Solid State Chemistry, 2004. **32**(1-2): p. 33-177.
6. Chen, X. and S.S. Mao, *Titanium dioxide nanomaterials: synthesis, properties, modifications, and applications*. Chem Rev, 2007. **107**(7): p. 2891-959.
7. Quiroz, M.A., C.A. Martínez-Huitle, and E.R. Bandala, *Advanced oxidation processes (AOPs) for removal of pesticides from aqueous media*. 2011: INTECH Open Access Publisher.
8. Brus, L., *A simple model for the ionization potential, electron affinity, and aqueous redox potentials of small semiconductor crystallites*. The Journal of chemical physics, 1983. **79**(11): p. 5566-5571.
9. Prakash, T., *Review on nanostructured semiconductors for dye sensitized solar cells*. Electronic Materials Letters, 2012. **8**(3): p. 231-243.
10. Chen, X., *Titanium Dioxide Nanomaterials and Their Energy Applications*. Chinese Journal of Catalysis, 2009. **30**(8): p. 839-851.
11. Lee, C.H., S.W. Rhee, and H.W. Choi, *Preparation of TiO<sub>2</sub> nanotube/nanoparticle composite particles and their applications in dye-sensitized solar cells*. Nanoscale Research Letters, 2012. **7**(1): p. 48.
12. Navas, J., C. Fernández-Lorenzo, T. Aguilar, R. Alcántara, and J. Martín-Calleja, *Improving open-circuit voltage in DSSCs using Cu-doped TiO<sub>2</sub> as a semiconductor*. physica status solidi (a), 2012. **209**(2): p. 378-385.
13. Smestad, G.P. and M. Gratzel, *Demonstrating Electron Transfer and Nanotechnology: A Natural Dye-Sensitized Nanocrystalline Energy Converter*. Journal of Chemical Education, 1998. **75**(6): p. 752.
14. Fujishima, A. and K. Honda, *Photolysis-decomposition of water at the surface of an irradiated semiconductor*. Nature, 1972. **238**(5385): p. 37-38.
15. Frank, S.N. and A.J. Bard, *Heterogeneous photocatalytic oxidation of cyanide ion in aqueous solutions at titanium dioxide powder*. Journal of the American Chemical Society, 1977. **99**(1): p. 303-304.
16. Hashimoto, K., H. Irie, and A. Fujishima, *TiO<sub>2</sub> photocatalysis: a historical overview and future prospects*. Japanese journal of applied physics, 2005. **44**(12R): p. 8269.
17. Barakat, M.A. and R. Kumar, *Photocatalytic Activity Enhancement of Titanium Dioxide Nanoparticles*, in *Photocatalytic Activity Enhancement of Titanium Dioxide Nanoparticles*. 2016, Springer. p. 1-29.
18. Coronado, J.M., F. Fresno, M.D. Hernández-Alonso, and R. Portela, *Design of advanced photocatalytic materials for energy and environmental applications*. 2013: Springer.

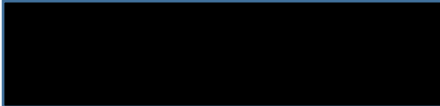
19. Choi, W., A. Termin, and M.R. Hoffmann, *The role of metal ion dopants in quantum-sized TiO<sub>2</sub>: correlation between photoreactivity and charge carrier recombination dynamics*. The Journal of Physical Chemistry, 1994. **98**(51): p. 13669-13679.
20. Nagaveni, K., M.S. Hegde, and G. Madras, *Structure and Photocatalytic Activity of Ti<sub>1-x</sub>M<sub>x</sub>O<sub>2±δ</sub> (M = W, V, Ce, Zr, Fe, and Cu) Synthesized by Solution Combustion Method*. The Journal of Physical Chemistry B, 2004. **108**(52): p. 20204-20212.
21. Qiu, X., M. Miyauchi, K. Sunada, M. Minoshima, M. Liu, Y. Lu, D. Li, Y. Shimodaira, Y. Hosogi, Y. Kuroda, and K. Hashimoto, *Hybrid CuxO/TiO<sub>2</sub> Nanocomposites As Risk-Reduction Materials in Indoor Environments*. ACS Nano, 2012. **6**(2): p. 1609-1618.
22. Tseng, I.H., W.-C. Chang, and J.C.S. Wu, *Photoreduction of CO<sub>2</sub> using sol-gel derived titania and titania-supported copper catalysts*. Applied Catalysis B: Environmental, 2002. **37**(1): p. 37-48.
23. Choudhury, B., M. Dey, and A. Choudhury, *Defect generation, dd transition, and band gap reduction in Cu-doped TiO<sub>2</sub> nanoparticles*. International Nano Letters, 2013. **3**(1): p. 1-8.
24. Daniel, L.S., H. Nagai, N. Yoshida, and M. Sato, *Photocatalytic activity of vis-responsive Ag-nanoparticles/TiO<sub>2</sub> composite thin films fabricated by molecular precursor method (MPM)*. Catalysts, 2013. **3**(3): p. 625-645.
25. Leong, K.H., B.L. Gan, S. Ibrahim, and P. Saravanan, *Synthesis of surface plasmon resonance (SPR) triggered Ag/TiO<sub>2</sub> photocatalyst for degradation of endocrine disturbing compounds*. Applied Surface Science, 2014. **319**(0): p. 128-135.
26. Gupta, K., R. Singh, A. Pandey, and A. Pandey, *Photocatalytic antibacterial performance of TiO<sub>2</sub> and Ag-doped TiO<sub>2</sub> against S. aureus. P. aeruginosa and E. coli*. Beilstein journal of nanotechnology, 2013. **4**(1): p. 345-351.
27. Takeshi, M., A. Ryoji, O. Takeshi, A. Koyu, and T. Yasunori, *Band-Gap Narrowing of Titanium Dioxide by Nitrogen Doping*. Japanese journal of applied physics, 2001. **40**(6A): p. L561.
28. Takeshita, K., A. Yamakata, T.-a. Ishibashi, H. Onishi, K. Nishijima, and T. Ohno, *Transient IR absorption study of charge carriers photogenerated in sulfur-doped TiO<sub>2</sub>*. Journal of Photochemistry and Photobiology A: Chemistry, 2006. **177**(2-3): p. 269-275.
29. Liu, G., L. Wang, H.G. Yang, H.-M. Cheng, and G.Q. Lu, *Titania-based photocatalysts-crystal growth, doping and heterostructuring*. Journal of Materials Chemistry, 2010. **20**(5): p. 831-843.
30. Pal, M., U. Pal, J.M. Jimenez, and F. Perez-Rodriguez, *Effects of crystallization and dopant concentration on the emission behavior of TiO<sub>2</sub>:Eu nanophosphors*. Nanoscale Res Lett, 2012. **7**(1): p. 1.
31. Xu, A.-W., Y. Gao, and H.-Q. Liu, *The Preparation, Characterization, and their Photocatalytic Activities of Rare-Earth-Doped TiO<sub>2</sub> Nanoparticles*. Journal of Catalysis, 2002. **207**(2): p. 151-157.
32. Paul, N. and D. Mohanta, *Effective optoelectronic and photocatalytic response of Eu<sup>3+</sup>-doped TiO<sub>2</sub> nanoscale systems synthesized via a rapid condensation technique*. Journal of Materials Research, 2013. **28**(11): p. 1471-1480.
33. Borgarello, E., J. Kiwi, M. Graetzel, E. Pelizzetti, and M. Visca, *Visible light induced water cleavage in colloidal solutions of chromium-doped titanium dioxide particles*. Journal of the American Chemical Society, 1982. **104**(11): p. 2996-3002.
34. Hong, C.K., Y.H. Jung, H.J. Kim, and K.H. Park, *Electrochemical properties of TiO<sub>2</sub> nanoparticle/nanorod composite photoanode for dye-sensitized solar cells*. Current Applied Physics, 2014. **14**(3): p. 294-299.
35. Jennings, J.R., A. Ghicov, L.M. Peter, P. Schmuki, and A.B. Walker, *Dye-Sensitized Solar Cells Based on Oriented TiO<sub>2</sub> Nanotube Arrays: Transport, Trapping, and Transfer of Electrons*. Journal of the American Chemical Society, 2008. **130**(40): p. 13364-13372.

36. Barzykin, A.V. and M. Tachiya, *Mechanism of Charge Recombination in Dye-Sensitized Nanocrystalline Semiconductors: Random Flight Model*. The Journal of Physical Chemistry B, 2002. **106**(17): p. 4356-4363.
37. Zheng, D., M. Lv, S. Wang, W. Guo, L. Sun, and C. Lin, *A combined TiO<sub>2</sub> structure with nanotubes and nanoparticles for improving photoconversion efficiency in dye-sensitized solar cells*. Electrochimica Acta, 2012. **83**(0): p. 155-159.
38. Subramanian, V.R., S. Sarker, B. Yu, A. Kar, X. Sun, and S.K. Dey, *TiO<sub>2</sub> nanotubes and its composites: Photocatalytic and other photo-driven applications*. Journal of Materials Research, 2013. **28**(3): p. 280-293.
39. Lee, D.-S., S.-Y. Lee, K.Y. Rhee, and S.-J. Park, *Effect of hydrothermal temperature on photocatalytic properties of TiO<sub>2</sub> nanotubes*. Current Applied Physics, 2014. **14**(3): p. 415-420.
40. Li, S., Y. Liu, G. Zhang, X. Zhao, and J. Yin, *The role of the TiO<sub>2</sub> nanotube array morphologies in the dye-sensitized solar cells*. Thin Solid Films, 2011. **520**(2): p. 689-693.
41. Hafez, H.S., *Synthesis of highly-active single-crystalline TiO<sub>2</sub> nanorods and its application in environmental photocatalysis*. Materials Letters, 2009. **63**(17): p. 1471-1474.
42. Mukul, D. and H.A. Hongshan, *Morphological and Photovoltaic Studies of TiO<sub>2</sub> NTs for High Efficiency Solar Cells*. Scanning Electron Microscopy. 2012.
43. Flores, I.C., J.N. de Freitas, C. Longo, M.-A. De Paoli, H. Winnischofer, and A.F. Nogueira, *Dye-sensitized solar cells based on TiO<sub>2</sub> nanotubes and a solid-state electrolyte*. Journal of Photochemistry and Photobiology A: Chemistry, 2007. **189**(2-3): p. 153-160.
44. Xue, Z., W. Zhang, X. Yin, Y. Cheng, L. Wang, and B. Liu, *Enhanced conversion efficiency of flexible dye-sensitized solar cells by optimization of the nanoparticle size with an electrophoretic deposition technique*. RSC Advances, 2012. **2**(18): p. 7074-7080.
45. Xu, H., X. Tao, D.-T. Wang, Y.-Z. Zheng, and J.-F. Chen, *Enhanced efficiency in dye-sensitized solar cells based on TiO<sub>2</sub> nanocrystal/nanotube double-layered films*. Electrochimica Acta, 2010. **55**(7): p. 2280-2285.



# **CHAPTER II**

## **Metal doping of TiO<sub>2</sub> powders**



### **II. Metal doping of TiO<sub>2</sub> powders.**

#### **2.1 Synthesis of TiO<sub>2</sub> doped with metallic ions.**

TiO<sub>2</sub> nanomaterials have been synthesized by the sol-gel method, a widely used method in making various ceramic materials. In a typical sol-gel process, the hydrolysis of titanium alkoxide or halide precursor and subsequent condensation finally lead to the formation of the TiO<sub>2</sub> inorganic framework. This process normally proceeds via an acid controlled hydrolysis step of titanium (IV) alkoxide followed by condensation. The development of Ti-O-Ti chains through alkoxylation is favored for low content of water, with low hydrolysis rates and excess titanium alkoxide in the reaction mixture. Three-dimensional polymeric skeletons with close packing result from the development of Ti-O-Ti chains since a part of the Ti are coordinated with O atoms [1].

### 2.1.1 $\text{TiO}_2$ doping with Cu.

The doping with metal ions induces effects on the photocatalytic activity of  $\text{TiO}_2$ . Some authors claim that the metal doping should decrease the photo threshold energy of  $\text{TiO}_2$ , producing a significant band gap narrowing, which allows lowering the energy consumption; meanwhile, other authors consider that the metal doping could work as a recombination center for electrons and holes, avoiding a fast recombination; and thus increasing the  $\text{TiO}_2$  photoreactivity [2].

### 2.1.2 $\text{TiO}_2$ doping with Ag.

In the recent years the plasmonic driven photocatalysts achieved with the support of noble metal(s) has become a key focus in many studies. Decorating with single or bi-noble metal(s) onto semiconductor spinals had proven to trigger the localized surface plasmon resonance (LSPRs) for enhanced visible light photocatalytic activities. A plasmon band is generated due to the collective oscillations of conduction electron induced by the electric field of the incident visible light photons and further potentially declines the recombination rate of photogenerated electron-hole pairs of the semiconductor [3].

### 2.1.3 $\text{TiO}_2$ doping with Eu.

Lanthanide ions are known for their ability to form complexes with various Lewis bases (e.g., acids, amines, aldehydes, alcohols, thiols, etc.) in the interaction of these functional groups with the f-orbitals of lanthanides [4]. The incorporation of lanthanide ions into the  $\text{TiO}_2$  host may help organic pollutants to concentrate on the semiconductor surface.[5]. According to Xu et al., the  $\text{TiO}_2$  doping with lanthanides increase the photocurrent, and it implies an effective separation of electron-hole pairs [6].

### 2.1.4 Experimental design.

The  $\text{TiO}_2$  doping with metallic elements was made according to the following experimental designs:

In early studies, anatase  $\text{TiO}_2$  was believed to be a more efficient photocatalyst than rutile  $\text{TiO}_2$  due to its higher Fermi level and a higher degree of hydroxylation [7]. On the other hand, the incorporation of doping ions can modify the phase temperature transition from anatase phase to

rutile. Therefore a variation in the thermal treatment temperature was made to stabilize the anatase phase according to the XRD results. Only samples of  $TiO_2$  doping with 3% mol were employed for this experimental design showed in Table 1.

Table 1. Experimental design for the  $TiO_2$  doped with metallic ions (3% mol) by the temperature variation.

$TiO_2$	$TiO_2$ :3%Cu	$TiO_2$ :3%Ag	$TiO_2$ :3%Eu
500° C			
600° C		650° C	
700° C			
800° C		800° C	

When the temperature of the stable Anatase phase was found, the doping with 1, 2 and 3% mol was made, according to the experimental design in Table 2. The structural, electronic and optical properties of  $TiO_2$  was studied and finally, the dye degradation was evaluated (photocatalytic test).

Table 2. Experimental design for  $TiO_2$  doping with metallic ions (1, 2 y 3% mol).

	$Cu^{2+}$	$Ag^{2+}$	$Eu^{3+}$
$TiO_2$ puro.	-		
$TiO_2$ :%M	1% mol a 500°C	1% mol a 500°C	1% mol a 800°C
$TiO_2$ :%M	2% mol a 500°C	2% mol a 500°C	2% mol a 800°C
$TiO_2$ :%M	3% mol a 500°C	3% mol a 500°C	3% mol a 800°C

The thermal treatment temperature was 500°C for the samples of  $TiO_2$  pure,  $TiO_2$ :Cu and  $TiO_2$ :Ag and 800°C for  $TiO_2$ :Eu, due to a very well crystallization of anatase phase.

## 2.1.5 Synthesis procedure of $TiO_2$ : Metal.

### 2.1.5.1 Materials.

The pure  $TiO_2$  and doped were synthesized by the soft chemical method sol-gel using titanium isopropoxide (IV) as a reactant. The reactants used are listed below:

- Titanium (IV) isopropoxide (TTIP) of Strem Chemicals (98%).
- Acetic acid of Fisher Scientific.
- 2-Propanol (99.5%) de Alfa Aesar GmbH.
- Anhydrous copper (II) acetate (98%) of Alfa Aesar GmbH.
- Hydrated europium (III) acetate (99.9%) of Strem Chemicals
- Silver acetate(99%) of Strem Chemicals.

### 2.1.5.2. Synthesis of pure $TiO_2$ .

The synthesis procedure for  $TiO_2$  nanoparticles consists in adding 3.3 ml of TTIP to 8.85 ml of 2-propanol used as solvent. The mixture was kept under vigorous magnetic stirring for 15 min at room temperature. Then, 3.0 ml of acetic acid was added and the stirring performed for 30 min. The obtained product was dried at 120°C for 48 hours and then calcined in air at 500 and 800 °C.

### 2.1.5.3 Synthesis of $TiO_2$ doped with metallic ions powders.

The experimental procedure for the synthesis of metal-doped  $TiO_2$  nanoparticles (with a metal ratio of 1%, 2%, and 3 mol. %) was performed by using TTIP and ethanol as solvent under vigorous magnetic stirring for 15 min. For the doping process, appropriate amounts of copper acetate or silver acetate were added to the solution and stirred until a clear solution was formed, and then the procedure described above was followed. For the Eu-doping, the solution was hermetically closed and ultrasonicated for 2 hours, then heated at 60°C in an oven for 12 hours and ultrasonicated again for 2 hours before adding the acetic acid Then the sols were dried at 120 °C. Cu or Ag-doped  $TiO_2$  were calcined in air at 500 °C with the anatase phase stabilized at this temperature. For Eu doping, the product was calcined at 800 °C due to the stabilization of the anatase phase at a higher temperature compared to doping with the other elements.



## 2.2 Results and discussion: Pure $\text{TiO}_2$ particles.

### 2.2.1 Phase identification by XRD of pure $\text{TiO}_2$ . *Effect of the temperature.*

The powders of  $\text{TiO}_2$  synthesized by the sol-gel method were analyzed by XRD for determination of the crystalline phase. The samples were annealed at different temperatures to determine transition temperature from anatase to rutile phase, see Fig. 13.

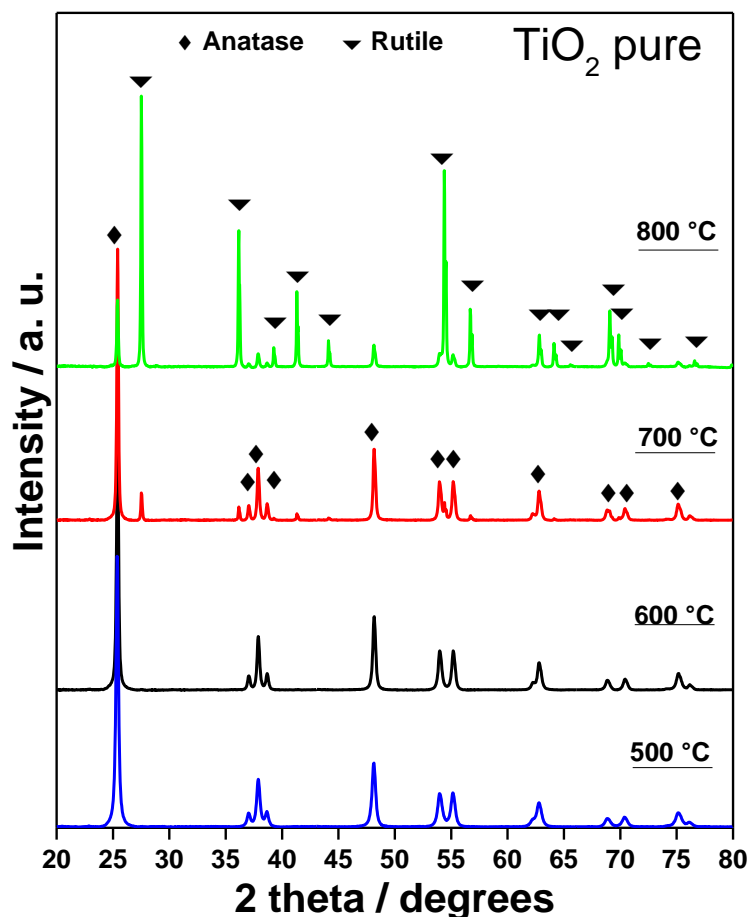


Fig. 13 X-ray diffractogram of  $\text{TiO}_2$  pure at different thermal treatments.

The samples calcined at 500 °C and 600 °C show only the anatase phase, (JPDCS-01-089-4921). The first peak in  $2\theta \approx 27^\circ$  appear from 700 °C, and it is related to the peak in the plane (110) from the rutile phase (JPDCS 01-086-0147). At 800 °C the main peak related is more intense than the main peak of the plane (101) from the anatase. It suggests that at 800 °C the predominant phase is rutile. The temperature of the phase transformation depends on the synthesis conditions for  $\text{TiO}_2$  nanoparticles.

## 2.2.2 Phase identification of $\text{TiO}_2$ powders by Raman spectroscopy.

The anatase and rutile phases of  $\text{TiO}_2$  can be precisely identified from their Raman active modes related to the involved crystalline structure. The anatase phase shows major Raman bands at 144, 197, 399, 515, 519 (superimposed with the  $515\text{ cm}^{-1}$  band), and  $639\text{ cm}^{-1}$ . These bands can be attributed to the six Raman-active modes of anatase phase with the symmetries of  $E_g$ ,  $E_g$ ,  $B_{1g}$ ,  $A_{1g}$ ,  $B_{1g}$ , and  $E_g$ , respectively. The typical Raman bands due to rutile phase appear at 143 (superimposed with the  $144\text{ cm}^{-1}$  band due to anatase phase), and the ones 235, 447, and  $612\text{ cm}^{-1}$ , which can be ascribed to the  $B_{1g}$ , two-phonon scattering,  $E_g$ , and  $A_{1g}$  modes of rutile phase, respectively. Additionally, the band at  $144\text{ cm}^{-1}$  is the strongest one for the anatase phase and the band at  $143\text{ cm}^{-1}$  is the weakest one for the rutile phase [8-11].

The Raman modes of the samples of pure  $\text{TiO}_2$  annealed at  $500^\circ\text{C}$  and  $800^\circ\text{C}$  are shown in the Fig. 14. For the pure  $\text{TiO}_2$  annealed at  $500^\circ\text{C}$  the peaks at 144, 395, 514 and  $636\text{ cm}^{-1}$  corresponds to the anatase phase, while the  $\text{TiO}_2$  annealed at  $800^\circ\text{C}$ , shows peaks corresponding to the anatase and rutile phase. The peaks at 144 and  $515\text{ cm}^{-1}$  correspond to the anatase phase and 235, 447 and  $612\text{ cm}^{-1}$  correspond to the rutile phase. It means that both phases are presents in the sample, these results are in agreement with the X-ray results.

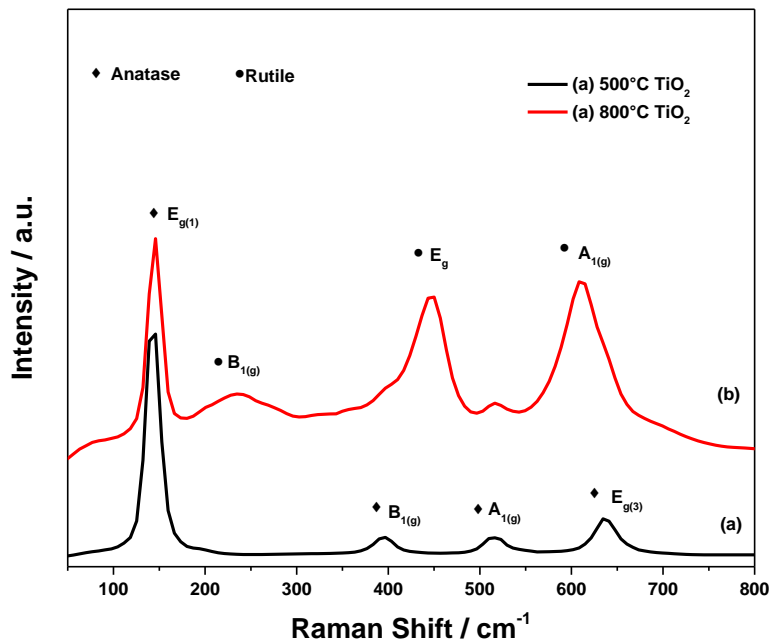


Fig. 14. Raman spectra of pure  $\text{TiO}_2$  heat treated at  $500^\circ\text{C}$  and  $800^\circ\text{C}$ .

### 2.2.3 Optical characterization of pure TiO<sub>2</sub> powders.

The main mechanism of light absorption in pure semiconductors is direct interband electron transitions. This absorption is particularly small in indirect semiconductors, e.g., TiO<sub>2</sub>, where the direct electron transitions between the band centers are prohibited by the crystal symmetry.

Considerable enhancement of the absorption is expected in small TiO<sub>2</sub> nanocrystals, as well as in porous and microcrystalline semiconductors when the interface atoms is sufficiently large [12].

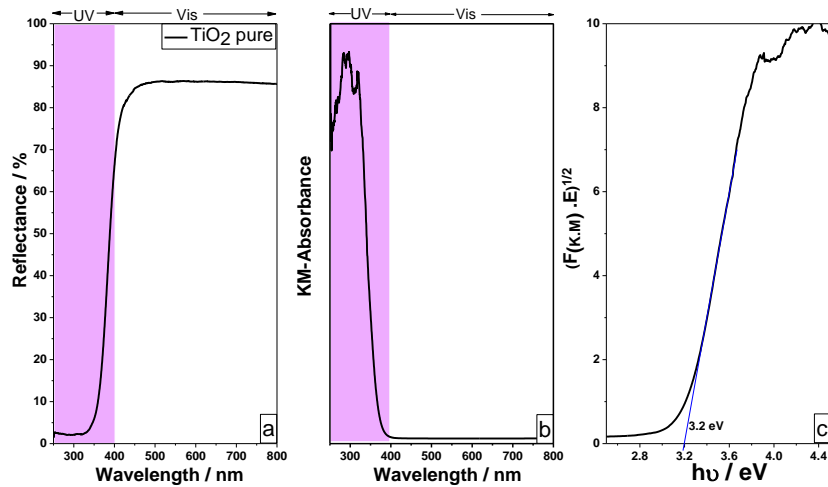


Fig. 15. Optical spectroscopy. a) Diffuse reflectance (%) spectra of pure TiO<sub>2</sub> powders with the corresponding b) Kubelka-Munk absorption curves, c) Determination of band gap.

The diffuse reflectance spectra of pure TiO<sub>2</sub> powders annealed at 500 °C is shown in Fig. 15. They have a strong absorption in the UV region with a low absorption in the visible range. The absorbance spectrum is obtained using the Kubelka Munk function:

$$(R) = \frac{(1 - R)^2}{2R} \quad \text{Equation 10}$$

The band gap was obtained using the Kubelka Munk modified function  $[F(R) \times h\nu]^{1/2}$  vs light absorption energy plot.

A band gap of 3.2 eV was measured for the TiO<sub>2</sub> powder annealed at 500 °C. This value is in accordance with the literature. [13-16].

The absorption in the UV region is associated to the O<sup>2-</sup>(2p)→Ti<sup>4+</sup> (3d) charge transfer process [17]. In TiO<sub>2</sub>, the valence band (VB) is composed of O 2p states, and the conduction band (CB) is composed of Ti 3d states [13].

## 2.2.4 Chemical Analysis by X-ray Photoelectron Spectroscopy of pure $\text{TiO}_2$ powders.

The XPS technique was employed to explore the chemical states of the elements on the surface sample. In this section,  $\text{TiO}_2$  annealed at 500 °C was the only one analyzed. Subsequently, in the next sections it will be compared with the doped systems.

The XPS spectra of O 1s of  $\text{TiO}_2$  in the Fig. 16 a) are attributed to lattice oxygen (530.3 eV), surface hydroxyl oxygen ( $531 \pm 0.5$  eV) and adsorbed oxygen ( $533 \pm 1$  eV) [18, 19]. Two well-resolved peaks at 464.5 and 458.9 eV were observed from the Ti 2p core-level spectrum ( Fig. 16 b), which can be assigned to  $\text{Ti } 2p_{1/2}$  and  $\text{Ti } 2p_{3/2}$  spin-orbital components in  $\text{TiO}_2$ , respectively [20]. XPS results indicate that  $\text{TiO}_2$  has a stoichiometric composition, no impurities that can modify the peaks position were detected.

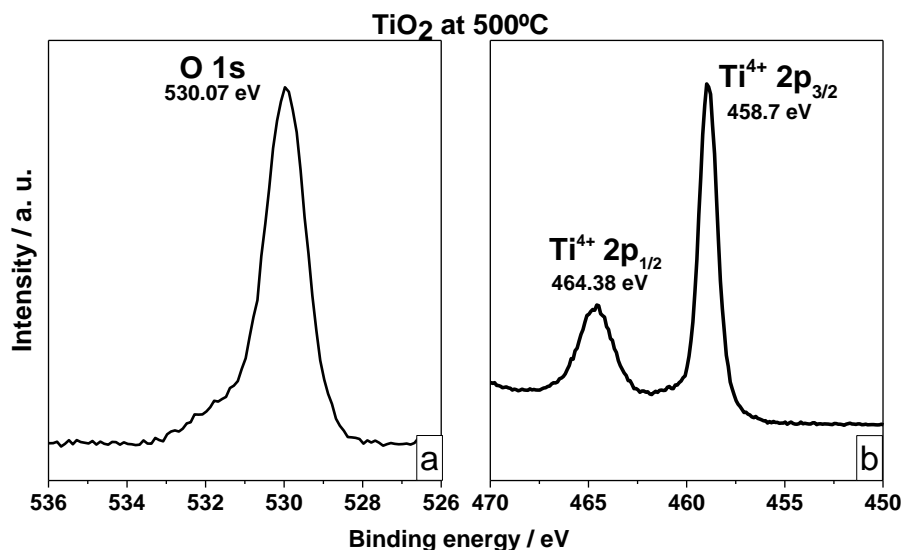


Fig. 16. XPS spectra of pure  $\text{TiO}_2$ .

## 2.2.5 Photocatalytic evaluation of pure $\text{TiO}_2$ powder.

The photodegradation of the dye (methylene blue  $2 \times 10^{-5}$  Mol) by pure  $\text{TiO}_2$  powder annealed at 500 °C when it was irradiated with light from a Xenon lamp was studied. The irradiation power was 120 mW/cm<sup>2</sup> and a distance between the lamp and the sample of 70 cm. A magnetic stirring was used during the test.

The photocatalytic results of the pure  $TiO_2$  annealed at 500 °C were employed as a comparison point, due to the fact that it is a pure sample with a very well anatase phase formation.

During the test, the absorbance of the methylene blue was measured with a VIS spectrometer in intervals of 10 minutes, Fig. 17. These spectra were integrated for the area under a curve measurements.

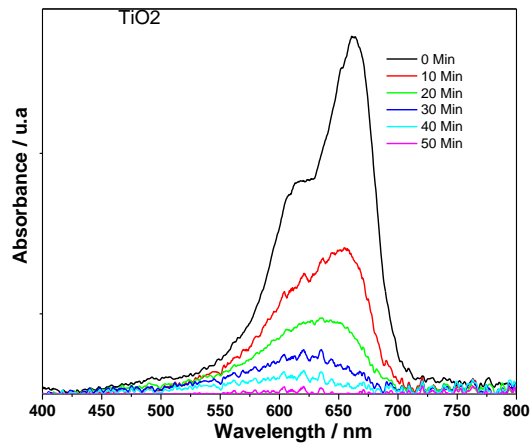


Fig. 17. Absorption spectra of methylene blue photodegradation by pure  $TiO_2$  powder.

The photocatalytic process consists in the concentration reduction ( $C$ ) during a time ( $t$ ), following a first order Kinect employing the next equation:

$$C(t) = C(0) \exp[-kt]$$

Equation 11

The most important parameter of this equation is ( $k$ ), named as constant rate or constant of reaction with units in  $\text{min}^{-1}$ , Fig. 18. The higher the  $k$  constant and the more efficient is the photodegradation of methylene blue. All the photocatalysis experiments were done under the same conditions for a real effective comparison.

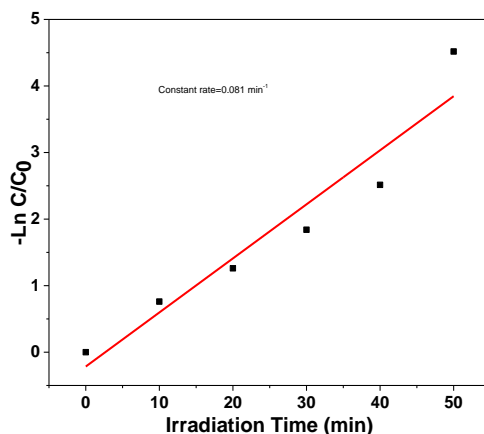


Fig. 18 First order Kinetics of methylene blue photodegradation by pure  $\text{TiO}_2$  powder..

### 2.3 Phase identification by XRD of $\text{TiO}_2$ : Cu powders. *Effect of the temperature.*

$\text{TiO}_2$  powders doped with copper were synthesized by the sol-gel technique and analyzed by X-ray diffraction for the crystalline phase determination. The annealed temperatures were varied to find a stable anatase phase.

For pure  $\text{TiO}_2$  powder annealed at 500 °C, only the anatase phase is present (JPDCS-01-089-4921). From the thermal treatment of 600 °C, a peak at  $2\theta \sim 27^\circ$  corresponding to the main plane (110) (JPDCS 01-086-0147) of the rutile appears. At 700 °C, the sample of 3%Cu- $\text{TiO}_2$  presents a rutile phase predominantly, while for pure  $\text{TiO}_2$  powder at this temperature the predominant phase is anatase. It means that copper addition decreases the phase transformation temperature of the system, see Fig. 19. At 800 °C a complete phase transformation of anatase to rutile is achieved.

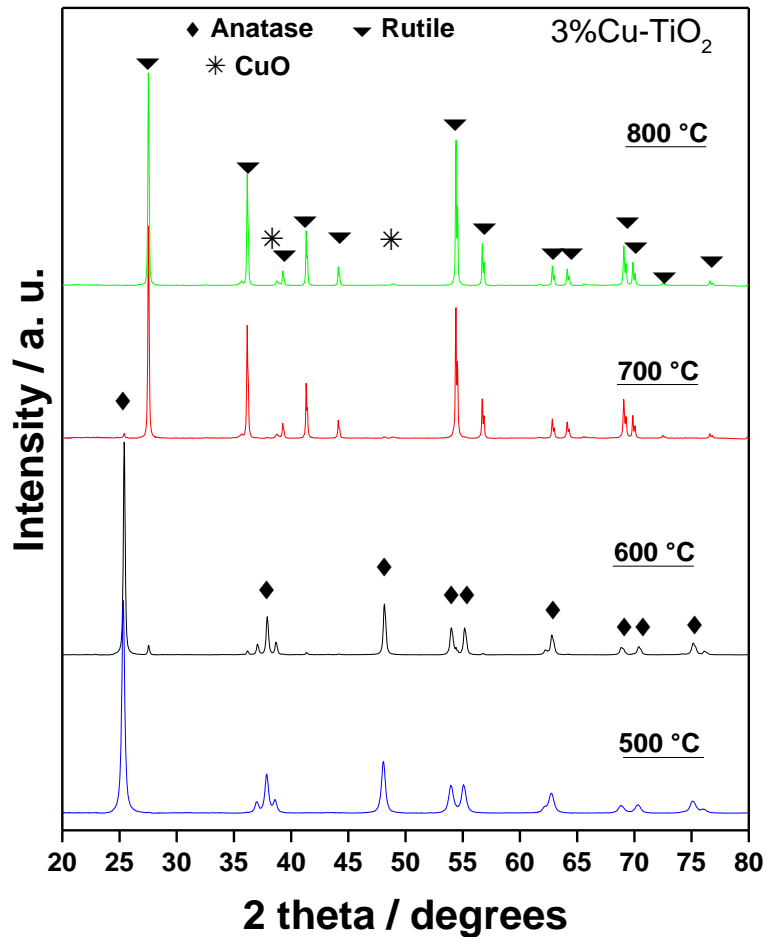


Fig. 19. X-ray diffractograms of 3%Cu- $\text{TiO}_2$  annealed at different temperatures.

When metal ion dopants are used, the properties of  $\text{TiO}_2$  are modified. The modifications are not only dependent on the type of dopant, but also on its concentration and distribution. It has been demonstrated that the transformation rate is dependent on the conditions of doping. Indeed, the way that the dopant is incorporated, and also its oxidation state, chemical environment, and distribution, could have an effect on the phase transformation [21].

Doping of Cu increases the concentration of grain boundary defects. Oxygen vacancies generated by doping migrate to the grain boundary and thereby increase defect content in this region [22]. At elevated temperatures, the substitution of  $\text{Ti}^{4+}$  by  $\text{Cu}^{2+}$  increases the oxygen vacancy concentration and decreases the free electron concentration. The excess of oxygen vacancies created in the  $\text{TiO}_2$  crystal lattice is responsible for anatase to rutile phase transition. Dopants with an oxidation state of 3+ or lower, when placed in the titania lattice points, create a charge-compensating anion vacancy and cause a transformation to the rutile phase [23].

### 2.3.2 Phase identification by XRD of $\text{TiO}_2$ :Cu powders. *Effect of the concentration.*

In this section, the  $\text{TiO}_2$  powders were doped with copper in concentrations of 1%, 2% and 3% mol, by the sol-gel method. X-ray diffraction was employed for phase determination and calculation of crystallite. The samples were annealed at 500 °C to stabilize the anatase phase.

According to the Fig. 20, all the peaks correspond to the anatase phase. It must be noted that the presence of copper oxide cannot be observed even in the sample with the highest copper content. The similarity in ionic radius of  $\text{Cu}^{2+}$  (0.73 Å) to that of  $\text{Ti}^{4+}$  (0.64 Å) enable copper to substitutionally replaces it in the titanium lattice. Cu could be placed in the interstitial sites due to  $r_{\text{Ti}} < r_{\text{Cu}}$  producing the strain of the titania lattice, and hence a displacement of the (1 0 1) signal in the XRD pattern [2, 23].

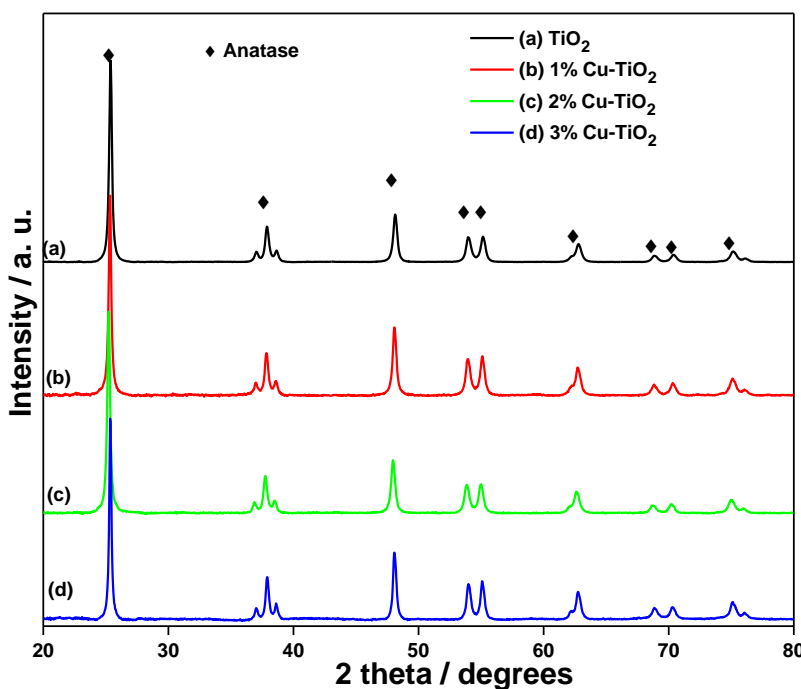


Fig. 20. X-ray diffractogram of  $\text{TiO}_2$  doped with copper (1, 2 and 3% mol) annealed at 500 °C.

The crystallite size was determined using Full Prof software. It can be observed that copper addition of 1% increase the crystallite size, the opposite effect was observed for the doping with



2% mol. It has been noted in a previous report that  $\text{Cu}^{2+}$  doping retards the grain growth of  $\text{TiO}_2$  nanoparticles [23].

Table 3. Crystallite size for  $\text{TiO}_2$  Doped powders with copper (1, 2 and 3% mol).

	$\text{TiO}_2$ pure	1% Cu- $\text{TiO}_2$	2% Cu- $\text{TiO}_2$	3% Cu- $\text{TiO}_2$
<b>Crystallite size</b>	20 nm	29 nm	24 nm	37 nm

The diffractograms of  $\text{TiO}_2$  doped with copper were fitted using High Score Plus software, for determining the peaks position in 2theta corresponding to the main plane of the anatase phase (101), and for the measurement of the FWHM, showed in Table 4. The peak positions of the plane (101) was located at values very similar in 2theta. The FWHM changed due to the doping effect, this variation is related to the evolution of the crystallite size caused by the insertion of  $\text{Cu}^{2+}$ .

Table 4. Diffraction line analysis of the main peak corresponding to the plane (101) from anatase phase, for  $\text{TiO}_2$  doped powders with copper (1, 2 and 3 % mol):

<b>Sample</b>	<b>Peak position of the plane (101) / degrees</b>	<b>Full width at half medium</b>
$\text{TiO}_2$	25.35	0.242
1%Cu- $\text{TiO}_2$	25.31	0.214
2%Cu- $\text{TiO}_2$	25.20	0.247
3%Cu- $\text{TiO}_2$	25.33	0.182

### 2.3.3 Phase identification by Raman spectroscopy of $\text{TiO}_2$ :Cu powders.

Raman spectroscopy was employed for the characterization of the vibrational modes related to the crystalline structure of  $\text{TiO}_2$  powders and to probe the structural changes due to doping.

The ionic size of  $\text{Cu}^{2+}$  (0.73 Å) is larger than that of  $\text{Ti}^{4+}$  (0.64 Å), and hence, doping of this ion will distort the lattice structure of  $\text{TiO}_2$ . As there is charge difference between  $\text{Cu}^{2+}$  and  $\text{Ti}^{4+}$ , doping of Cu generates oxygen vacancies in the lattice of  $\text{TiO}_2$  to maintain the charge neutrality. If doping occurs on the substitutional position of the  $\text{Ti}^{4+}$  site, the Ti-O-Ti bond will be distorted and a new Cu-O-Ti or Cu-O-Cu bond will be formed. Therefore, disturbance of the Ti-O-Ti bonds and the formation of new Cu-O bonds will affect the Raman-active modes and will result in the broadening and shifting of the Raman bands [13].

No Raman modes from copper oxide were detected by this technique. The observed ones related to anatase were located at 43, 396, 516 and 641  $\text{cm}^{-1}$ , see Fig. 21.

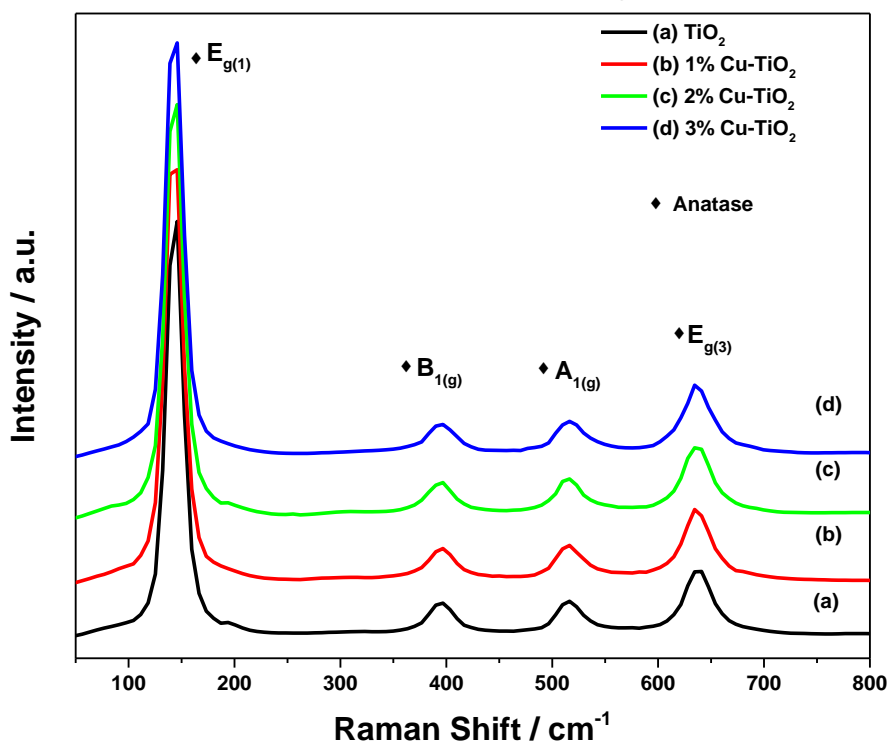


Fig. 21. Raman spectra of  $\text{TiO}_2$  doped with copper (1, 2 and 3% mol) annealed at 500°C.

An adjustment of the Raman line was realized for the main vibration mode  $E_{g1}$ , using the Voigt function for changes in the Raman shift and the FWHM caused by the doping effect, see Table 5.

The  $E_g$  peak is associated with the symmetric stretching vibration of O-Ti-O in  $\text{TiO}_2$  [10, 13]. No particular shift of the Raman band position was detected while a net broadening of the FWHM was observed for the doping samples. Parker and Siegel [24], reported that this broadening of the Raman peaks is due to the presence of oxygen vacancies. The formation of oxygen vacancies near of the Cu is theoretically possible in  $\text{TiO}_2$  doped with copper [25].

Table 5. Analysis of the main Raman peak of the anatase  $E_{g1}$  of  $\text{TiO}_2$ :Cu.

Samples	$E_{g1}$ peak position / $\text{cm}^{-1}$	Full width at half medium.
$\text{TiO}_2$	142.9	18.4
1%Cu- $\text{TiO}_2$	142.7	19.3
2%Cu- $\text{TiO}_2$	143.1	19.02
3%Cu- $\text{TiO}_2$	143.1	19.02

### 2.3.4 BET surface area measurements of $\text{TiO}_2$ :Cu powders.

The BET surface area, pore volume and pore size of the pure  $\text{TiO}_2$  pure and the  $\text{TiO}_2$  doped powders with copper are shown in Table 6. The doped sample has a lower surface area than the pure  $\text{TiO}_2$  powder. This behavior could be due to the agglomeration process or ripening caused by the presence of oxygen vacancies [26-28]. The particle size was determined by the BET surface area results.

Table 6. BET surface area, pore volume and pore size of  $\text{TiO}_2$ :Cu.

Sample	BET surface area / $\text{m}^2 \text{g}^{-1}$	Pore volume / $\text{cm}^3 \text{g}^{-1}$	Poro size / nm	Average particle diameter / nm
$\text{TiO}_2$ at $500^\circ\text{C}$	31.3	0.078	9	49
3 % Cu- $\text{TiO}_2$ at $500^\circ\text{C}$	22.6	0.056	10	68

### 2.3.5 EPR evaluation of $TiO_2:Cu$ powders.

Electron paramagnetic resonance (EPR) is an important tool to determine the valence states of doping elements and their local environments in the host matrices. As the  $TiO_2$  is a photoactive materials able to react with radiations in suitable spectral range, the experiments were conducted at room temperature (RT) and at low temperature 150 K as well as in-situ under irradiation by using the light spectrum of Xe source with a nominal power of 10 W on the sample.

A measurement under Xe lamp radiation contributes to the creation of an additional small signal superimposed to the EPR spectrum of  $Cu^{2+}$ . To identify the main features of the EPR signal, a simulation was realized taking into account the electronic spin of  $Cu^{2+}$  ( $S=1/2$ ) and the nuclear spin of the two main isotopes of Cu nuclei ( $I=3/2$ ).

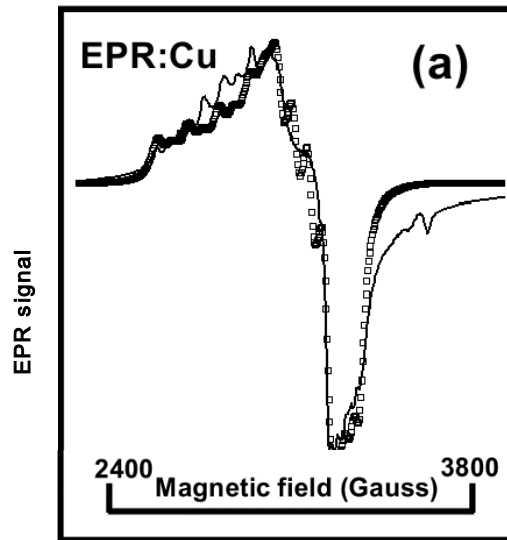


Fig. 22. EPR spectrum of  $Cu^{2+}$  ions in  $TiO_2$  with the experimental (continuous) and the simulated one (dashed).

The involved interactions between electronic spin and the applied magnetic field as well as with the nuclear spin are summarized in the following spin Hamiltonian:

$$\hat{H} = \beta \vec{B} \tilde{g} \vec{S} + \vec{I} \tilde{A} \vec{S} \quad \text{Equation 12}$$

Where B stands for the applied magnetic field, the Landé tensor depending on the electronic structure of the  $Cu^{2+}$  ion in its local environment, the hyperfine coupling tensor between electronic spin (S) and nuclear one (I).

The simulation of the experimental spectrum yields the theoretical values of the EPR spectral parameters summarized in Table 7. The theoretical spectrum is compared to the experimental one (Fig. 22) based on the use of two crystalline sites for  $\text{Cu}^{2+}$  ions. The only difference between spectral parameters lies in the variation in one component of g-tensor ( $\Delta g_z=0.04$ ). The existence of two crystalline host sites for  $\text{Cu}^{2+}$  seems involved in  $\text{Cu-TiO}_2$  with rhombic symmetry which may occur from the substitution of  $\text{Cu}^{2+}$  in  $\text{Ti}^{4+}$  ions. The distortion of the local sites is expected due to the difference between the ionic radii of Ti (4+): 0.51-0.6 and Cu (2+): 0.65-0.73. The g-tensor components are in the same order of magnitude as those obtained in Cu-doped  $\text{BiVO}_4$ . [29].

Thus, distorted oxygen environments constitute the local hosting sites for  $\text{Cu}^{2+}$  ions. The doping process consists in the incorporation of  $\text{Cu}^{2+}$  ions in the host crystalline sites of  $\text{TiO}_2$ . It is worth noting that there is no occurrence in the host matrix of Cu-rich phase segregation or Cu clusters.

The small EPR signal located in the high magnetic field side correspond to g- factor about 1.96. This value is well identified for  $\text{Ti}^{3+}$  ions which occur after irradiation of the sample by Xe-lamp which also contain a spectral band in the UV range.

Table 7. EPR values obtained of EPR experimental data of 3%Cu- $\text{TiO}_2$  powders.

Metal doping	gx	gy	gz	Ax (G)	Ay (G)	Az (G)	LW (G)	%
$\text{Cu}^{2+}$ (1)	2.06 (2)	2.15 (2)	2.36 (2)	30 (3)	50 (5)	100 (5)	25	38
$\text{Cu}^{2+}$ (2)	2.06 (2)	2.15 (2)	2.40 (2)	30 (3)	50 (5)	100 (5)	25	62

The gx, gy, gz are the components of g-tensor, Ax, Ay and Az the hyperfine components of A-tensor and LW the line width of EPR lines.

### 2.3.6 Optical characterization of $\text{TiO}_2\text{:Cu}$ powders.

The main goal of doping with metallic ions is to increase the light absorption in the visible region. The nature of  $\text{TiO}_2$  allows the absorption in the UV region. However, UV light represents only 10 % of the solar light. With UV-Vis spectroscopy, it is possible to appreciate the optical behavior of the doping systems.

The absorption in the UV region is associated to the  $\text{O}^{2-}(2p) \rightarrow \text{Ti}^{4+}(3d)$  charge transfer process. The absorption in the visible range increases for the sample doped with copper due to the combination of the charge transfer processes  $\text{O}^{2-}(2p) \rightarrow \text{Ti}^{4+}(3d)$  and  $\text{O}^{2-}(2p) \rightarrow \text{Cu}^{2+}(3d)$ . The absorption band at 600-1000 nm can be attributed to copper transitions  ${}^2E_g \rightarrow {}^2T_{2g}$  for copper ions localized in the symmetry of the distorted octahedron. [30], see Fig. 24. Indeed  $\text{Cu}^{2+}$  has a  $d^9$  electronic configuration, and in the pure octahedral coordination, the  ${}^2D$  state of  $\text{Cu}^{2+}$  is split into  ${}^2E_g$  ground state and  ${}^2T_{2g}$  excited state with a single electronic transition.

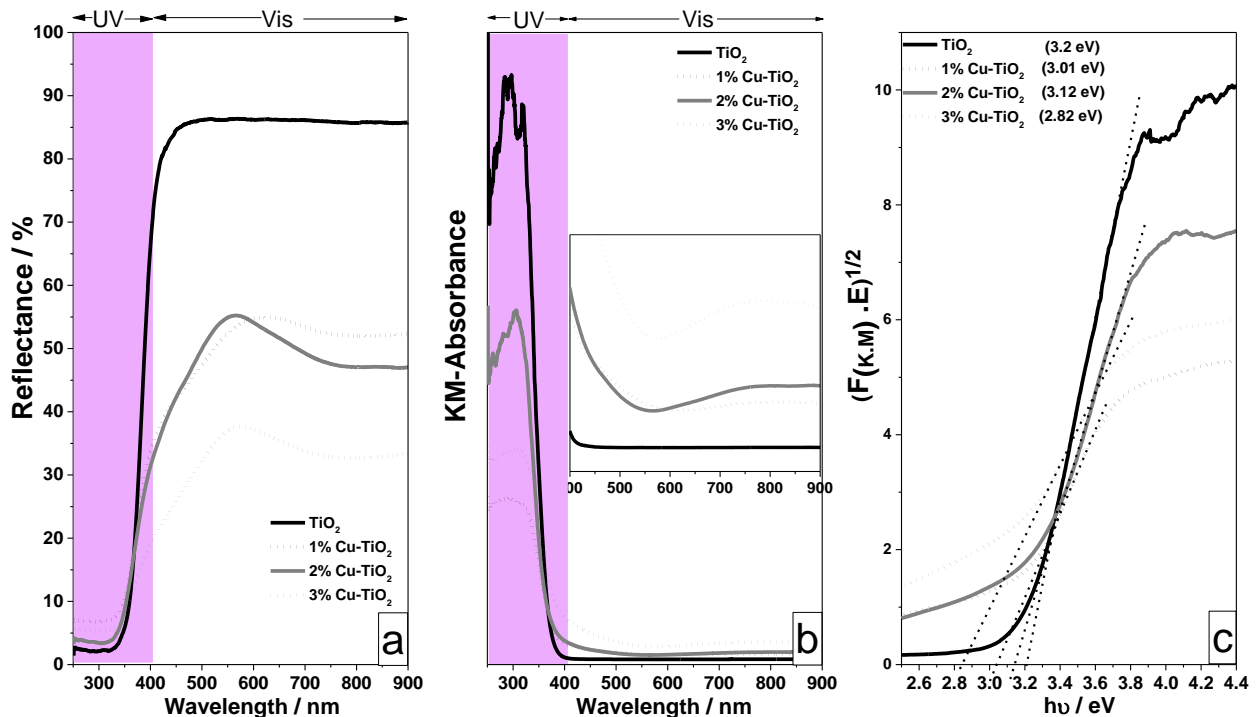


Fig. 23. Optical spectroscopy. a) Diffuse reflectance (%) spectra of  $\text{TiO}_2$  doped powders with copper (1, 2 and 3% mol) with the corresponding b) Kubelka-Munk absorption curves, c) Determination of band gap.

However, from the XRD and Raman spectra of the samples, it was found that doping of  $Cu^{2+}$  generates oxygen vacancies which lie near  $Cu^{2+}$ . Therefore,  $Cu^{2+}$  is no longer in the pure octahedral ( $O_h$ ) symmetry, and the symmetry is slightly distorted. A Jahn-Teller (J-T) distortion is taking place, changing the symmetry from  $O_h$  to  $D_{4h}$ . Due to the J-T effect, the ground state  ${}^2E_g$  is further splitted into  ${}^2B_{1g}$  ground and  ${}^2A_g$  excited states, and the  ${}^2T_{2g}$  is separated into  ${}^2B_{2g}$  ground and  ${}^2E_g$  excited states. Therefore, the possible optical transitions that may give rise to the above peaks are  ${}^2B_{1g} \rightarrow {}^2A_g$ ,  ${}^2B_{1g} \rightarrow {}^2B_{2g}$ , and  $B \rightarrow E_g$ . The Fig. 24 shows the octahedral distortion to tetragonal local symmetry. [13].

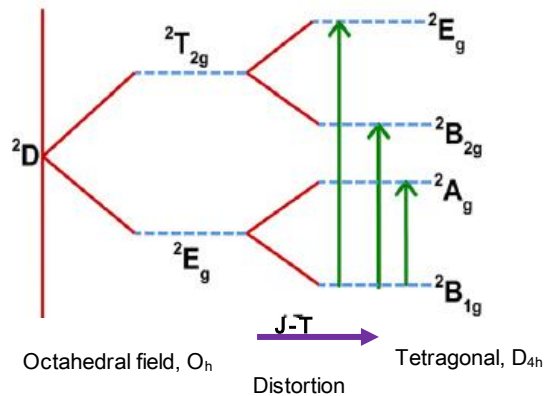


Fig. 24. Jahn-Teller(J-T) distortion of the octahedral symmetry of  $TiO_6$  and changes in the d-d transition from octahedral to tetragonal phase. In undistorted octahedral coordination, only a single electronic transition occurs

The band gap of the doping samples decrease in comparison with the pure  $TiO_2$  as it can be observed in Fig. 23 c).  $Cu^{2+}$  forms sub-band states in the band gap of  $TiO_2$ . Along with  $Cu^{2+}$ , oxygen defect band states are also formed in the band gap. In pure  $TiO_2$ , the electronic transition occurs directly from VB to CB. However, on Cu doping, the electrons are not directly excited to CB since the unoccupied  $Cu^{2+}$  s-d states and oxygen vacancies capture the electrons. The charged oxygen defect states formed in  $TiO_2$  are F (two electrons),  $F^+$  (single electron), and  $F^{++}$  (devoid electrons). The oxygen vacancy states that may capture electrons are  $F^+$  and  $F^{++}$ , respectively. Therefore, the sub-band states of  $Cu^{2+}$  and oxygen defects are responsible for the reduction of the effective band gap of  $TiO_2$  nanoparticles [13].

### 2.3.7 Chemical Analysis by XPS of $\text{TiO}_2$ :Cu powders.

XPS spectroscopy was employed for the determination of the chemical state of Cu and Ti in the annealed samples. Fig. 25 shows the XPS spectrum of 3%Cu- $\text{TiO}_2$  powder and it is compared with the pure  $\text{TiO}_2$ . In Fig. 25 a) can be observed the peaks at 933.06 eV and 942.28 eV corresponding to the  $\text{Cu}^{2+}$  oxidation state, the first correspond to the  $\text{Cu } 2p_{3/2}$  transition and the second correspond to the satellite peak. The peak transition is lower than the values reported in the literature (933.6 eV). The shift of binding energies to the lower energy side indicates the substitutional incorporation of Cu ions in the  $\text{TiO}_2$  lattice rather than the formation of  $\text{Cu}_2\text{O}$  or  $\text{CuO}$  at the surface of  $\text{TiO}_2$  [17, 19, 31, 32].

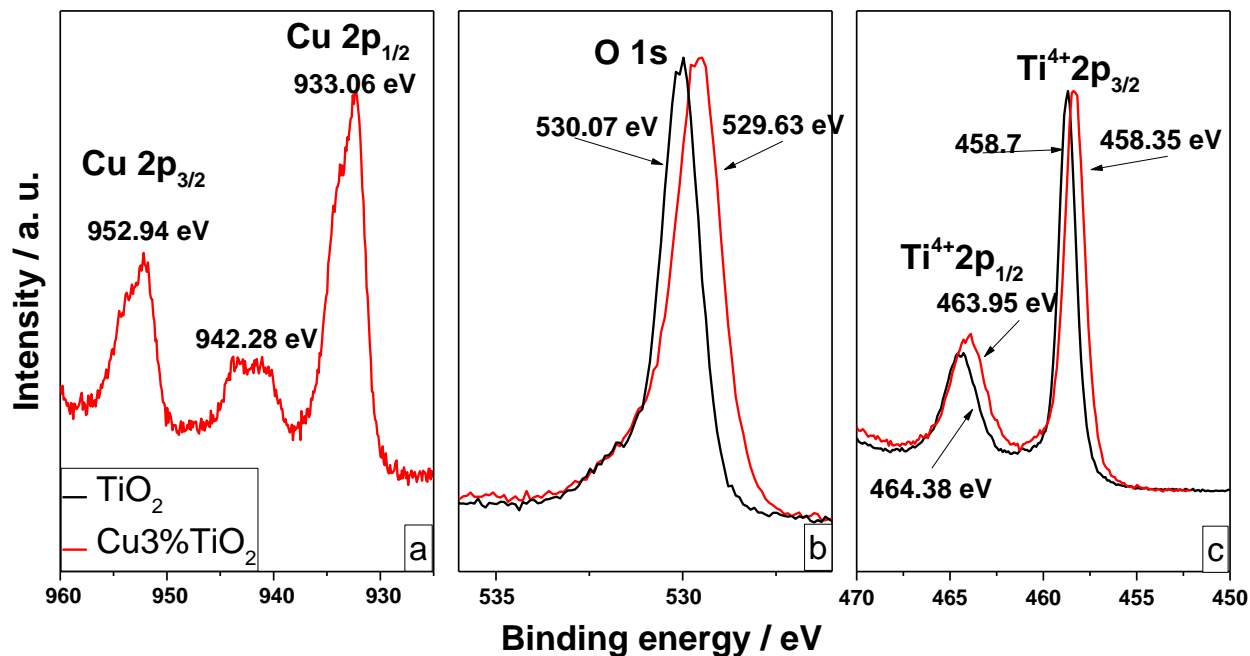


Fig. 25. XPS spectra of 3%Cu- $\text{TiO}_2$  annealed at 500°C.

The XPS spectrum of O 1s for the 3%Cu- $\text{TiO}_2$  powder can be observed in the Fig. 25 b) the loss of oxygen atoms of the lattice is caused by the difference of the valence of  $\text{Ti}^{4+}$  and  $\text{Cu}^{2+}$ . This weakens the Ti-O-Ti bonds, which can be the reason for lowering of O 1s binding energies in comparison with the O 1s of pure  $\text{TiO}_2$  powder.

The XPS spectrum of  $\text{Ti}^{4+}$  for the 3%Cu- $\text{TiO}_2$  can be observed in the Fig. 25 c) and shows a lower binding energy in comparison with the pure  $\text{TiO}_2$ . A decrease of Ti  $2p_{3/2}$  binding energy is a direct



measure of the lowering of valence state level of  $Ti^{4+}$ . Formation of oxygen vacancies, as a result of doping, results in an electron density decrease and a partial reduction of  $Ti^{4+}$  to  $Ti^{3+}$  and to  $Ti^{2+}$ , which reflects a decrease in  $Ti\ 2p_{3/2}$  binding energy.[33, 34]. This was clearly shown by EPR method with the existence of  $Ti^{3+}$  EPR spectrum in Cu doped  $TiO_2$ . In Table 8 is summarized the peaks positions of the XPS spectra previously discussed.

Table 8. XPS binding energies of 3%Cu- $TiO_2$  powder.

	Binding energy / eV			
	Ti2p <sub>3/2</sub>	Ti2p <sub>1/2</sub>	O1s	Cu2p <sub>3/2</sub>
Pure $TiO_2$	458.7	464.38	530.07	-
3%Cu- $TiO_2$	458.35	463.95	529.63	933.06

### 2.3.8 Photocatalytic evaluation of $\text{TiO}_2$ : Cu powders.

The photodegradation of the dye (methylene blue  $2 \times 10^{-5}$  Mol) by pure or doped  $\text{TiO}_2$  powders annealed at  $500^\circ\text{C}$  when were irradiated with light from a Xenon lamp was studied. The irradiation power was from  $120 \text{ mW/cm}^2$  and a distance of 70 cm between the lamp and the sample. A magnetic stirring was used during the test.

During the test, the absorbance of the methylene blue was measured with a VIS spectrometer in intervals of 10 minutes. The Fig. 26 shows the methylene blue spectra for the samples of  $\text{TiO}_2$  doped with copper (1, 2 and 3 %mol). These spectra were integrated for the area under a curve measurements.

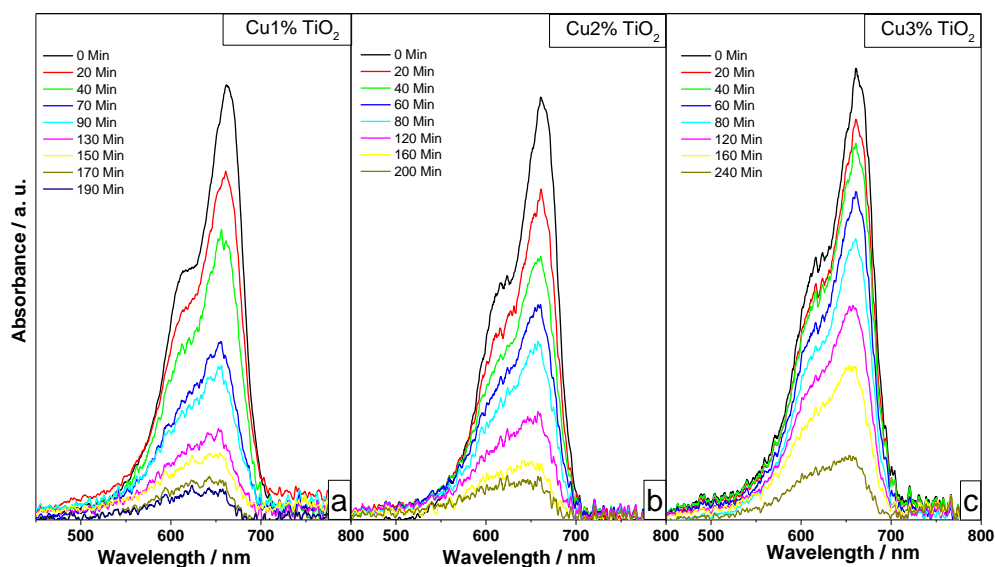


Fig. 26. Absorption spectra of methylene blue photodegradation by  $\text{TiO}_2$  doped with copper (1, 2 and 3% mol).

The first order kinetics of methylene blue photodegradation by  $\text{TiO}_2$  doped with copper (1, 2 and 3% mol) are shown in Fig. 27. The doping samples present a lower constant rate in comparison with pure  $\text{TiO}_2$  powder. It means that Cu doping do not improve the photocatalytic efficiency..

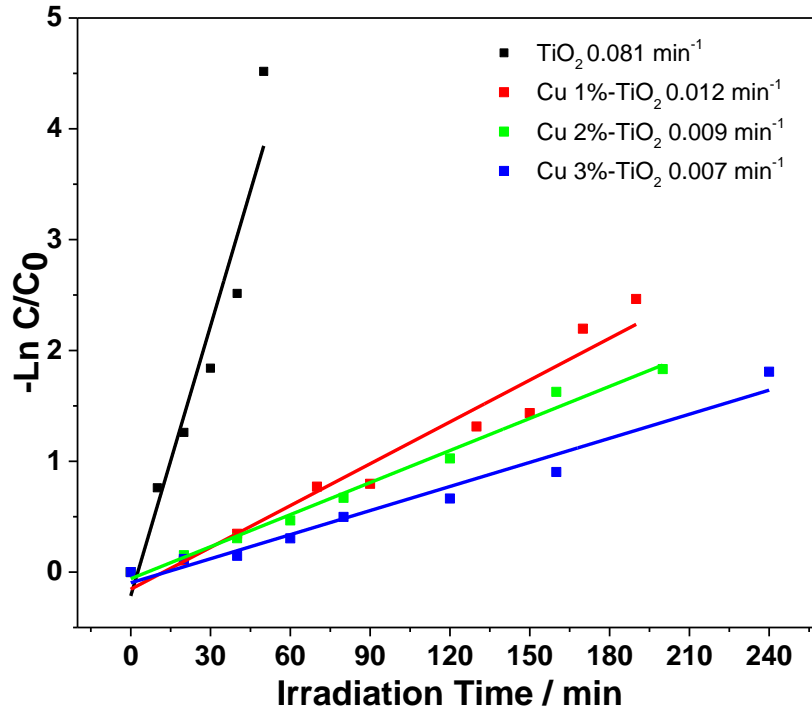


Fig. 27. First order Kinetics of methylene blue photodegradation by TiO<sub>2</sub> doped with copper (1, 2 and 3% mol).

When Cu<sup>2+</sup> replaces Ti<sup>4+</sup> in the crystalline structure it can act as recombination centers for the electrons and holes photoinduced through the following process:



Where the energy level for M<sup>n+</sup>/M<sup>(n-1)+</sup> lies below the conduction band edge (E<sub>cb</sub>) and the energy level for M<sup>n+</sup>/M<sup>(n+1)+</sup> above the valance band edge (E<sub>vb</sub>) [19, 35, 36].

### 2.4.1 Phase identification by XRD of $TiO_2:Ag$ Powders. *Effect of the temperature.*

$TiO_2$  powders doped with silver were synthesized by the sol-gel technique and analyzed by X-ray diffraction for the crystalline phase determination. The annealed temperatures were varied to find a stable anatase phase.

Fig. 28 shows the diffractograms of the 3%  $Ag-TiO_2$  powder with different annealing temperatures. It can be observed that at 500°C and 600°C only exist the anatase phase. At 700°C a very well formed rutile phase is present; while for pure  $TiO_2$  powder at this temperature the predominant phase is anatase. This means that silver addition decreases the phase transformation temperature of the system.

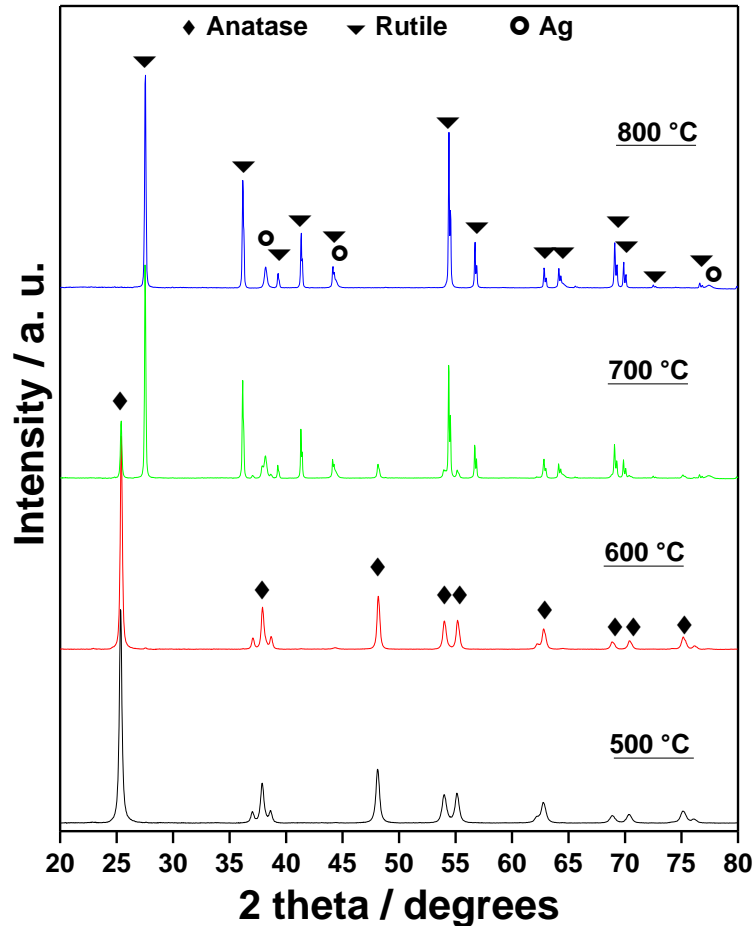


Fig. 28. X-ray diffractograms of 3%  $Ag-TiO_2$  annealed at different temperatures.

It is well accepted that the concentration of oxygen vacancies strongly influences the rate of the anatase to rutile transformation. Because the radius of  $\text{Ag}^+$  ion (ca. 126 pm) is much larger than that of  $\text{Ti}^{4+}$  ion (ca. 68 pm), the  $\text{Ag}^+$  ions introduced by the sol-gel process could not enter into the lattice of anatase phase to form a stable solid solution. During the drying and calcination process with the elimination of liquids and organic substances and the crystallization of anatase phase, the uniformly dispersed  $\text{Ag}^+$  ions would gradually migrate from the volume of anatase grains to the surface of the  $\text{TiO}_2$  powder under the action of heat. The density of surface defects at the surface of anatase grains then increases, which favors the rutile nucleation.

On the other hand, due to the high redox potential for the  $\text{Ag}^+$  ion, by heat and  $\text{TiO}_2$  photocatalytic reduction, the  $\text{Ag}^+$  ions spreaded on the surface anatase grains would gradually be reduced into  $\text{Ag}^0$ .

For charge compensation, oxygen vacancies occur:



The concentration of oxygen vacancies at the surface of the  $\text{TiO}_2$  powder then increases, which facilitates the bond rupture and ionic movement necessary for the formation of the rutile phase. The anatase to rutile phase transformation is then accelerated [37].

### 2.4.2 Phase identification by XRD of $\text{TiO}_2$ :Ag powders. *Effect of the concentration.*

In this section,  $\text{TiO}_2$  was doped with silver in concentrations of 1%, 2% and 3% mol, by the sol-gel method. X-ray diffraction was employed for phase determination and estimation of crystallite size. The samples were annealed at 500 °C.

Fig. 29 shows the diffractograms of the  $\text{TiO}_2$  doped powders with silver (1, 2 and 3% mol). XRD patterns do not show any noticeable change in the number of diffraction lines due to the presence of the silver dopant. This suggests that the Ag nanoparticles were well scattered located on the surface of  $\text{TiO}_2$  grains. Due to the higher ionic radii of Ag (1.26 Å), is complicated to incorporate into the lattice structure [38].

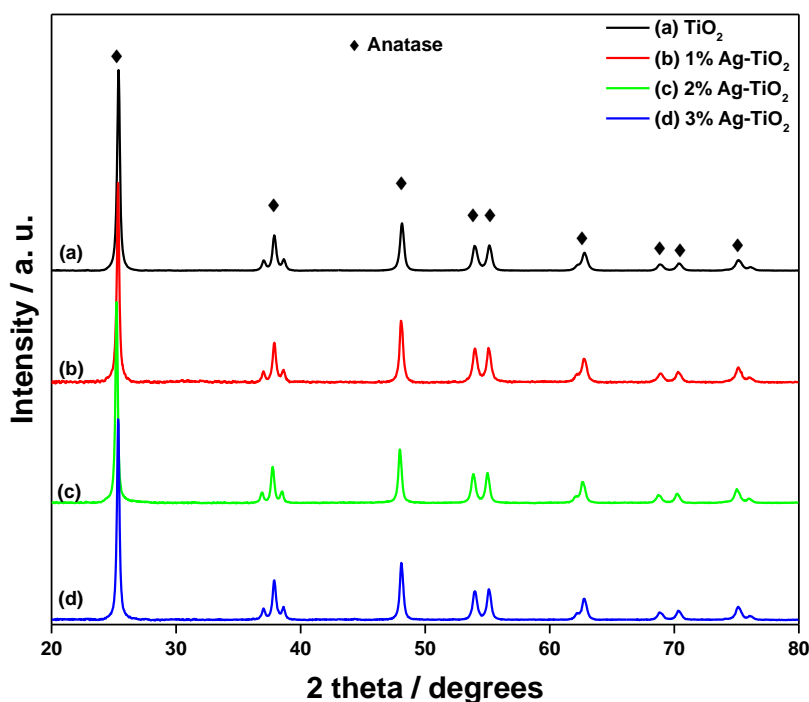


Fig. 29. X-ray diffractogram of  $\text{TiO}_2$  doped with silver (1, 2 and 3% mol) annealed at 500°C.

The diffractograms of  $\text{TiO}_2$  doped with silver were refined using High Score Plus software, to determine the involved crystalline structure by the main plane of the anatase phase (101), and for the measurement of the FWHM, reported in Table 9. The peaks position of the plane (101) was located at values very similar in  $2\theta$ . The FWHM changed due to the doping effect, this variation is related to the crystallite size being modified by the incorporation of Ag in the host titania.

Table 9. Position and FWHM of the (101) diffraction line as function of the Ag doping ratio:

Sample	Peak position of the plane (101) / degrees	Full width at half medium .
$\text{TiO}_2$	25.35	0.24
1%Ag- $\text{TiO}_2$	25.31	0.20
2%Ag- $\text{TiO}_2$	25.20	0.20
3%Ag- $\text{TiO}_2$	25.32	0.21

The presence of structural defects generate a charge decompensation favoring the agglomeration process and therefore the slight increased of particle size, see Table 10. Despite the crystallite size increased by the doping effect, the sample doped with 3% mol has a similar crystallite size than the doped with 1%. It could be due to the silver incorporated on the  $\text{TiO}_2$  surface that favor the growth of titania nanoparticle. However, the slight increase of the Ag- $\text{TiO}_2$  crystallites is contradictory to several reports where doping the structure induce a reduction of the size of particle. Additional BET measurements as discussed below can shed light also on the particle growth due to doping.

Table 10. Crystallite size for  $\text{TiO}_2$ . Doped powders with silver (1, 2 and 3% mol).

	$\text{TiO}_2$ pure	1% Ag- $\text{TiO}_2$	2% Ag- $\text{TiO}_2$	3% Ag- $\text{TiO}_2$
<b>Crystallite size</b>	20 nm	30 nm	26 nm	32 nm

### 2.4.3 Phase identification by Raman spectroscopy of $\text{TiO}_2$ :Ag powders.

Raman bands related to oxides of silver were not detected by this technique. The Raman modes of the anatase were shown at 43, 396, 516 y 641  $\text{cm}^{-1}$ , see Fig. 30. For  $\text{TiO}_2$  doped with silver we may notice additional band at 80  $\text{cm}^{-1}$  which correspond to metallic Ag, [39, 40].

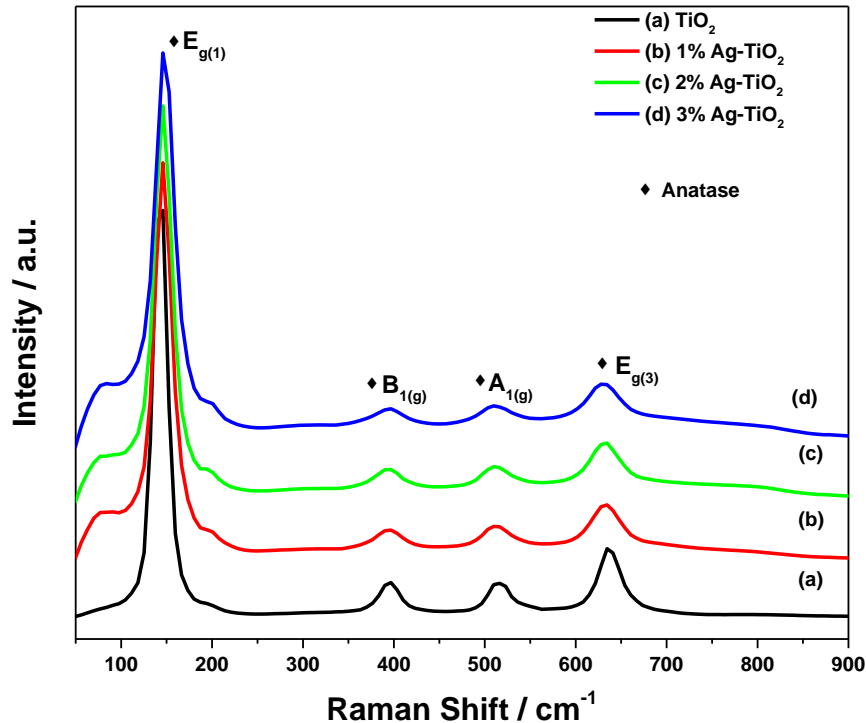


Fig. 30. Raman spectra of  $\text{TiO}_2$  doped with silver (1, 2 and 3% mol) annealed at  $500^\circ\text{C}$ .

A nonlinear fitting of the Raman spectra was realized for the main vibration mode  $E_{g1}$ , using the Voigt function for changes in the Raman shift and the FWHM caused by the doping effect, see Table 5. A shift and broadening of the main Raman mode of anatase  $E_{g1}$  can be observed for the  $\text{TiO}_2$  doped powders with silver. Quiñones et al [39], attributed this effect to a volume contraction and radial pressure increase, which consequently changes the force constant and vibrational amplitude of the nearest neighbor bond. The  $E_g$  peak is associated with the symmetric stretching vibration of O-Ti-O in  $\text{TiO}_2$  [10, 13].



The intensity of the bands relevant to  $\text{TiO}_2$  decreases with increasing Ag amount (prolonging reaction time), which implies that there is an interaction between Ag and  $\text{TiO}_2$  probably due to some plasmon effect which can alter the Raman bands. [41].

Table 11. Analysis of the main Raman band associated to  $E_{g1}$  Raman active mode of anatase of  $\text{TiO}_2$ :Ag powders.

Samples	$E_{g1}$ peak position / $\text{cm}^{-1}$	Full width at half medium.
$\text{TiO}_2$	142.9	18.4
1%Ag- $\text{TiO}_2$	145.9	20.6
2%Ag- $\text{TiO}_2$	145.9	22.8
3%Ag- $\text{TiO}_2$	147.5	24.6

### 2.3.4 BET surface area measurements of $\text{TiO}_2$ :Ag powders.

BET surface area measurements are shown in Table 12 and lower for the sample doped with  $\text{TiO}_2$ . The decrease in surface area of Ag-loaded  $\text{TiO}_2$  powders might be due to a block of fine capillaries of parent  $\text{TiO}_2$  surface by metal film islands [16]. The diameter particle size was determinate using the BET surface area.

Table 12. BET surface area, pore volume and pore size of  $\text{TiO}_2$ :Ag powders.

Sample	BET surface area / $\text{m}^2 \text{g}^{-1}$	Pore volume / $\text{cm}^3 \text{g}^{-1}$	Pore size / nm	Average particle diameter / nm
$\text{TiO}_2$ at $500^\circ\text{C}$	31.3	0.078	9.9	49
3%Ag- $\text{TiO}_2$ at $500^\circ\text{C}$	21.4	0.073	13.7	71

### 2.4.5 EPR investigations of $TiO_2:Ag$ powders.

As  $Cu^{2+}$ ,  $Ag^{2+}$  ions possess an electronic configuration with  $d^9$  orbitals and then the paramagnetic behavior is expected with an effective spin ( $S=1/2$ ). The EPR spectrum of 3 at.% of Ag-doped  $TiO_2$  powders is shown in Fig. 31, along with an additional narrow line which emanates from color centers in  $TiO_2$ . The simulation of the EPR spectrum is performed based on the above spin hamiltonian with electronic spin  $S=1/2$  and nuclear spin  $I=1/2$  for Ag nuclei. The spectral parameters of  $Ag^{2+}$  doped  $TiO_2$  are summarized in table 1. Only one crystalline site is occupied by  $Ag^{2+}$  in contrast to  $Cu^{2+}$  discussed above with two involved substitutional sites. The low quality of the EPR signal/noise ratio indicates a lower concentration of substitutional  $Ag^{2+}$  with regard to the departure of its ionic radius (0.94) compared to titanium ion. The anisotropy of the g-tensor which shows a rhombic local symmetry around  $Ag^{2+}$  ions is inferred in a similar way as shown above for  $Cu^{2+}$  doping.

Table 13. EPR values obtained of EPR experimental data of 3%Ag- $TiO_2$  powders.

Metallic doping	gx	gy	gz	Ax (G)	Ay (G)	Az (G)	LW (G)	%
$Ag^{2+}$	2	2.05	2.21	20	20	30	10-20 G	100
Colour centers ( $Ag-TiO_2$ )	2.0035	2.0035	2.0035	0	0	0	3	100

Thus, an only low fraction of substitutional silver seems realized in the sample with incorporation in crystalline sites leading to the well resolved hyperfine structure as illustrated by the doublet in Fig. 31. Under irradiation by wide spectral range from Xe-lamp, we notice the development of narrow EPR line which originates from color centers induced by UV radiation in  $TiO_2$ . However, in contrast to  $Cu^{2+}$  doping case, there is no evidence of valence change of Titanium ions leading to  $Ti^{3+}$ . It seems that, in the present case of doping, the color centers are formed preferentially to the formation of  $Ti^{3+}$  as observed for copper doping.

It is worth noting that Ag doping ratio didn't induce important EPR spectra. Even with the highest used ratio of 3 at.%, a low signal on noise ratio remains on the recorded EPR spectrum. This behavior suggests the possibility of Ag rich phases segregated from the host  $\text{TiO}_2$  structure. Alternatively, if the valance state is  $\text{Ag}^+$ , no EPR signal may be induced in that case. Optical absorption measurements are then helpful to point out the eventual involvement of Ag metal clusters as discussed below.

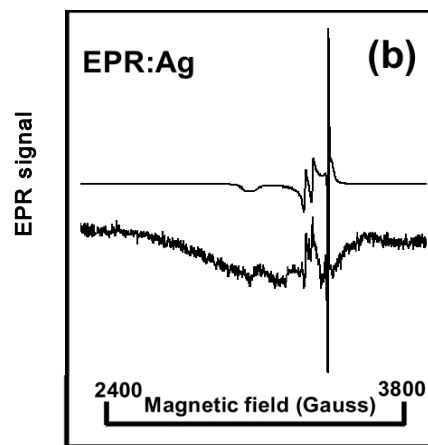


Fig. 31. EPR spectra of 3 at.% Ag doped  $\text{TiO}_2$  powder with the experimental (thick line) and simulation (thin line).

### 2.4.6 Optical characterization of $\text{TiO}_2$ :Ag powder.

The main goal of doping with metallic ions consists in an increase of the light absorption in the visible region. UV-Vis spectroscopy is appropriate possible to measure the optical behavior of the doping systems.

The absorption in the UV region is associated to the  $\text{O}^{2-}(2p) \rightarrow \text{Ti}^{4+}(3d)$  charge transfer process [17]. A strong absorption is observed at 600 nm for the  $\text{TiO}_2$  doped with silver Fig. 32.

This significant change is strongly attributed to localized surface plasmon resonance (LSPRs) induced by Ag NPs. The presence of Ag NPs on the titania surface had induce charge oscillations of the metallic particles enhancing then the electromagnetic (light) fields in the vicinity of titania [3].

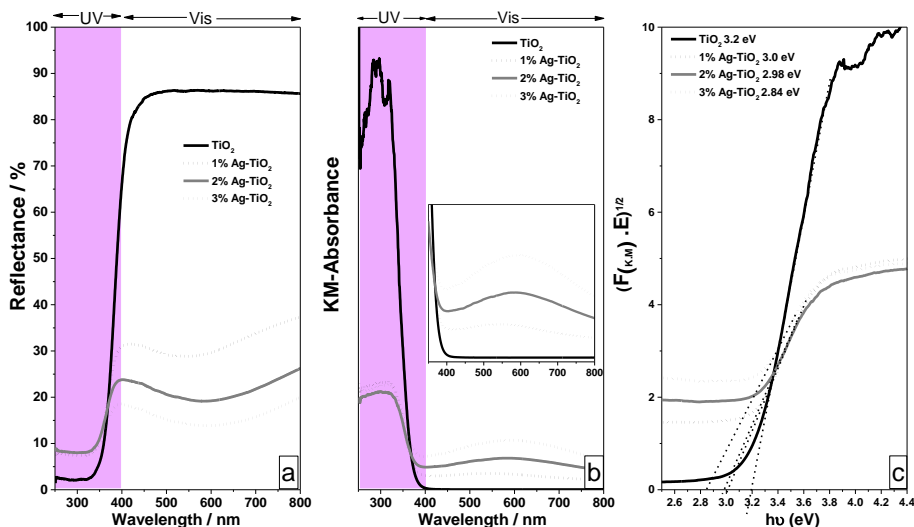


Fig. 32. Optical spectroscopy. a) Diffuse reflectance (%) spectra of  $\text{TiO}_2$  doped with silver (1, 2 and 3% mol) with the corresponding b) Kubelka-Munk absorption curves, c) Determination of band gap.

It is also noteworthy that the visible light absorption peaks of the various Ag doping are unchanged, except the intensities but additional plasmonic band can be seen on the optical spectra.

The peak position in the absorption spectrum depends on various factors, as the temperature of annealing, concentration, agglomeration of silver nanoparticles, silver precursors, and particle size, among others. The peak absorption formed in the visible region corresponds to a behavior generated by silver particles on the surface of  $\text{TiO}_2$  at temperatures higher than 400 °C [42].

### 2.4.7 Chemical Analysis by XPS of $\text{TiO}_2$ :Ag powders.

XPS spectroscopy was employed for the determination of the chemical state of Ag and Ti in the annealed samples. The Fig. 33 shows the XPS spectrum of 3%Ag- $\text{TiO}_2$  powder and it is compared with the pure  $\text{TiO}_2$  powder.

The strong existence of silver nanoparticles can be distinguished by the center peaks at the binding energies of 368.1 and 374.09 eV corresponding to Ag  $3d_{5/2}$  and Ag  $3d_{3/2}$ , see Fig. 33 a). These results confirm the existence of silver nanoparticles as evidence by Raman spectroscopy [3, 41, 43]. The existence of AgO was not shown as the corresponding lines must appear at the binding energy of 367.7 eV for Ag  $3d_{5/2}$  [44], besides has been reported that the bonds Ag-Ag and Ti-O are stronger than the chemical bond of Ag-O, which favors the metallic silver cluster formation [45]. The XPS spectra for O 1s and Ti2p is shown in the Fig. 33 b) and c). It can be observed that the peaks for the samples of  $\text{TiO}_2$  pure and doped powders have the same binding energy. For the Ti  $2p_{3/2}$  its binding energy of 458.70 eV and 464.42 eV for Ti  $2p_{1/2}$ . For O 1s a binding energy of 530.07 is expected.

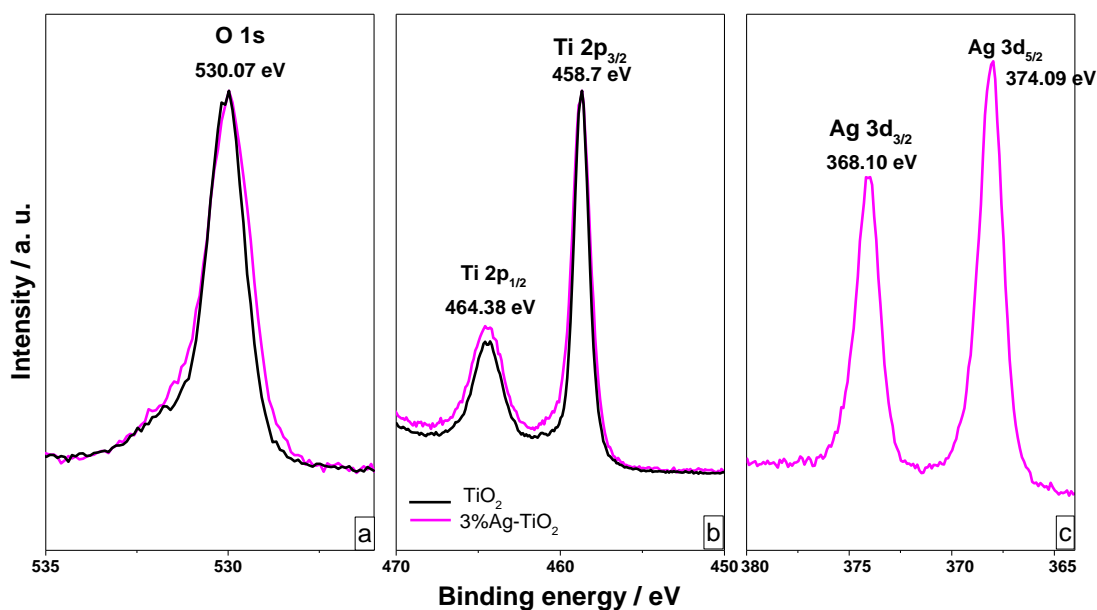


Fig. 33. XPS spectra of 3%Ag- $\text{TiO}_2$  annealed at 500°C.

In the Table 14 are summarized the binding energies corresponding to the XPS analysis. It can be observed a broadening of the peaks of  $2p_{3/2}$ ,  $2p_{1/2}$  and O1s of the 3%Ag- $\text{TiO}_2$  powder in comparison with the pure  $\text{TiO}_2$  powders. According to Young Ku et al. [46], as the amount of silver

incorporated on  $TiO_2$  is increased, the Ti 2p peaks become broader and composed by superposition of XPS at the energies 457.4 eV and 458.7 eV matching the trivalent and tetravalent states of Ti, respectively. It could be a consequence of the presence of  $Ti^{3+}$  resulting from the incorporation of Ag ions inside the host titania.

Table 14. XPS binding energies of 3%Ag- $TiO_2$  powder.

	Binding energy / eV				
	Ti2p <sub>3/2</sub>	Ti2p <sub>1/2</sub>	O1s	Ag 3d <sub>3/2</sub>	Ag 3d <sub>5/2</sub>
$TiO_2$	458.7	464.38	530.07	-	-
3%Ag- $TiO_2$	458.35	464.38	530.07	374.09	368.10

## 2.4.8 Photocatalytic evaluation of $TiO_2:Ag$ powders.

The photodegradation of organic dyes as (methylene blue  $2 \times 10^{-5}$  Mol) by Ag doped  $TiO_2$  powders annealed at 500 °C were irradiated with light from a Xenon lamp. The irradiation power was of 120 mW/cm<sup>2</sup> and the distance of 70 cm between the lamp and the sample. A magnetic stirring was used during the test.

The photocatalysis was characterized by, the absorbance of the methylene blue measured with a VIS spectrometer in intervals of 10 minutes. Fig. 26 shows the optical absorption of MB for the samples of  $TiO_2$  doped powders with silver (1, 2 and 3 %mol). These spectra were integrated for the area under a curve measurements.

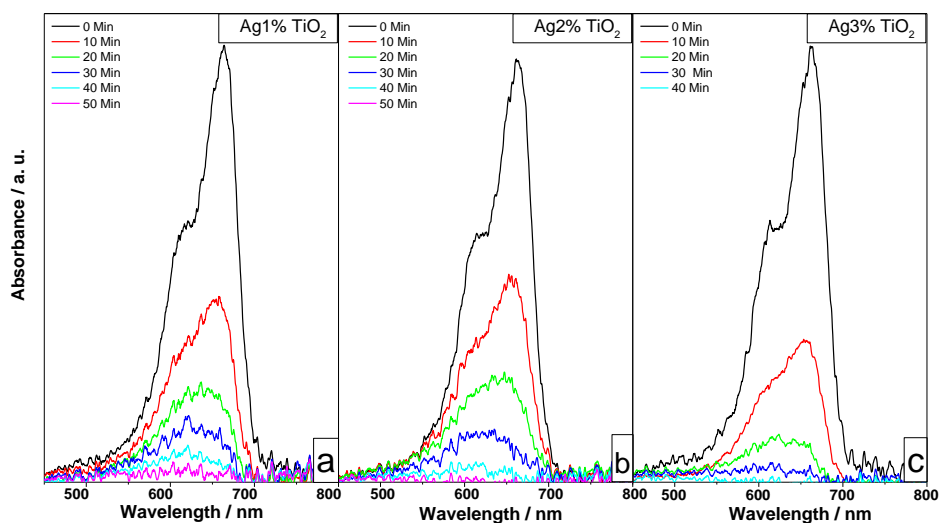


Fig. 34. Absorption spectra of methylene blue photodegradation by  $TiO_2$  doped with silver (1, 2 and 3% mol).

The first order kinetics of methylene blue photodegradation by  $\text{TiO}_2$  doped with silver (1, 2 and 3% mol) are shown in Fig. 35. The doping samples present a higher constant rate in comparison with  $\text{TiO}_2$  pure, not for the doping with 1% mol.

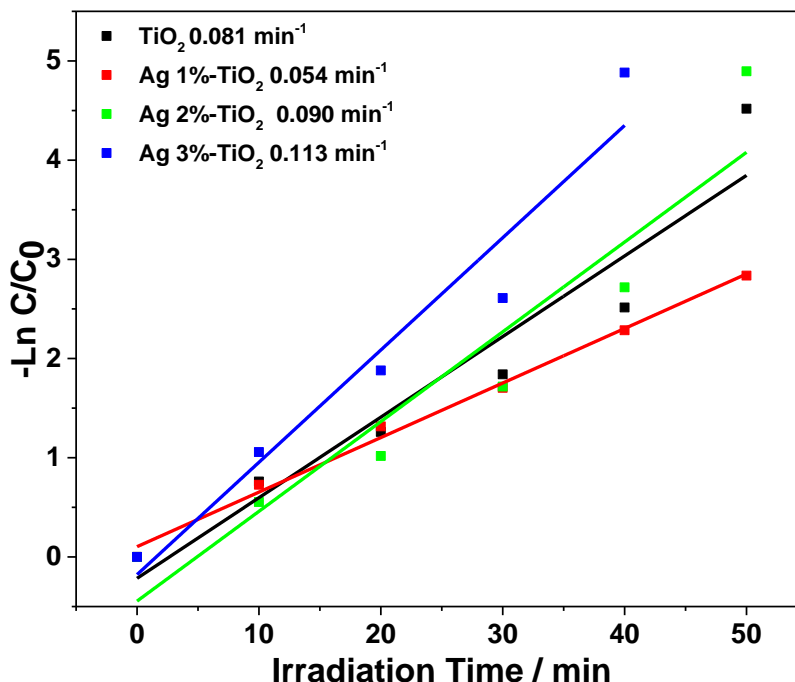


Fig. 35. First order Kinetics of methylene blue photodegradation by  $\text{TiO}_2$  doped with silver (1, 2 and 3% mol).

The samples of  $\text{TiO}_2$  doped with silver show a higher constant rate in comparison of pure  $\text{TiO}_2$ , this is because the Fermi level of Ag is lower than that of  $\text{TiO}_2$  so that electrons may transfer to the Ag deposited on surface of  $\text{TiO}_2$ , which this induce a decrease in the outer electron cloud density on Ti ion. The accumulation of electrons on silver particles results in the negative charge enrichment of the metal surface. This enhances the separation of reduction and oxidation surface site. Hence, the extent of surface recombination is lowered and availability of holes and electrons for redox. Subsequently, electrons migrate from silver-laden particles to  $\text{O}_2$  molecules. Moreover, the density of free electrons in Ag– $\text{TiO}_2$  coatings is less than in the pure  $\text{TiO}_2$  coating and will promote the photoabsorption of  $\text{O}_2$  molecules on the surface of photocatalysts. Therefore, the rate of electron transfer to oxygen increases and the recombination rate of electron/hole pairs decreases [46-48].

### 2.5.1 Phase identification by XRD of $TiO_2:Eu$ powders. *Effect of the temperature.*

$TiO_2$  doped with europium synthesized by the sol-gel technique and were analyzed by x-ray diffraction for the crystalline phase determination. The annealed temperatures were varied to find a stable anatase phase.

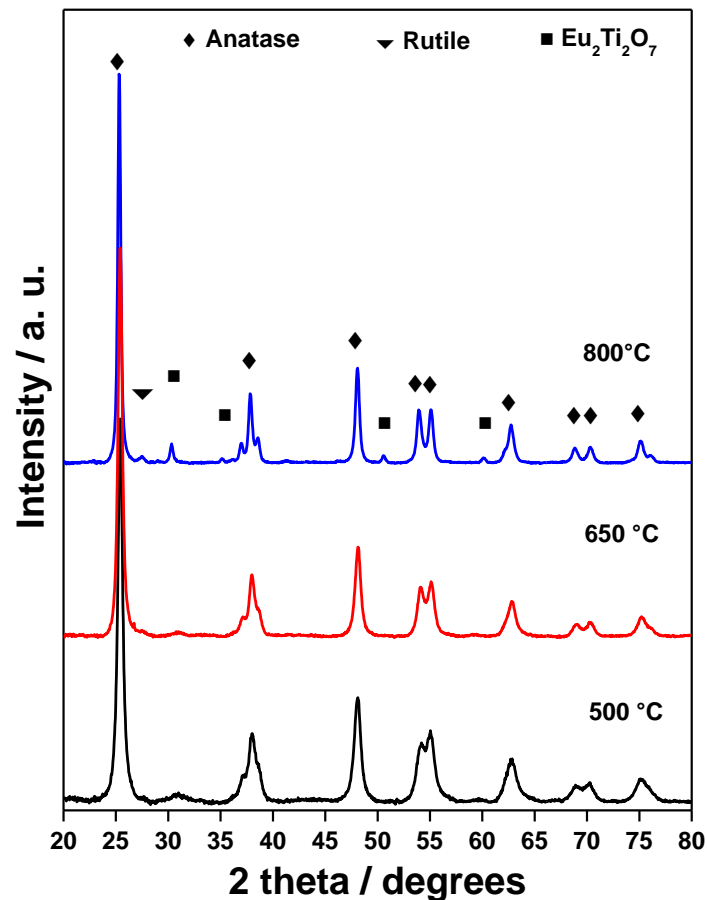


Fig. 36. X-ray diffractograms of 3%Eu- $TiO_2$  annealed at different temperatures.

In the Fig. 36 can be observed the behavior of the 3%Eu- $TiO_2$  at different thermal treatments. It can be shown that the anatase phase is present even at the highest temperature about 800 °C in comparison with pure  $TiO_2$ . Europium ions will inhibit the phase transition of anatase-to-rutile through the formation of a Ti–O–Eu bond. The  $Eu_2O_3$  lattice locks the Ti–O species at the interface with the  $TiO_2$  domains preventing the nucleation that is necessary for anatase transformation to rutile [4].



## 2.5.2 Phase identification by XRD of $\text{TiO}_2$ :Eu powders. *Effect of the concentration.*

The samples doped with europium which maintains the anatase phase even at 800 °C (JPCDS-01-089-4921) and only minor fraction of rutile phase appears. This is in contrast to the samples doped with silver and copper at 800°C which show a complete rutile phase was achieved. The samples doping with europium at 1, 2 and 3% mol were annealed at 800 °C. For the sample 3%Eu- $\text{TiO}_2$ , it could be observed a peak corresponding to  $\text{Eu}_2\text{Ti}_2\text{O}_7$  (JCPDS 01-087-1852), Fig. 37. Yuhong et al [4], established that this remarkable shift of crystallization and the phase transformation to high temperatures is caused by the substitution of titanium ions by europium ions within the structural framework. However, no such a conclusion can be drawn since we do not show the incorporation of Eu ions in the lattice from the EPR investigations discussed below. Thus, the location of minor phase, rich in Eu, prevent the coalescence of  $\text{TiO}_2$  particles.

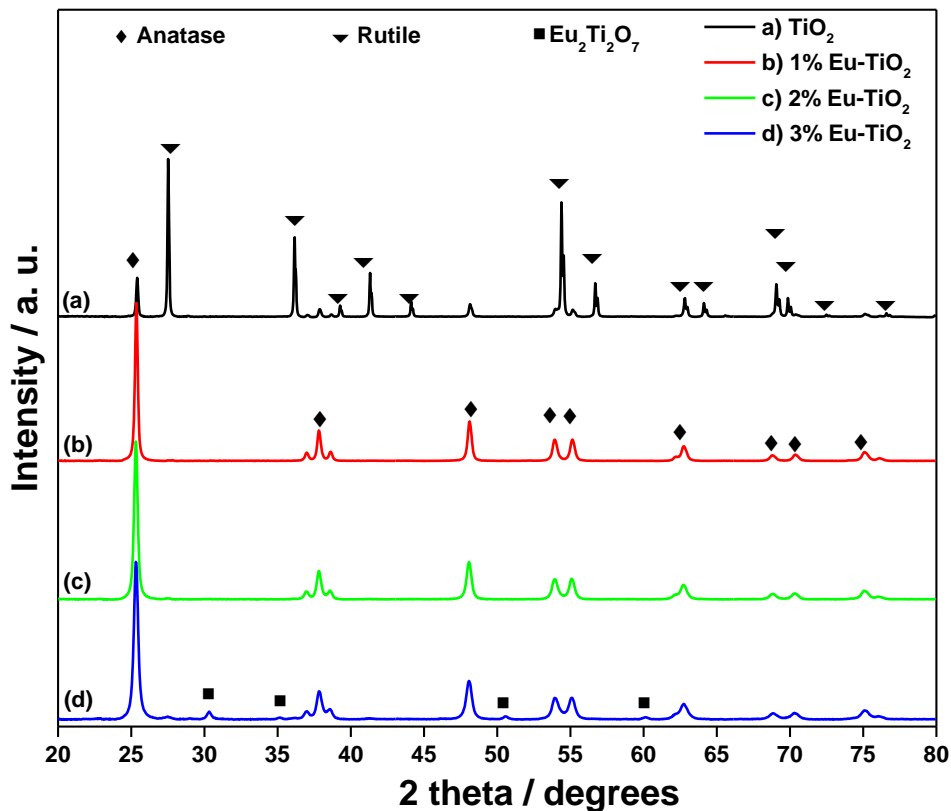


Fig. 37. X-ray diffractogram of  $\text{TiO}_2$  doped with europium (1, 2 and 3% mol) annealed at 800°C.

The diffractograms of  $\text{TiO}_2$  doped with Europium were fitted using High Score Plus software, for determining the peaks position in 2θ corresponding to the main plane of the anatase phase

(101), and for the measurement of the FWHM, showed in Table 15 Table 4. The peaks position of the plane (101) was located at values very similar of  $2\theta$ . The FWHM changed is induced due to the doping effect, this variation is related to the crystallite size caused by the effect of  $Eu^{2+}$  and the high annealing temperature.

Table 15. Peak analysis of the main peak corresponding to the plane (101) from anatase phase, for  $TiO_2$  doped with europium (1, 2 and 3 % mol):

Sample	Peak position of the plane (101) / degrees	Full width at half medium
$TiO_2$	25.35	0.242
1%Eu- $TiO_2$	25.32	0.204
2%Eu- $TiO_2$	25.29	0.272
3%Eu- $TiO_2$	25.30	0.326

According to the particle size estimated, see Table 16, it decrease as the europium concentration increase, this due the Eu ions suppresses the growth of  $TiO_2$  nanocrystals to a great extent [49].

Table 16. Crystallite size for  $TiO_2$  doping with europium (1, 2 and 3% mol).

	$TiO_2$ pure	1% Eu- $TiO_2$	2% Eu- $TiO_2$	3% Eu- $TiO_2$
Crystallite size	20 nm	44 nm	28 nm	25 nm

### 2.5.3 Phase identification by Raman spectroscopy of $\text{TiO}_2\text{:Eu}$ powders.

The Raman modes of the anatase are associated to the bands at 43, 396, 516 and 641  $\text{cm}^{-1}$  corresponding to the doping with Europium (1, 2 and 3% mol). For pure  $\text{TiO}_2$ , at 800°C a mix of phases of anatase and rutile is present. The bands corresponding to  $\text{Eu}_2\text{Ti}_2\text{O}_7$  were not identified by Raman spectroscopy, it could be due to the small concentration of the Europium ions. As the Raman bands are well resolved and sharp, we may conclude the good crystalline quality of the host titania. The effect of Eu doping seems not to affect the Raman spectra. This is a consequence of phase segregation of Eu from the titania lattice.

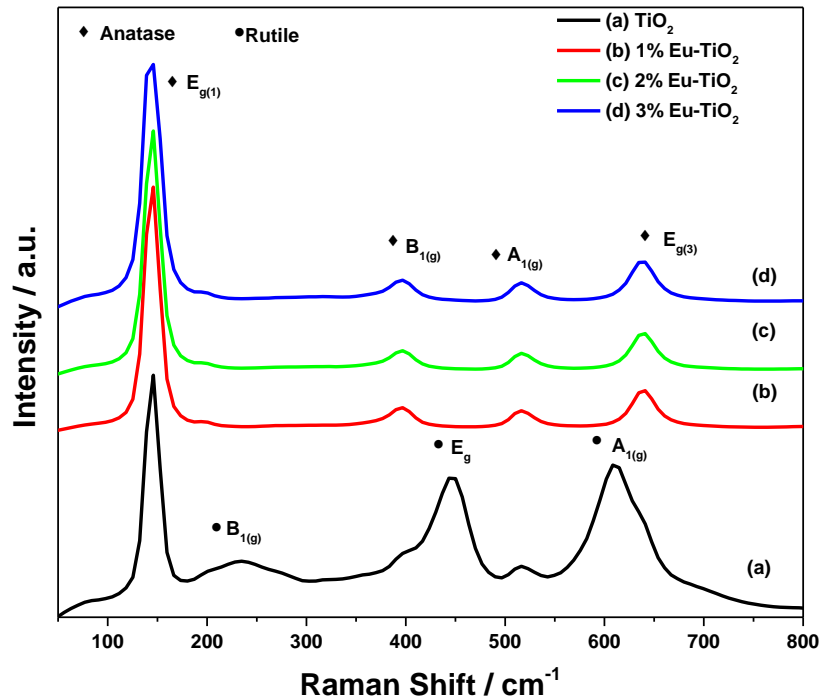


Fig. 38. Raman spectra of  $\text{TiO}_2$  doped with europium (1, 2 and 3% mol) annealed at 800°C.

An adjustment of the Raman spectra was realized for the main vibration mode  $E_{g1}$ , using the Voigt function. The aim is to reveal the effect of EU doping on the vibrational properties of Titania structure, see Table 17. Increased oxygen vacancies in the crystal structure of  $\text{TiO}_2$  induce a shift of the wavenumber of the anatase  $E_g$  mode (144  $\text{cm}^{-1}$ ). This may imply that the discrepancies in

the oxygen vacancy level have not been significant enough to cause Raman band shifting. This is understood from the rather limited substitutional  $\text{Eu}^{3+}$  doping in the  $\text{TiO}_2$  lattice [50].

Table 17. Analysis of the main Raman peak of the anatase  $E_{g1}$  of  $\text{TiO}_2$ :Eu.

Samples	$E_{g1}$ peak position / $\text{cm}^{-1}$	Full width at half medium.
$\text{TiO}_2$	144.7	17.21
1%Eu- $\text{TiO}_2$	144.45	18.20
2%Eu- $\text{TiO}_2$	144.68	18.58
3%Eu- $\text{TiO}_2$	144.08	21.09

### 2.5.4 BET surface area measurements of $\text{TiO}_2$ :Eu powders.

The BET surface area, pore volume and pore size of the  $\text{TiO}_2$  pure and the  $\text{TiO}_2$  doped with europium, are shown in Table 18. The sample doping has a lower surface area than pure  $\text{TiO}_2$ . This could be due to the high annealing temperature for the anatase stabilization, favoring the particles growth and agglomeration. The particle size was determined by the BET surface area method.

Table 18. BET surface area, pore volume and pore size of  $\text{TiO}_2$ :Eu.

Sample	BET surface area / $\text{m}^2 \text{g}^{-1}$	Pore volume / $\text{cm}^3 \text{g}^{-1}$	Poro size / nm	Average particle diameter / nm
$\text{TiO}_2$ at $500^\circ\text{C}$	31.3324	0.078245	9.989	49 nm
3%Eu- $\text{TiO}_2$ at $800^\circ\text{C}$	10.0270	0.044292	17.66	153 nm

However, we may note that the great difference in the annealing temperature can explain such difference in the particle size. The role of Eu doping is quite minor at this stage since as shown by EPR (seem below) the doping ions have tendency at this temperature to segregate from host titania.

### 2.5.5 EPR evaluation of $\text{TiO}_2$ :Eu powders.

The Eu doping seems the more critical among the above-used elements. The features of the spectra are less resolved and we do not see the characteristic U forms which are reported for this ions in its valence state  $\text{Eu}^{2+}$ . In that case, the electronic spin is  $S=7/2$  and characteristic lines must be seen in the spectra. Instead, we only notice large signals (Fig. 39) with intensities correlated with the doping ratios (1, 2, 3 at.%). However, the absence of characteristic ( $S=7/2$ )  $\text{Eu}^{2+}$  EPR lines due to the incorporation of Eu ions in the host crystalline sites can be understood by the large departure between Eu ionic radius almost twice that of  $\text{TiO}_2$ . However, the existence of weak and broad EPR signal with intensity correlated with the doping rates underlines the involvement of  $\text{Eu}^{2+}$  in the samples. The weak intensity reflects a small fraction of Eu ions in the valence states  $\text{Eu}^{2+}$  and the large line width can be explained probably by clustering of  $\text{Eu}^{2+}$  ions submitted to exchange interactions. According to XRD investigations have shown a phase segregation with rich europium ions as  $\text{Eu}_2\text{Ti}_2\text{O}_7$  within the titania host matrix. As the valence

state  $\text{Eu}^{3+}$ , no EPR signal can be obtained from such ions. Also, the above results are consistent with the Europium ions being mainly in the valance state  $\text{Eu}^{3+}$ . In addition, the exposure of  $\text{Eu-TiO}_2$  to Xe-Lamp radiation as it was experienced with the other doping ions, didn't show any modification of the EPR spectra. This means that the photoactive efficiency of  $\text{Eu}$ -doped titania must be quite different compared to the other doping elements as it is discussed in forthcoming section.

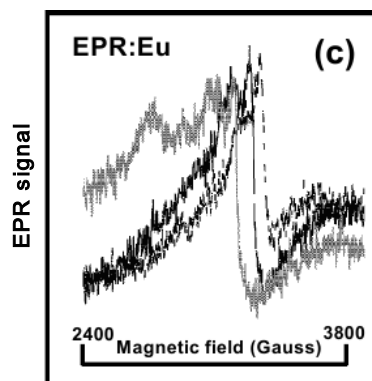


Fig. 39. EPR spectra of  $\text{Eu-TiO}_2$  at different concentrations 3 at.% (grey line), 2at.% (thick black line), 1 at.% (dashed line).

### 2.5.6 Optical characterization of $\text{TiO}_2$ :Eu powders.

The samples doped with Europium show an optical behavior similar to that of the pure  $\text{TiO}_2$ . The absorption in the UV region is associated to the  $\text{O}^{2-}(2p) \rightarrow \text{Ti}^{4+}(3d)$  charge transfer process [17]. The absorption peaks of  $\text{Eu}^{3+}$  appear at 210 and 250 nm for the transitions  $5d \leftarrow 4f$ , and at 394 and 464 nm for  ${}^7\text{F}_0 \rightarrow {}^5\text{L}_6$  and  ${}^7\text{F}_0 \rightarrow {}^5\text{D}_2$ , see Fig. 40 a).

The band gap decrease when the concentration of the rare earth dopant increase [51]. The variation in the optical band edge could occur due to the incorporation of localized impurity states owing to  $\text{Eu}^{3+}$  doping [5], see Fig. 40 c).

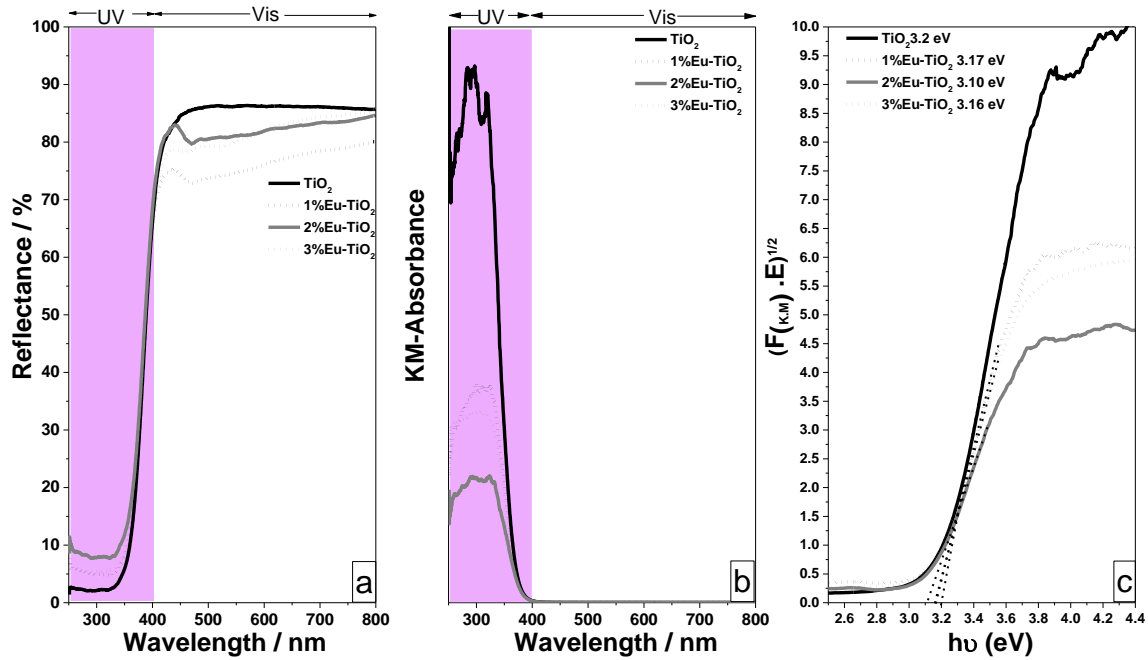


Fig. 40. Optical spectroscopy. a) Diffuse reflectance (%) spectra of  $\text{TiO}_2$  doped with europium (1, 2 and 3% mol) with the corresponding b) Kubelka-Munk absorption curves, c) Determination of band gap.

### 2.5.7 Chemical Analysis by XPS of $\text{TiO}_2$ :Eu powders.

XPS spectroscopy was employed for the determination of the chemical state of Eu and Ti in the annealed samples. The Fig. 41 shows the XPS spectrum of 3%Eu- $\text{TiO}_2$  and it is compared with the  $\text{TiO}_2$  pure.

The peak at 1134 eV of the doping sample corresponds to the Eu  $3d_{5/2}$ . The binding energy positions were attributed to Eu(III). There were observed two peaks at 1125 and 1154 eV that could be attributed to shake satellites of Eu 3d. These peaks have also been attributed to Eu(II) present on the surface. It is possible that Eu(III) will be reduced to Eu(II) when oxygen defects are created [52].

The Fig. 41 b) and c), show the XPS spectra for the O 1s and Ti 2p. It can be observed that the peaks for the samples of  $\text{TiO}_2$  pure and doped have the same binding energy. For the Ti  $2p_{3/2}$  has a binding energy of 458.70 eV and 464.42 eV for  $\text{Ti}2p_{1/2}$ . For O 1s has a binding energy of 530.07. It can suggest that the  $\text{Eu}^{3+}$  ions are likely distributed at the surface or near the surface of the nanoparticle [53].

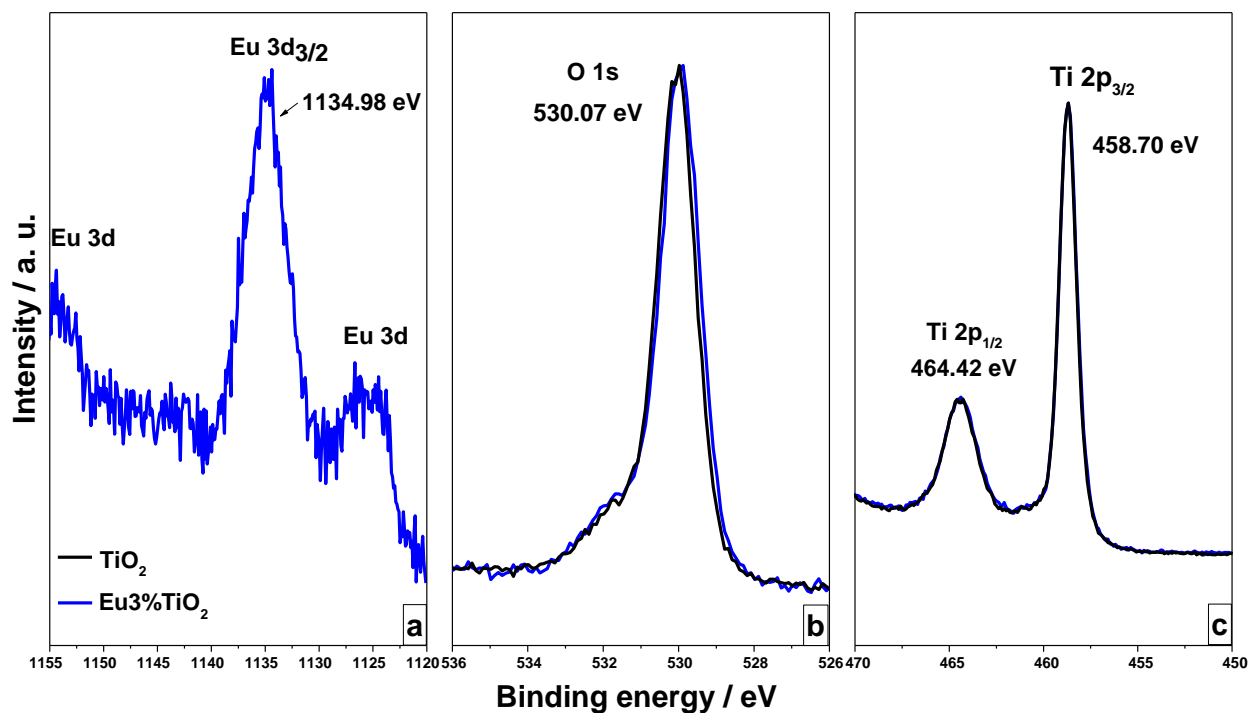


Fig. 41. XPS spectra of 3%Eu- $\text{TiO}_2$  annealed at 500°C.



### 2.5.8 Photocatalytic evaluation of $TiO_2:Eu$ powders.

The photodegradation of the dye (methylene blue  $2 \times 10^{-5}$  Mol) by  $TiO_2$  doped annealed at  $800^\circ C$  were irradiated with light from a Xenon lamp. The irradiation power was from  $120 \text{ mW/cm}^2$  and a distance of 70 cm between the lamp and the sample. In solution also submitted to magnetic stirring. During the photocatalytic process test, the absorbance of the methylene blue was measured with a VIS spectrometer in intervals of 10 minutes. The Fig. 42 shows the methylene blue spectra for the samples of  $TiO_2$  doped with europium (1, 2 and 3 %mol). These spectra were integrated for the area under a curve measurements.

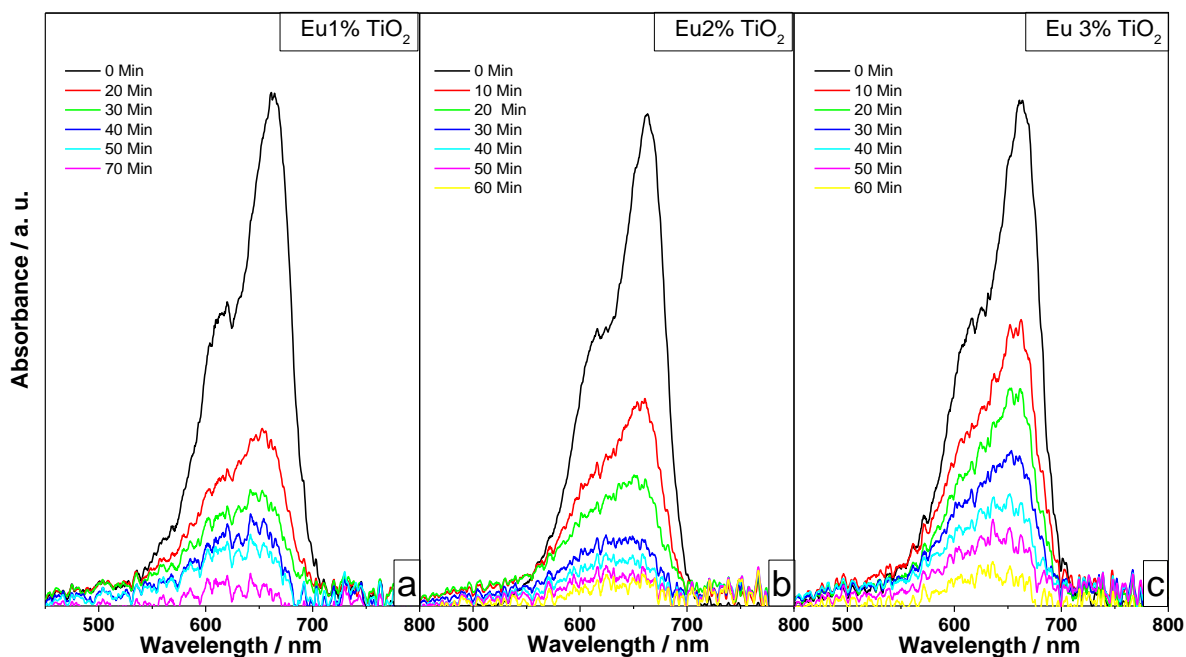


Fig. 42. Absorption spectra of methylene blue photodegradation by  $TiO_2$  doped with europium (1, 2 and 3% mol).

The first order kinetics of methylene blue photodegradation by  $TiO_2$  doped with europium (1, 2 and 3% mol) are shown in Fig. 43. The doping samples present a lower constant rate in comparison with  $TiO_2$  pure.

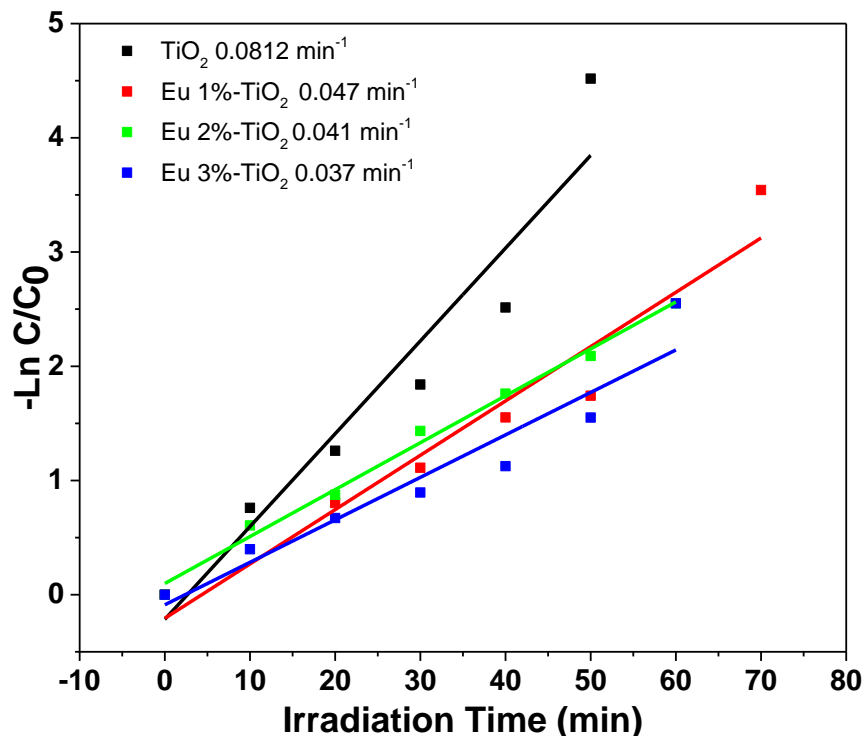


Fig. 43. First order Kinetics of methylene blue photodegradation by  $\text{TiO}_2$  doped with silver (1, 2 and 3% mol).

According to some reports, doping with concentrations lower than 0.5 mol, improve the photocatalytic degradation. However when the concentration of doping ions is high, the space charge region becomes very narrow and the penetration depth of light into  $\text{TiO}_2$  greatly exceeds the space charge layer; therefore the recombination of the photogenerated electron–hole pairs in semiconductor become easier decreasing the photocatalytic activity of the  $\text{TiO}_2$  for the methylene blue degradation process [6, 51]. Excess amounts of rare earth oxide covering the surface of  $\text{TiO}_2$  would increase the number of recombination centers and result in low photoactivity [54].

## 2.6 .Conclusions.

### 2.6.1 Comparative conductivity versus doping.

Electrical characterizations were carried out on the pure and metal-doped  $\text{TiO}_2$  in order to compare the thermal behavior of their electrical conductivity in the permanent regime. The obtained results are summarized in a semi-logarithmic plot depicted in Fig. 44, where thermally activated conductivity was reported with values up to  $0.1 \text{ S.m}^{-1}$ . However, irrespective to the doping element, no improvement of the conductivity was realized by doping and even the tendency is a decrease of the conductivity for doping elements such as Cu and Eu. Several reasons may be considered to account for the decrease of the conductivity. Particularly, due to the required neutrality in the substitutional sites, doping may induce the creation of oxygen vacancies which act as traps for electrons of  $\text{TiO}_2$  usually considered as an n-type semiconductor. The presence of oxygen vacancies induces the formation of energetically favorable valence state as  $\text{Ti}^{3+}$ . This is clearly demonstrated by EPR investigations in Cu-doped samples by the occurrence of EPR spectra related to paramagnetic  $\text{Ti}^{3+}$  involved in the lattice with a density estimated to  $10^{17} \text{ Ti}^{3+} \text{ ion/gram}$ . Thus, EPR and conductivity measurements give complementary information on the role of  $\text{Cu}^{2+}$  ions in  $\text{TiO}_2$ . For doping by Ag and Eu, composite systems are formed and consist of metallic Ag clusters or  $\text{Eu}_2\text{Ti}_2\text{O}_7$  minor phase embedded in the  $\text{TiO}_2$  host media. Such a departure to stoichiometric materials and the heterogeneous distribution of minor phases or clusters limit the charge carrier mobility reducing the hole conductivity of the doped samples compared to pure sample.

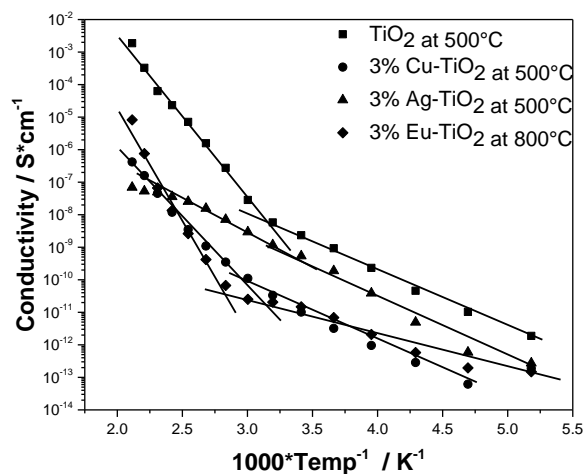


Fig. 44. Semi-log plot of  $\sigma_{dc}$  conductivity versus inverse temperature for pure and metal-doped  $\text{TiO}_2$ .

Conductivity measurements for the concrete mixes have been presented in an Arrhenius format, viz,

$$\sigma = \sigma_0 e^{\left[ \frac{E_a}{R_g T} \right]} \quad \text{Equation 16}$$

where  $\sigma$  is the sample conductivity (S/cm) at temperature T (Kelvin);  $\sigma_0$  the pre-exponential factor and represents the nominal conductivity at infinite temperature;  $E_a$  is the activation energy for the conduction process (J mol<sup>-1</sup>) and  $R_g$  is the Universal Gas constant 8.3141 (J mol<sup>-1</sup> K<sup>-1</sup>). In the work discussed below,  $\ln(\sigma)$  is plotted against  $1000/T$  hence multiplying the slope of the plot by  $R_g$ , obtains  $E_a$  in kJ mol<sup>-1</sup> which is the more usual unit (to convert activation energy in kJ mol<sup>-1</sup> to eV/ion,  $E_a$  should be divided by 96.485). The activation energy can be physically interpreted as the energy barrier that must be overcome for an ion to conduct [55]. The activation values are presented in two temperatures range according to the plot, see Table 19

Table 19. The activation energy of the samples 3%M-TiO<sub>2</sub>.

	Activation energy.	Activation energy.
TiO <sub>2</sub>	0.44 eV ( 193-313 K)	0.15 eV (333-473 K)
3% Cu-TiO <sub>2</sub>	0.37 eV ( 193-333 K)	0.16 eV (353-473 K)
3% Ag-TiO <sub>2</sub>	0.14 eV ( 193-313 K)	0.17 eV (333-473 K)
3% Eu-TiO <sub>2</sub>	0.59 eV ( 193-333 K)	0.10 eV (353-473 K)

## 2.6.2 Comparative performance versus doping.

Comparative investigations were devoted to metal-doped TiO<sub>2</sub> where doping process has shown versatile behavior and dependence on the nature of the used elements. Even, with identical and stable valence states such as (Cu<sup>2+</sup>, Ag<sup>2+</sup>, Eu<sup>2+</sup>), different behaviors were demonstrated for the effective incorporation of these ions in the host structure of TiO<sub>2</sub>. The discrepancy between ionic radii of the different used elements modulates the ratio of the substitutional doping. This is indeed achieved for Cu<sup>2+</sup> but in less extent for Ag<sup>2+</sup> while Europium ions form segregated phase as Eu<sub>2</sub>Ti<sub>2</sub>O<sub>7</sub>. The structural features are also dependent on the doping nature. This is illustrated by an increase or a decrease of the anatase-to-rutile phase transformation temperature. Interestingly, in the case of Eu-TiO<sub>2</sub> nanoparticles, europium preserves the anatase phase at 800°C, while the other samples show a complete rutile phase transformation at a lower

temperature ( $\sim 600^\circ\text{C}$ ). The electronic behavior is also drastically modified and depends on the doping elements with the effective conductivity being lowered compared to the undoped sample. The microstructure changes such with low specific surfaces in doped samples correlate with the formation of metallic clusters for Ag doping or europium oxide clusters for Eu doping. The increase of interfaces and composition changes by such doping may overcome the conduction channels compared to undoped sample.

Alternatively, the red shift of the band gap for all doped samples was clearly noticed with the expectation of harvesting a wide light spectrum for photocatalysis reactions. The experiments on the degradation of methylene blue dyes have shown slight improvement with Ag-doped samples. The reason was tentatively attributed to the Ag clusters which were indeed demonstrated through their plasmon optical band. The induced surface plasmon resonances enhance the intensity of light radiation at the  $TiO_2$  interfaces and improve the efficiency of photocatalytic degradation of dyes in solutions, see Fig. 45.

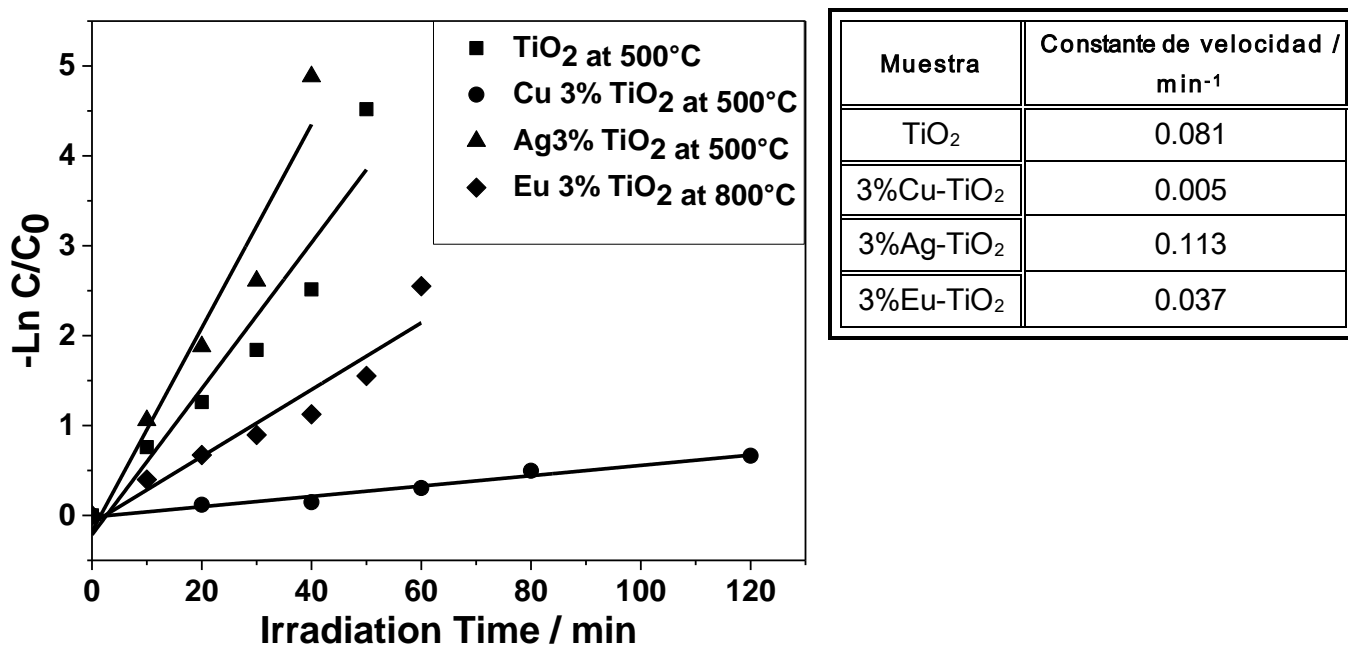


Fig. 45 First order Kinetics of methylene blue photodegradation by 3% M- $TiO_2$  (M=Cu, Ag, and Eu).

## 2.7 Bibliography.


1. Chen, X., *Titanium Dioxide Nanomaterials and Their Energy Applications*. Chinese Journal of Catalysis, 2009. **30**(8): p. 839-851.
2. López, R., R. Gómez, and M.E. Llanos, *Photophysical and photocatalytic properties of nanosized copper-doped titania sol-gel catalysts*. Catalysis Today, 2009. **148**(1-2): p. 103-108.
3. Leong, K.H., B.L. Gan, S. Ibrahim, and P. Saravanan, *Synthesis of surface plasmon resonance (SPR) triggered Ag/TiO<sub>2</sub> photocatalyst for degradation of endocrine disturbing compounds*. Applied Surface Science, 2014. **319**(0): p. 128-135.
4. Zhang, Y., H. Zhang, Y. Xu, and Y. Wang, *Europium doped nanocrystalline titanium dioxide: preparation, phase transformation and photocatalytic properties*. Journal of Materials Chemistry, 2003. **13**(9): p. 2261-2265.
5. Paul, N. and D. Mohanta, *Effective optoelectronic and photocatalytic response of Eu<sup>3+</sup>-doped TiO<sub>2</sub> nanoscale systems synthesized via a rapid condensation technique*. Journal of Materials Research, 2013. **28**(11): p. 1471-1480.
6. Xu, A.-W., Y. Gao, and H.-Q. Liu, *The Preparation, Characterization, and their Photocatalytic Activities of Rare-Earth-Doped TiO<sub>2</sub> Nanoparticles*. Journal of Catalysis, 2002. **207**(2): p. 151-157.
7. Yan, J., G. Wu, N. Guan, L. Li, Z. Li, and X. Cao, *Understanding the effect of surface/bulk defects on the photocatalytic activity of TiO<sub>2</sub>: anatase versus rutile*. Physical Chemistry Chemical Physics, 2013. **15**(26): p. 10978-10988.
8. Zhang, J., M. Li, Z. Feng, J. Chen, and C. Li, *UV Raman Spectroscopic Study on TiO<sub>2</sub>. I. Phase Transformation at the Surface and in the Bulk*. The Journal of Physical Chemistry B, 2006. **110**(2): p. 927-935.
9. Narayanan, P.S., *Raman spectrum of rutile (TiO<sub>2</sub>)*. Proceedings of the Indian Academy of Sciences - Section A, 1950. **32**(4): p. 279-283.
10. Ohsaka, T., F. Izumi, and Y. Fujiki, *Raman spectrum of anatase, TiO<sub>2</sub>*. Journal of Raman spectroscopy, 1978. **7**(6): p. 321-324.
11. Tian, F., Y. Zhang, J. Zhang, and C. Pan, *Raman Spectroscopy: A New Approach to Measure the Percentage of Anatase TiO<sub>2</sub> Exposed (001) Facets*. The Journal of Physical Chemistry C, 2012. **116**(13): p. 7515-7519.
12. Chen, X. and S.S. Mao, *Titanium dioxide nanomaterials: synthesis, properties, modifications, and applications*. Chem Rev, 2007. **107**(7): p. 2891-959.
13. Choudhury, B., M. Dey, and A. Choudhury, *Defect generation, dd transition, and band gap reduction in Cu-doped TiO<sub>2</sub> nanoparticles*. International Nano Letters, 2013. **3**(1): p. 1-8.
14. Takeshi, M., A. Ryoji, O. Takeshi, A. Koyu, and T. Yasunori, *Band-Gap Narrowing of Titanium Dioxide by Nitrogen Doping*. Japanese journal of applied physics, 2001. **40**(6A): p. L561.
15. Hashimoto, K., H. Irie, and A. Fujishima, *TiO<sub>2</sub> photocatalysis: a historical overview and future prospects*. Japanese journal of applied physics, 2005. **44**(12R): p. 8269.
16. Sakthivel, S., M.V. Shankar, M. Palanichamy, B. Arabindoo, D.W. Bahnemann, and V. Murugesan, *Enhancement of photocatalytic activity by metal deposition: characterisation and photonic efficiency of Pt, Au and Pd deposited on TiO<sub>2</sub> catalyst*. Water Research, 2004. **38**(13): p. 3001-3008.
17. Colón, G., M. Maicu, M.C. Hidalgo, and J.A. Navío, *Cu-doped TiO<sub>2</sub> systems with improved photocatalytic activity*. Applied Catalysis B: Environmental, 2006. **67**(1-2): p. 41-51.
18. Petrik, I., G. Krylova, O. Kelyp, L. Lutsenko, N. Smirnova, and L. Oleksenko, *XPS AND TPR STUDY OF SOL-GEL DERIVED M/TiO<sub>2</sub> POWDERS (M= Co, Cu, Mn, Ni)*. Chemistry, 2015. **6**(2): p. 179-189.

19. Xin, B., P. Wang, D. Ding, J. Liu, Z. Ren, and H. Fu, *Effect of surface species on Cu-TiO<sub>2</sub> photocatalytic activity*. Applied Surface Science, 2008. **254**(9): p. 2569-2574.
20. Qiu, X., M. Miyauchi, K. Sunada, M. Minoshima, M. Liu, Y. Lu, D. Li, Y. Shimodaira, Y. Hosogi, Y. Kuroda, and K. Hashimoto, *Hybrid Cu<sub>x</sub>O/TiO<sub>2</sub> Nanocomposites As Risk-Reduction Materials in Indoor Environments*. ACS Nano, 2012. **6**(2): p. 1609-1618.
21. Baltazar, P., V.H. Lara, G. Córdoba, and R. Arroyo, *Kinetics of the amorphous—anatase phase transformation in copper doped titanium oxide*. Journal of Sol-Gel Science and Technology, 2006. **37**(2): p. 129-133.
22. Choudhury, B., M. Dey, and A. Choudhury, *Shallow and deep trap emission and luminescence quenching of TiO<sub>2</sub> nanoparticles on Cu doping*. Applied Nanoscience, 2014. **4**(4): p. 499-506.
23. Sahu, M. and P. Biswas, *Single-step processing of copper-doped titania nanomaterials in a flame aerosol reactor*. Nanoscale Research Letters, 2011. **6**(1): p. 441.
24. Parker, J. and R. Siegel, *Calibration of the Raman spectrum to the oxygen stoichiometry of nanophase TiO<sub>2</sub>*. Applied Physics Letters, 1990. **57**(9): p. 943-945.
25. Duhalde, S., M. Vignolo, F. Golmar, C. Chilotte, C.R. Torres, L. Errico, A. Cabrera, M. Renteria, F. Sánchez, and M. Weissmann, *Appearance of room-temperature ferromagnetism in Cu-doped TiO<sub>2</sub>- $\delta$  films*. Physical Review B, 2005. **72**(16): p. 161313.
26. Cao, G. and Y. Wang, *Nanostructures and Nanomaterials: Synthesis, Properties, and Applications*. 2011: World Scientific.
27. Ibach, H., *Physics of Surfaces and Interfaces*. 2006: Springer Berlin Heidelberg.
28. Pan, X. and Y.-J. Xu, *Fast and spontaneous reduction of gold ions over oxygen-vacancy-rich TiO<sub>2</sub>: A novel strategy to design defect-based composite photocatalyst*. Applied Catalysis A: General, 2013. **459**: p. 34-40.
29. Merupo, V.-I., S. Velumani, K. Ordon, N. Errien, J. Szade, and A.-H. Kassiba, *Structural and optical characterization of ball-milled copper-doped bismuth vanadium oxide (BiVO<sub>4</sub>)*. CrystEngComm, 2015. **17**(17): p. 3366-3375.
30. Ramadevudu, G., M. Shareefuddin, N.S. Bai, M.L. Rao, and M.N. Chary, *Electron paramagnetic resonance and optical absorption studies of Cu<sup>2+</sup> spin probe in MgO–Na<sub>2</sub>O–B<sub>2</sub>O<sub>3</sub> ternary glasses*. Journal of non-crystalline solids, 2000. **278**(1): p. 205-212.
31. Li, G., N.M. Dimitrijevic, L. Chen, T. Rajh, and K.A. Gray, *Role of surface/interfacial Cu<sup>2+</sup> sites in the photocatalytic activity of coupled CuO–TiO<sub>2</sub> nanocomposites*. The Journal of Physical Chemistry C, 2008. **112**(48): p. 19040-19044.
32. Anitha, B. and M.A. Khadar, *Dopant concentration dependent magnetism of Cu-doped TiO<sub>2</sub> nanocrystals*. Journal of Nanoparticle Research, 2016. **18**(6): p. 1-14.
33. Etacheri, V., M.K. Seery, S.J. Hinder, and S.C. Pillai, *Oxygen Rich Titania: A Dopant Free, High Temperature Stable, and Visible-Light Active Anatase Photocatalyst*. Advanced Functional Materials, 2011. **21**(19): p. 3744-3752.
34. Jiang, X., Y. Zhang, J. Jiang, Y. Rong, Y. Wang, Y. Wu, and C. Pan, *Characterization of oxygen vacancy associates within hydrogenated TiO<sub>2</sub>: a positron annihilation study*. The Journal of Physical Chemistry C, 2012. **116**(42): p. 22619-22624.
35. Barakat, M.A. and R. Kumar, *Photocatalytic Activity Enhancement of Titanium Dioxide Nanoparticles*, in *Photocatalytic Activity Enhancement of Titanium Dioxide Nanoparticles*. 2016, Springer. p. 1-29.
36. Choi, W., A. Termin, and M.R. Hoffmann, *The role of metal ion dopants in quantum-sized TiO<sub>2</sub>: correlation between photoreactivity and charge carrier recombination dynamics*. The Journal of Physical Chemistry, 1994. **98**(51): p. 13669-13679.

37. Chao, H.E., Y.U. Yun, H.U. Xingfang, and A. Larbot, *Effect of silver doping on the phase transformation and grain growth of sol-gel titania powder*. Journal of the European Ceramic Society, 2003. **23**(9): p. 1457-1464.
38. Ocwelwang, A.R. and L. Tichagwa, *Synthesis and Characterisation of Ag and Nitrogen Doped  $\text{TiO}_2$  Nanoparticles Supported on A Chitosan-Pvae Nanofibre Support*.
39. Quiñones-Jurado, Z.V., M.Á. Waldo-Mendoza, H.M. Aguilera-Bandin, E.G. Villabona-Leal, E. Cervantes-González, and E. Pérez, *Silver nanoparticles supported on  $\text{TiO}_2$  and their antibacterial properties: effect of surface confinement and nonexistence of plasmon resonance*. Materials Sciences and Applications, 2014. **5**(12): p. 895.
40. Bosnick, K.A., *Raman studies of mass-selected metal clusters*. 2000, University of Toronto.
41. Su, C., L. Liu, M. Zhang, Y. Zhang, and C. Shao, *Fabrication of Ag/ $\text{TiO}_2$  nanoheterostructures with visible light photocatalytic function via a solvothermal approach*. CrystEngComm, 2012. **14**(11): p. 3989-3999.
42. Cuppoletti, J., *Nanocomposites and polymers with analytical methods*. 2011: InTech.
43. Daniel, L.S., H. Nagai, N. Yoshida, and M. Sato, *Photocatalytic activity of vis-responsive Ag-nanoparticles/ $\text{TiO}_2$  composite thin films fabricated by molecular precursor method (MPM)*. Catalysts, 2013. **3**(3): p. 625-645.
44. Eremenko, A., A. Korduban, I. Gnatiuk, N. Vityuk, N. Smirnova, O. Linnik, and Y. Mukha, *Silver and gold nanoparticles on sol-gel  $\text{TiO}_2$ ,  $\text{ZrO}_2$ ,  $\text{SiO}_2$  surfaces: optical spectra, photocatalytic activity, bactericide properties*. 2011: INTECH Open Access Publisher.
45. Léonard, G.L.M., C.M. Malengreaux, Q. Mélotte, S.D. Lambert, E. Bruneel, I. Van Driessche, and B. Heinrichs, *Doped sol-gel films vs. powders  $\text{TiO}_2$ : On the positive effect induced by the presence of a substrate*. Journal of Environmental Chemical Engineering, 2016. **4**(1): p. 449-459.
46. Kuo, Y.-L., H.-W. Chen, and Y. Ku, *Analysis of silver particles incorporated on  $\text{TiO}_2$  coatings for the photodecomposition of o-cresol*. Thin Solid Films, 2007. **515**(7-8): p. 3461-3468.
47. Xin, B., L. Jing, Z. Ren, B. Wang, and H. Fu, *Effects of Simultaneously Doped and Deposited Ag on the Photocatalytic Activity and Surface States of  $\text{TiO}_2$* . The Journal of Physical Chemistry B, 2005. **109**(7): p. 2805-2809.
48. Takai, A. and P.V. Kamat, *Capture, Store, and Discharge. Shuttling Photogenerated Electrons across  $\text{TiO}_2$ -Silver Interface*. ACS Nano, 2011. **5**(9): p. 7369-7376.
49. Pal, M., U. Pal, J.M. Jimenez, and F. Perez-Rodriguez, *Effects of crystallization and dopant concentration on the emission behavior of  $\text{TiO}_2$ :Eu nanophosphors*. Nanoscale Res Lett, 2012. **7**(1): p. 1.
50. Li, J.-G., X. Wang, K. Watanabe, and T. Ishigaki, *Phase structure and luminescence properties of Eu<sup>3+</sup>-doped  $\text{TiO}_2$  nanocrystals synthesized by Ar/ $\text{O}_2$  radio frequency thermal plasma oxidation of liquid precursor mists*. The Journal of Physical Chemistry B, 2006. **110**(3): p. 1121-1127.
51. Štengl, V., S. Bakardjieva, and N. Murafa, *Preparation and photocatalytic activity of rare earth doped  $\text{TiO}_2$  nanoparticles*. Materials Chemistry and Physics, 2009. **114**(1): p. 217-226.
52. Kang, J.-G., Y. Jung, B.-K. Min, and Y. Sohn, *Full characterization of  $\text{Eu}(\text{OH})_3$  and  $\text{Eu}_2\text{O}_3$  nanorods*. Applied Surface Science, 2014. **314**(0): p. 158-165.
53. Almeida, N.A.F., J. Rodrigues, P. Silva, N. Emami, M.J. Soares, T. Monteiro, J.A. Lopes-da-Silva, and P.A.A.P. Marques, *Pressure dependent luminescence in titanium dioxide particles modified with europium ions*. Sensors and Actuators B: Chemical, 2016. **234**: p. 137-144.
54. Khataee, A.R., A. Karimi, R.D.C. Soltani, M. Safarpour, Y. Hanifehpour, and S.W. Joo, *Europium-doped ZnO as a visible light responsive nanocatalyst: Sonochemical synthesis, characterization and response surface modeling of photocatalytic process*. Applied Catalysis A: General, 2014. **488**: p. 160-170.



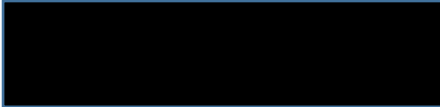
55. McCarter, W., G. Starrs, T. Chrisp, P. Basheer, S. Nanukuttan, and S. Srinivasan, *Conductivity/activation energy relationships for cement-based materials undergoing cyclic thermal excursions*. Journal of Materials Science, 2015. **50**(3): p. 1129-1140.



# CHAPTER III

## TiO<sub>2</sub>:M films

### elaborated by spin-coating and dip coating



### III. TiO<sub>2</sub>:M films elaborated by spin coating and dip coating.

#### 3. Introduction.

TiO<sub>2</sub> has several naturally occurring modifications, the most common ones being rutile, anatase, and brookita polymorphs. Most research on photocatalysis is performed using anatase, while in all other aspects rutile has been much more thoroughly characterized (e.g. electronic behavior, bulk structural investigations). This is mostly due to the preparation methods: While it is easier to obtain anatase than rutile at low temperatures below 600°C, rutile is stable at temperatures above 800°C, which is the transition temperature to the thermodynamically most stable phase rutile.

While TiO<sub>2</sub> powders or films obtained at low temperatures are finely grained (nanocrystalline) because little grain growth can occur, grain growth at temperatures above 800°C can be substantial. Therefore, depending on the preparation method, the nature of the TiO<sub>2</sub> particle or film surface, as well as the active surface area are usually very different for anatase and rutile

---

powders [1]. The present chapter focuses on the elaboration of thin films of  $\text{TiO}_2$  doped with metallic ions (Cu, Ag, and Eu) by two methods of fabrications: spin coating and dip coating.

### 3.1 Surfactants and nanoscience.

Surfactants are amphiphilic molecules—that is, they have one part prefers water and another part prefers oil. These dual characteristics give them a range of properties connected to two key behaviors—adsorption at interfaces and self-assembly in solution. The molecular group possesses the head group which may be charged or may be polar due to the inclusion of oxygen or similar atoms; the tail group generally comprises hydrocarbon chains [2].

It is clear that a vast range of chemical groups can fulfill these requirements, and so, a large number of chemically different surfactants are possible.

Among the well known surfactant, Pluronic F 127 was employed for the fabrication of the films. The objective is to increase the surface area for increasing the contact between the semiconductor and the dye (methylene blue), in the photocatalysis test.

### 3.2 Experimental design.

The  $TiO_2:M$  films elaboration was carried out following the next experimental design, see Table 20.

Table 20. Experimental design for  $TiO_2$  doping with metallic ions (Cu, Ag y Eu) and  $TiO_2$  pure.

	Spin Coating	Dip coating.
$TiO_2$	450°C	450°C
$TiO_2:\%Cu$	3% mol at 450°C	3% mol at 450°C
$TiO_2:\%Ag$	3% mol at 450°C	3% mol at 450°C
$TiO_2:\%Eu$	3% mol at 450°C	3% mol at 450°C

### 3.3 Synthesis of $TiO_2$ :Metal thin films.

The experimental procedure is detailed below.

#### 3.3.1 Materials.

The  $TiO_2$  pure and doped were synthesized by the soft chemical method sol-gel using titanium isopropoxide (IV) as a precursor. The reactants used are listed below:

- Titanium (IV) isopropoxide (TTIP) of Strem Chemicals.
- Acetic acid of Fisher Scientific.
- 2-Propanol (99.5%) de Alfa Aesar GmbH.
- Anhydrous copper (II) acetate (98%) of Alfa Aesar GmbH.
- Hydrated europium (III) acetate (99.9%) of Strem Chemicals
- Silver acetate (99%) of Strem Chemicals.
- Pluronic F-127.

### 3.3.2. Preparation of the sol for $TiO_2$ thin films elaboration.

The synthesis procedure for  $TiO_2$  nanoparticles consists in adding 3.3 ml of TTIP to 5.8 ml of 2-propanol used as a solvent. The mixture was kept under vigorous magnetic stirring for 15 min at room temperature. Then, 3.0 ml of acetic acid was added and the stirring performed for 30 min. In another flask, 0.52 g of F127 was mixed with 3 ml of 2-Propanol and were stirred until getting a complete dissolution. The both solutions were mixed and stirred for 30 minutes. The sol was kept close to avoid the contact with humidity of the environment.

### 3.3.3 Preparation of the sol for $TiO_2$ doped with metallic ions.

The experimental procedure for the synthesis of metal-doped  $TiO_2$  films (with a metal ratio of 3 mol. %) was performed by using TTIP and ethanol as solvent under vigorous magnetic stirring for 15 min. For the doping process, appropriate amounts of copper acetate or silver acetate were added to the solution and stirred until a clear solution was formed, and then the procedure described above was followed. For the Eu-doping, the solution was hermetically closed and ultrasonicated for 2 hours, then heated at  $60^\circ C$  in an air oven for 12 hours and ultrasonicated again for 2 hours before adding the acetic acid. In another flask, 0.52 g of F127 was mixed with 3 ml of 2-Propanol and were stirred until getting a complete dissolution. The both solutions were mixed and stirred for 30 minutes. The sol was kept close to avoid the contact with humidity of the environment.

### 3.3.4 Cleaning of the substrates.

Two kinds of substrates were employed: borosilicate and silicon crystalline. The silicon crystalline was employed for AFM analysis and Raman spectroscopy. The substrates were immersed in ethyl alcohol and were ultrasonicated for lapses of ten minutes. The substrates dimensions were 15 mm x 15 mm.

### 3.3.5 $TiO_2$ films elaborated by dip coating.

The  $TiO_2$  pure and  $TiO_2:M$  films were elaborated with the sols described in sections 3.3.2 and 3.3.3, by the immersed technique, which consists of immersing the substrate in the solution and

then it is withdrawn with a constant speed according to many tests made previously (results are not shown).

The conditions for thin films elaboration are below.

Immersion speed: 100 mm/s

Withdrawn speed: 5 mm / s

Covered surface area: 1 cm<sup>2</sup>.

Number of deposits: 3

Subsequently, the films were dried in air and then annealed in air at 450 °C for 30 min with an air cooling.

### **3.3.6 $TiO_2$ films elaborated by spin coating.**

The  $TiO_2$  pure and  $TiO_2:M$  films were elaborated with the sols described in sections 3.3.2 and 3.3.3, by spin technique, which consists in putting a drop of the sol in the center of the substrate submitted to it is spinning with an established speed for 30 seconds. The speed of spinning was established according to tests done previously (results are not shown).

The conditions for thin films elaboration are below.

The speed of spinning: 5000 rpm.

Number of layers: 3

Subsequently, the films were dried in air and then annealed in air at 450 °C for 30 min with an air cooling.

### 3.4 Phase identification by XRD of $\text{TiO}_2\text{:M}$ films elaborated by spin coating.

The films of  $\text{TiO}_2$  synthesized by the sol-gel and elaborated by spin coating were analyzed by XRD for determination of the crystalline phase. The samples were annealed at  $450\text{ }^\circ\text{C}$  for 30 minutes.

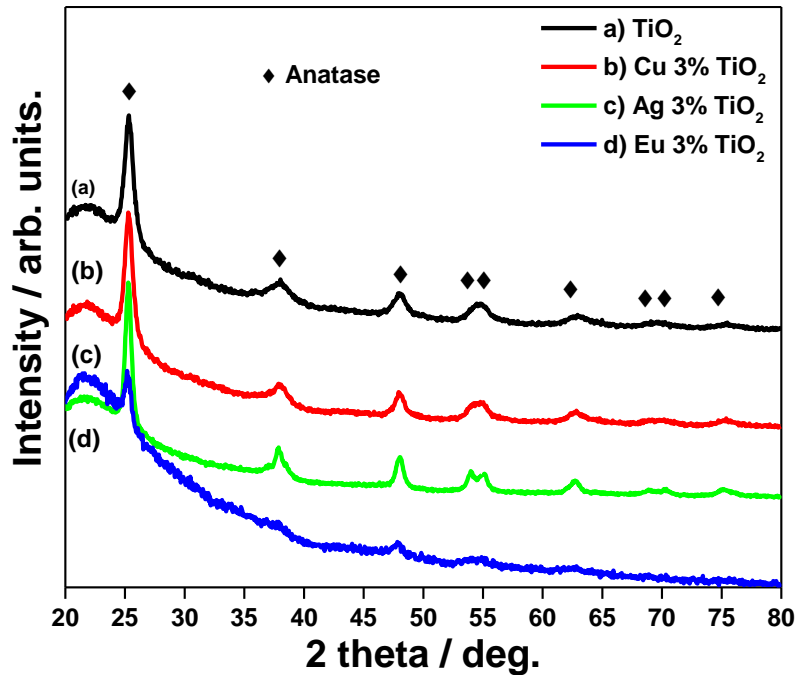


Fig. 46 X-ray diffractograms of 3%M- $\text{TiO}_2$  films (Cu, Ag, and Eu) annealed at  $450\text{ }^\circ\text{C}$  elaborated by spin coating.

For the films of  $\text{TiO}_2$  pure and  $\text{TiO}_2\text{:M}$  annealed at  $450\text{ }^\circ\text{C}$  the anatase phase is present ((JPDCS-01-089-4921)). The film of  $\text{Ag}3\%\text{-TiO}_2$  shows a better peak definition in comparison with the other samples, it could be due the radius of  $\text{Ag}^+$  ion (ca. 126 pm) is much larger than that of  $\text{Ti}^{4+}$  ion (ca. 68 pm), the  $\text{Ag}^+$  ions introduced by the sol-gel process could not enter into the lattice of anatase phase to form a stable solid solution. During the drying and calcination process with the elimination of liquids and organic substance and the crystallization of anatase phase, the uniformly dispersed  $\text{Ag}^+$  ions would gradually migrate from the volume of anatase grains to the surface and further to the surface of the  $\text{TiO}_2$  powder under the action of heat. The density of surfaces defects at the surface of anatase grains then increases, which favors the rutile

nucleation. Therefore the crystallization is improved for this system in comparison with the  $TiO_2$  pure.

In the case of the film of 3%Cu- $TiO_2$ , according to the results for the same system in powder, there is a copper incorporation in the titania lattice, favoring the presence of oxygen vacancies. The diffractogram shows a quality similar than in pure  $TiO_2$ .

For the film of 3%Eu- $TiO_2$ , the peaks intensity have not a good definition; it means that the film has not a good crystallization. This result is in accordance with the already reported results for powders. Europium ions will inhibit the phase transition of anatase-to-rutile through the formation of a Ti-O-Eu bond. It is necessary to increase the annealing temperature to obtain well crystalline anatase phase. However at higher temperature can contaminate the semiconductor with impurities of the substrate.



### 3.5 Phase identification by Raman spectroscopy of pure $TiO_2$ and $TiO_2:M$ 3% mol, elaborated by spin coating.

For pure and doped  $TiO_2$  Raman bands at 145, 396, 516 y 641  $cm^{-1}$  were detected corresponding to the anatase Raman modes for the films elaborated by spin and dip coating. An extra signal corresponding to silicon of the substrate was detected. Because of the thickness of the samples, the beam can pass through the film and detect the substrate.

For the  $TiO_2$  doped with silver samples a peak at 80  $cm^{-1}$  were detected and correspond to metallic Ag [3, 4]. The films elaborated by spin coating present higher intensity in comparison with the films elaborated by dip coating. It could be due to many factors, like thickness, roughness, a surface cover area among others. However, exists another factor that can affect the signal of the spectra as the focus made with a microscope in the equipment.

The doped films show a low shift in the main peak of anatase at 144  $cm^{-1}$ , in similar way as already observed in powders.

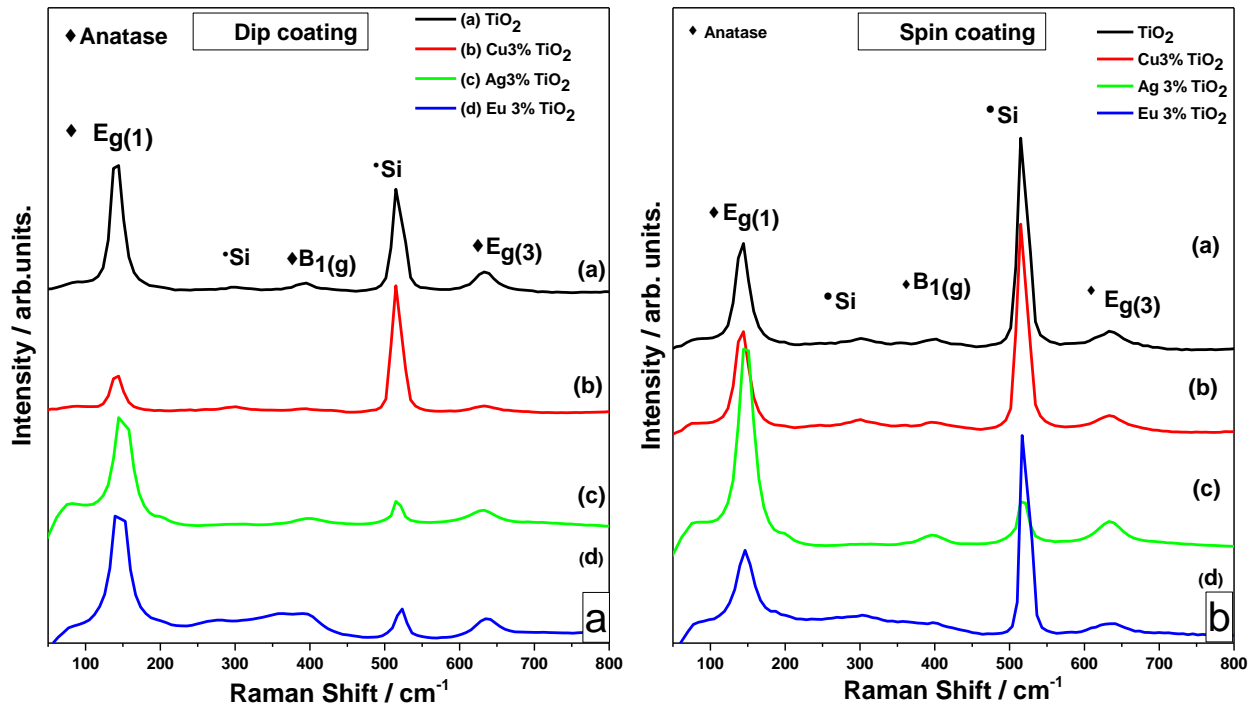


Fig. 47. Raman spectra of  $TiO_2$  pure and doped (Cu, Ag, and Eu) elaborated by a) dip coating and b) spin coating, annealed at 450  $^{\circ}C$ .

### 3.6 Morphological analysis of $TiO_2:M$ films elaborated by dip coating and spin coating.

The morphological analysis was done by AFM analysis. Information as thickness and morphology were obtained.

In the Fig. 48 and Fig. 50 can show the topographic images from the films elaborated with spin and dip coating respectively. It can be observed that even when it was employed the same solution the morphology obtained was different due to the experimental conditions used for each technique.

It is important to mention that each film was synthesized by superposition of three deposition run. This procedure allow to obtain an increasing of the thickness and roughness of the surface area. Therefore the contact surfaces increase between the film and the dye in the photocatalysis test.

Table 21. Thickness measurement by AFM of the films elaborated by spin coating and dip coating.

Sample	Thickness (spin coating) / nm	Espesor (dip coating) / nm
$TiO_2$	130	1000
3%Cu- $TiO_2$	800	500
3%Ag- $TiO_2$	1100	400
3%Eu- $TiO_2$	1140	400

Accordance to the literature, it was observed that the addition of dopant elements in the solution increase the contact angle between the solution and the substrate, this information is important for the interpretation of the obtained results. [5, 6]. A low contact angle means that the strong adhesion between the solution and the substrate is predominant, on the other hand, a high contact angle means that the cohesion forces in the solution are stronger, so it is more difficult the adhesion with the substrate.

The morphology obtained by spin coating is the result of the centripetal force combined with the surface tension of the solution which pushes the solution for creating films uniformly, see Fig. 48. The horizontal design of this technique can elaborate uniform films and besides a higher thickness in comparison with the films elaborated by dip coating, according to Table 21.

### Spin Coating

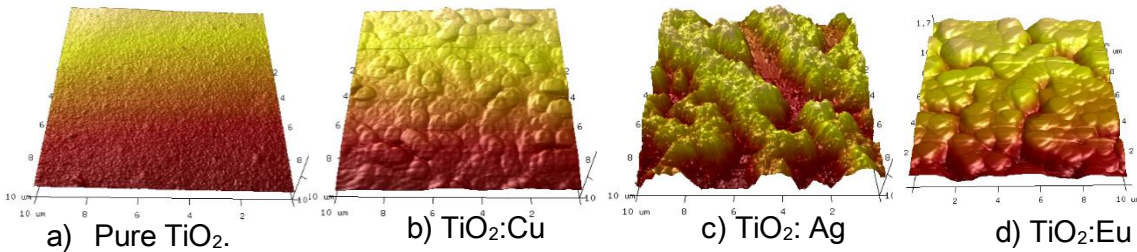


Fig. 48. AFM morphology of  $TiO_2$  film elaborated by spin coating, ( $10\ \mu m \times 10\ \mu m$ ): a) Pure  $TiO_2$ , b)  $TiO_2:Cu$  3% mol, c)  $TiO_2:Ag$  3% mol and d)  $TiO_2:Eu$ .

It can be observed that the film of pure  $TiO_2$  has a lower thickness than the doping films for the samples elaborated by spin coating. It is due to the low contact angle for the film of pure  $TiO_2$ , favoring the formation of a homogeneous flat film, see Fig. 49 a). The  $TiO_2$  doped films present higher roughness and thickness in comparison with the pure  $TiO_2$ ; it means that the contact angle of the solution increase forming a heterogeneous film, Fig. 49 b).

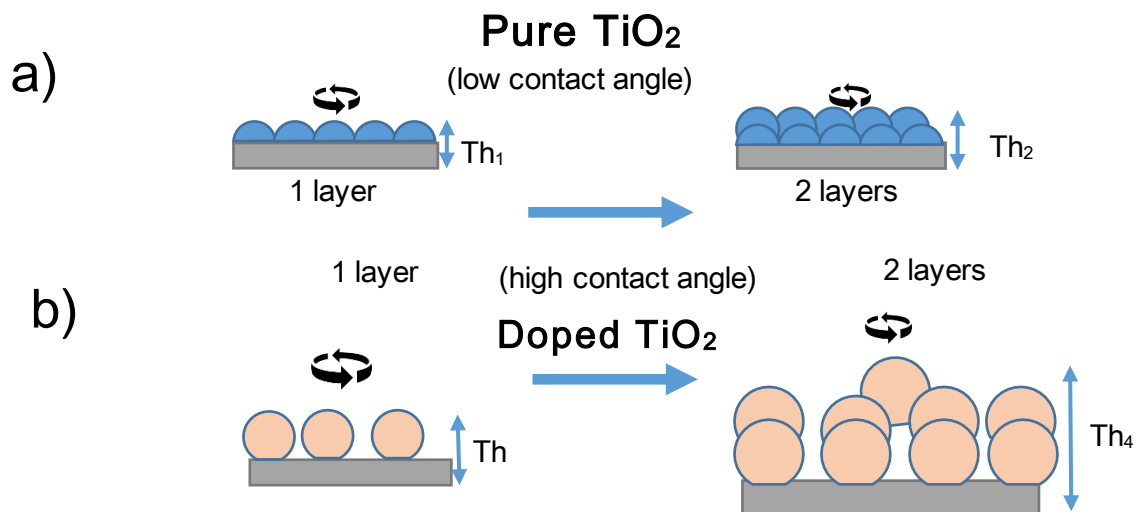


Fig. 49. Doping effect in the contact angle for films elaborated by spin coating: a) Pure  $TiO_2$  and b) Doped  $TiO_2$ .

The films elaborated by spin coating have a morphology, which depends on the factor as the withdrawn speed. This factor can change the thickness of the sample. During this process, the solution naturally and homogeneously is in contact with the substrate surface by the combined effect of the viscosity and capillarity.

### Dip Coating.

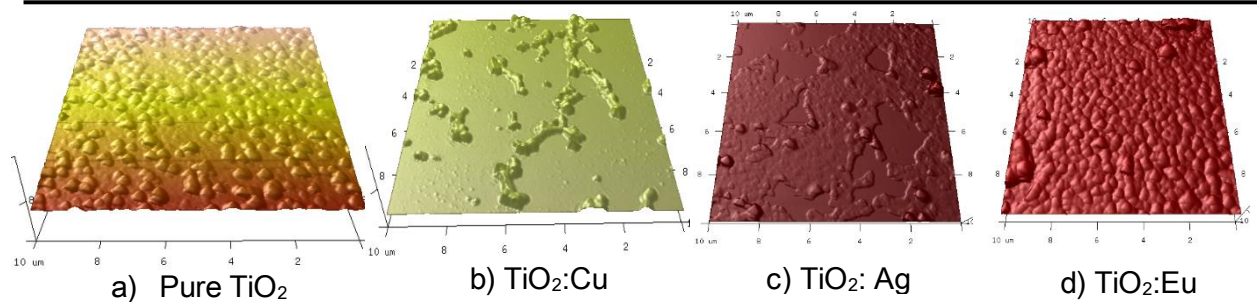


Fig. 50. AFM morphology of  $TiO_2$  film elaborated by dip coating ( $10\ \mu m \times 10\ \mu m$ ): a) Pure  $TiO_2$ , b)  $TiO_2:Cu$  3% mol, c)  $TiO_2:Ag$  3% mol and d)  $TiO_2:Eu$ .

For the sample of pure  $TiO_2$  elaborated by dip coating has a homogeneous film with a thickness higher than the doped films. This is because of the good adhesion with the substrate increasing their capillarity properties. The adhesion of new layer was done successfully Fig. 50 a) and Fig. 51 a).

For the samples of  $TiO_2:M$  the semiconductor doesn't cover all the substrate area. The particle disaggregation is more likely to form as the thickness of the  $TiO_2$  films increase. The over increasing thickness of  $TiO_2$  films caused a supersaturation of the glass support by the powder, which leads to decreasing the electrostatic attraction between the two surfaces of  $TiO_2$  particles and the support, hence a weakness of the adhesion between them. See Fig. 51 b) [7].

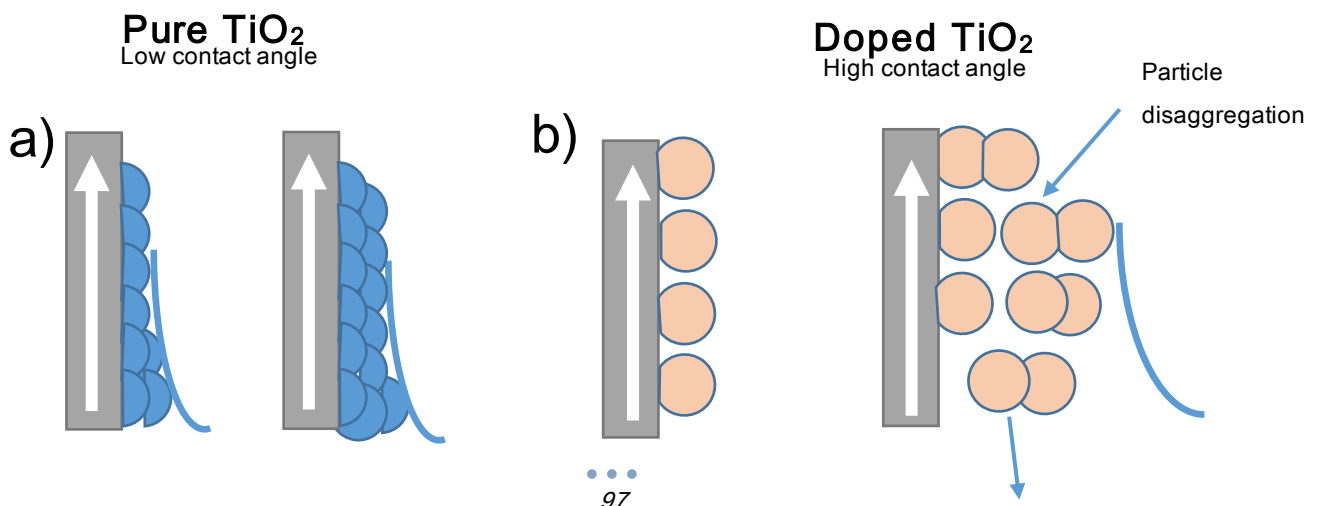


Fig. 51. Doping effect in the contact angle for films elaborated by spin coating: a) Pure  $TiO_2$  and b) Doped  $TiO_2$ .

### 3.7 Optical characterization of TiO<sub>2</sub>:M films elaborated by spin coating and dip coating.

The optical properties of the films were evaluated by measurements of their optical transmittance. The investigated films were deposited on borosilicate glass.

The band gap was determined using the Tauc plot

$$\alpha = \frac{1}{d} \ln \frac{100}{T} \quad \text{Equation 17}$$

Indeed, in amorphous materials, the absorption due to the band-to-band transitions that determine the optical band gap,  $E_g$ , is given by:

$$(\alpha h\nu) = q(h\nu - E_g)^\gamma \quad \text{Equation 18}$$

where  $E_g$  is the optical band gap,  $q$  is a constant, and  $\gamma = 0.5$  or  $2$  for indirect and direct optical transitions, respectively [8].

It can be observed that for the films elaborated by dip coating the transmittance in the visible region is higher in comparison with the films elaborated by spin coating. It could be due the low thickness and low surface area which allows to the visible light pass crossing through the film. TiO<sub>2</sub> particles, which may cause a decrease in the number of surface active sites and an increase in the opacity and the light scattering of TiO<sub>2</sub> particles more likely to decrease the passage of radiation through the sample [7].

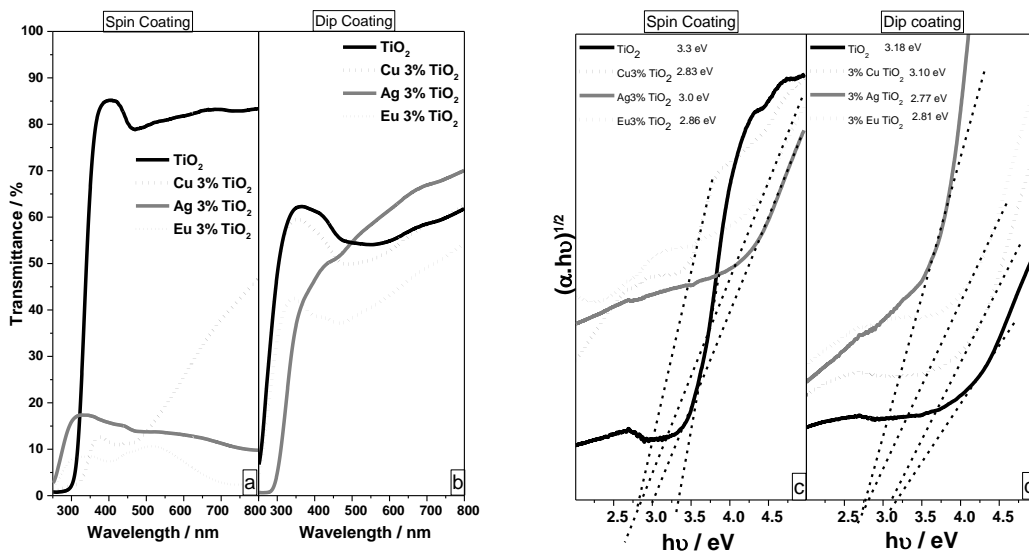


Fig. 52. Optical characterization of  $\text{M-TiO}_2$  films. Transmittance spectra and band gap determination of a) and c) respectively of  $\text{M-TiO}_2$  films elaborated by spin coating. Transmittance spectra and band gap determination of b) and d) respectively of  $\text{M-TiO}_2$  films elaborated by dip coating.

### 3.8 Photocatalytic evaluation of $\text{TiO}_2\text{:M}$ films.

The photodegradation of the dye (methylene blue  $2 \times 10^{-5}$  Mol) by pure  $\text{TiO}_2$  annealed at  $500^\circ\text{C}$  when were irradiated with light from a Xenon lamp was studied. The irradiation power was from  $320\text{ mW/cm}^2$  and a distance of 35 cm between the lamp and the sample. A magnetic stirring was used during the test.

During the test, the absorbance of the methylene blue was measured with a VIS spectrometer in intervals of 10 minutes. The Fig. 53 and Fig. 54 shows the methylene blue optical absorbance spectra for the films of pure  $\text{TiO}_2$  and  $\text{TiO}_2\text{:M}$  elaborated by spin coating and dip coating respectively. These spectra were integrated for the area under a curve measurements.

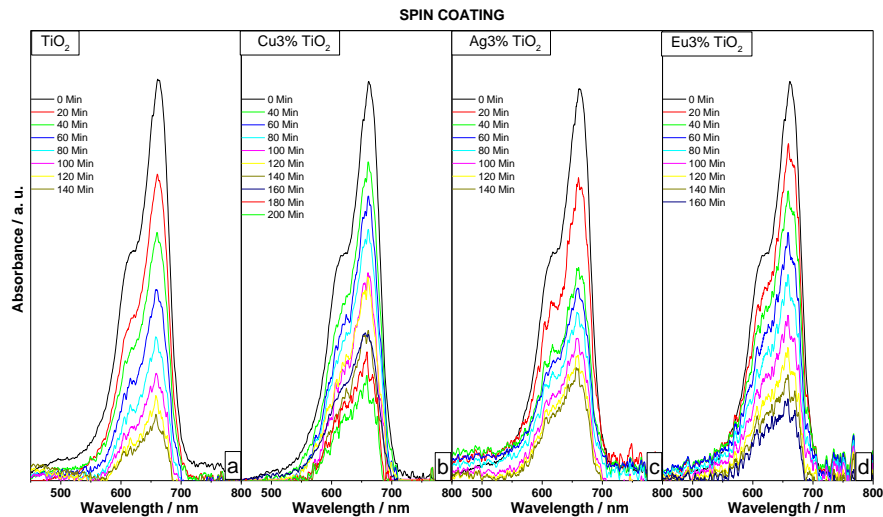


Fig. 53. Absorbance spectra of the methylene blue by the photodegradation with  $\text{M-TiO}_2$  films elaborated by spin coating.

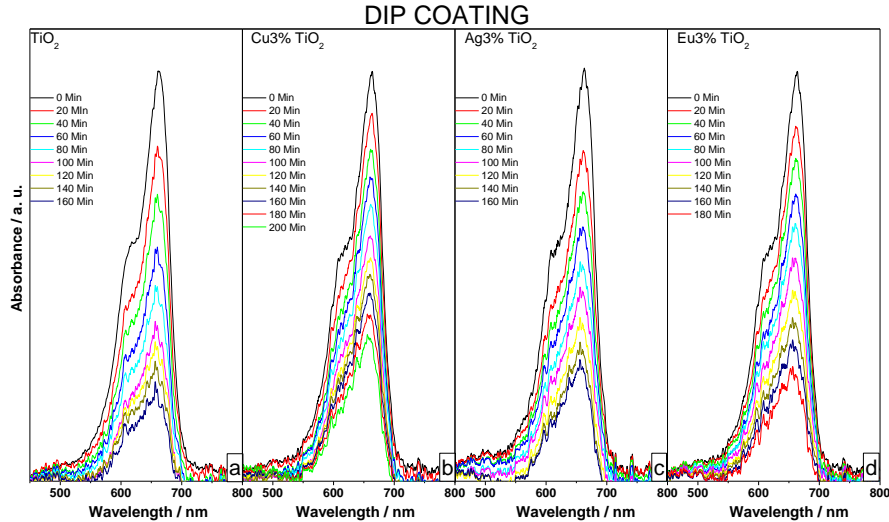


Fig. 54. Absorbance spectra of the methylene blue by the photodegradation with M-TiO<sub>2</sub> films elaborated by dip coating.

The photocatalytic process consists in the concentration reduction (C) during a time (t), following a first order Kinect employing the equation:

$$C(t) = C(0) \exp[-kt]$$

Equation 19

The most important parameter of this equation is (k), named as constant rate or constant of reaction with units of  $\text{min}^{-1}$ , Fig. 55. When this factor is higher means that the semiconductor is more efficient in the photodegradation of methylene blue.

All the photocatalysis experiments were done under the same conditions for a real comparison.

It can be observed that for the films of  $TiO_2$  doped with metallic ions ( $TiO_2:M$ ) have a constant rate lower than pure  $TiO_2$ . It means the photodegradation of the methylene blue is lower in comparison with the pure  $TiO_2$ . These results are in accordance with the obtained by the powders in Chapter 2.

In the specific case of the film of Ag- $TiO_2$  possesses a photodegradation efficiency lower than pure  $TiO_2$ . This result is not the same as the obtained by the powders in Chapter 2. It could be due the time and temperature of the thermal treatment previously mentioned during the drying and calcination process. In these conditions, the elimination of liquids and organic substance and the crystallization of anatase phase, the uniformly dispersed  $Ag^+$  ions would gradually migrate from

the volume of anatase grains to the surface and further to the surface of the  $\text{TiO}_2$  powder under the action of heat. Therefore silver could not be on the surface of the  $\text{TiO}_2$  as in the system powders, reducing the electronic charge transfer between the  $\text{TiO}_2$  and the silver nanoparticle [9].

In the case of the films doped with Europium, even when its photocatalytic efficiency is lower than pure  $\text{TiO}_2$ , its efficiency is similar than the obtained by the films doped with silver. It could be due to the temperature and the thermal treatment was lower in powders than the films, avoiding the formation of secondary compounds as  $\text{Eu}_2\text{Ti}_2\text{O}_7$ , which decrease the photocatalytic efficiency [10].

For the films elaborated by spin coating they show more photocatalytic efficiency than the films elaborated by dip coating. The possible origin is that the films elaborated by spin coating have more roughness and percentage of the cover area according to the AFM analysis. The photocatalytic efficiency is strongly influenced by the semiconductor concentration. These properties improve the contact between the semiconductor and the dyes favoring the degradation reactions.

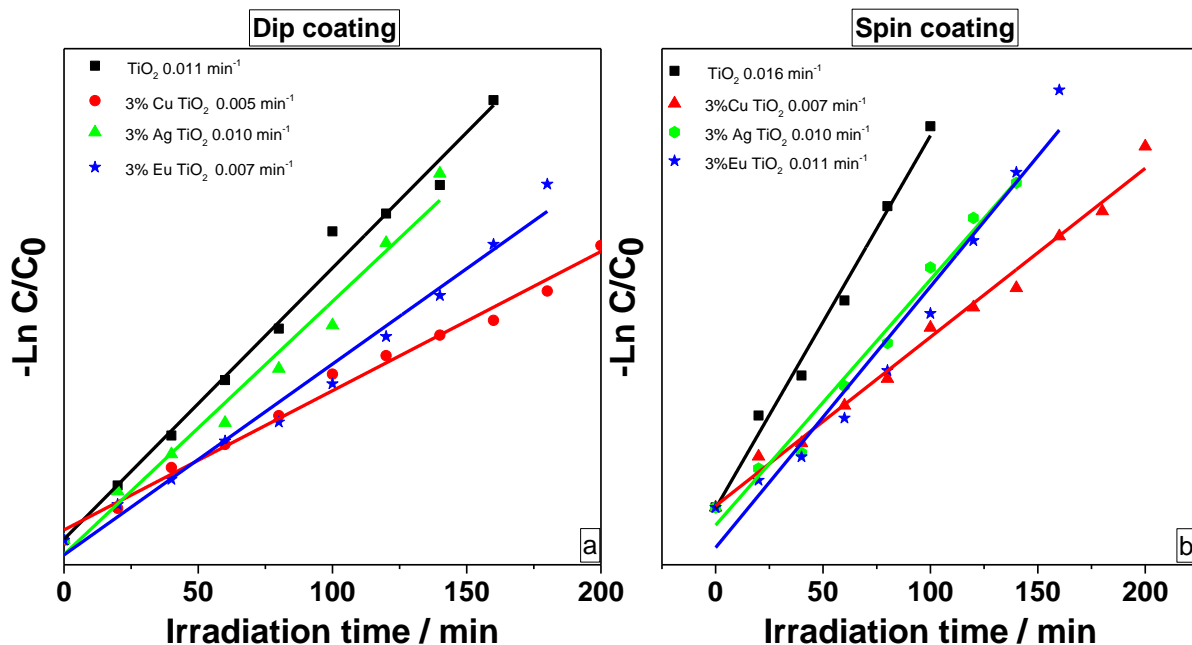


Fig. 55. First order Kinetics of methylene blue photodegradation with  $\text{M-TiO}_2$  films elaborated by a) dip coating and b) spin coating.



### 3.9 Conclusions

The film morphology obtained by the two techniques were completely different. The films elaborated by spin coating show higher photocatalytic degradation, due to the higher thickness, roughness, and percentage of covered area. These properties are obtained due to the centripetal force combined with the surface tension of the solution which pushes the solution for creating films uniform.

The films elaborated by dip coating have a low percentage of covered area. It could be due to the effect of the high contact angle, which indicates strong cohesion force in solution and then difficult adhesion with the substrate. Another important factor is the concentrations of acetic acid, which for which the vapor can dilute the formed film when it is withdrawing from the solution.

### 3.10 Bibliography.

1. Eufinger, K., D. Poelman, H. Poelman, R. De Gryse, and G. Marin, *TiO<sub>2</sub> thin films for photocatalytic applications*. Thin solid films: process and applications, 2008. **37**(661): p. 2.
2. Berti, D. and G. Palazzo, *Colloidal Foundations of Nanoscience*. 2014: Newnes.
3. Quiñones-Jurado, Z.V., M.Á. Waldo-Mendoza, H.M. Aguilera-Bandin, E.G. Villabona-Leal, E. Cervantes-González, and E. Pérez, *Silver nanoparticles supported on TiO<sub>2</sub> and their antibacterial properties: effect of surface confinement and nonexistence of plasmon resonance*. Materials Sciences and Applications, 2014. **5**(12): p. 895.
4. Bosnick, K.A., *Raman studies of mass-selected metal clusters*. 2000, University of Toronto.
5. Xu, Y., J.-a. Li, L.-f. Yao, L.-h. Li, P. Yang, and N. Huang, *Preparation and characterization of Cu-doped TiO<sub>2</sub> thin films and effects on platelet adhesion*. Surface and Coatings Technology, 2015. **261**: p. 436-441.
6. Léonard, G.L.M., C.M. Malengreaux, Q. Mélotte, S.D. Lambert, E. Bruneel, I. Van Driessche, and B. Heinrichs, *Doped sol-gel films vs. powders TiO<sub>2</sub>: On the positive effect induced by the presence of a substrate*. Journal of Environmental Chemical Engineering, 2016. **4**(1): p. 449-459.
7. Bouarioua, A. and M. Zerdaoui, *Photocatalytic activities of TiO<sub>2</sub> layers immobilized on glass substrates by dip-coating technique towards the decolorization of methyl orange as a model organic pollutant*. Journal of Environmental Chemical Engineering.
8. Salem, A. and M.S. Selim, *Structure and optical properties of chemically deposited Sb<sub>2</sub>S<sub>3</sub> thin films*. Journal of Physics D: Applied Physics, 2001. **34**(1): p. 12.
9. Chao, H.E., Y.U. Yun, H.U. Xingfang, and A. Larbot, *Effect of silver doping on the phase transformation and grain growth of sol-gel titania powder*. Journal of the European Ceramic Society, 2003. **23**(9): p. 1457-1464.
10. Zhang, Y., H. Zhang, Y. Xu, and Y. Wang, *Europium doped nanocrystalline titanium dioxide: preparation, phase transformation and photocatalytic properties*. Journal of Materials Chemistry, 2003. **13**(9): p. 2261-2265.



# CHAPTER IV

## TiO<sub>2</sub> Nanotubes



### IV. TiO<sub>2</sub> nanotubes for photocatalysis applications.

#### 4. Introduction.

The fabrication of titania nanotubes by hydrothermal synthesis is performed by reacting titania nanopowders with an alkaline aqueous solution. While the hydrothermal method of titania nanotube production has been comprehensively investigated in the past decade, the formation mechanisms, compositions, crystalline structures, thermal stabilities, and post-treatment functions remain areas of debate [1].

As a low-temperature technology, hydrothermal synthesis is environmentally friendly in that the reaction takes place in aqueous solutions within a closed system, using water as the reaction medium. This technique is usually carried out in an autoclave (a steel pressure vessel) under controlled temperature and pressure. The operating temperature is held above the water boiling point to self-generate saturated vapor pressure. The internal pressure generated in the autoclave is governed by the operating temperature and the presence of aqueous solutions in the autoclave. TiO<sub>2</sub> nanotubes are obtained when TiO<sub>2</sub> powders are mixed with 2.5-20 M sodium hydroxide aqueous solution maintained at 20-110 °C for 20 h in the autoclave [2].

The hydrothermal method is widely applied in titania nanotubes production because of its many advantages, such as high reactivity, low energy requirement, relatively non-polluting set-up and simple control of the aqueous solution. The reaction pathway is very sensitive to the experimental conditions, such as pH, temperature and hydrothermal treatment time, but the technique achieves a high yield of titania nanotubes cheaply and in a relatively simpler manner under optimized conditions. There is three main reactions steps in the hydrothermal method: (a) generation of the alkaline titanate nanotubes; (b) substitution of alkali ions with protons; and (c) heat dehydration reactions in air. The hydrothermal method is amenable to the preparation of  $\text{TiO}_2$  nanotubes with different crystalline phases such as the anatase, brookite, monoclinic and rutile phases. [1].

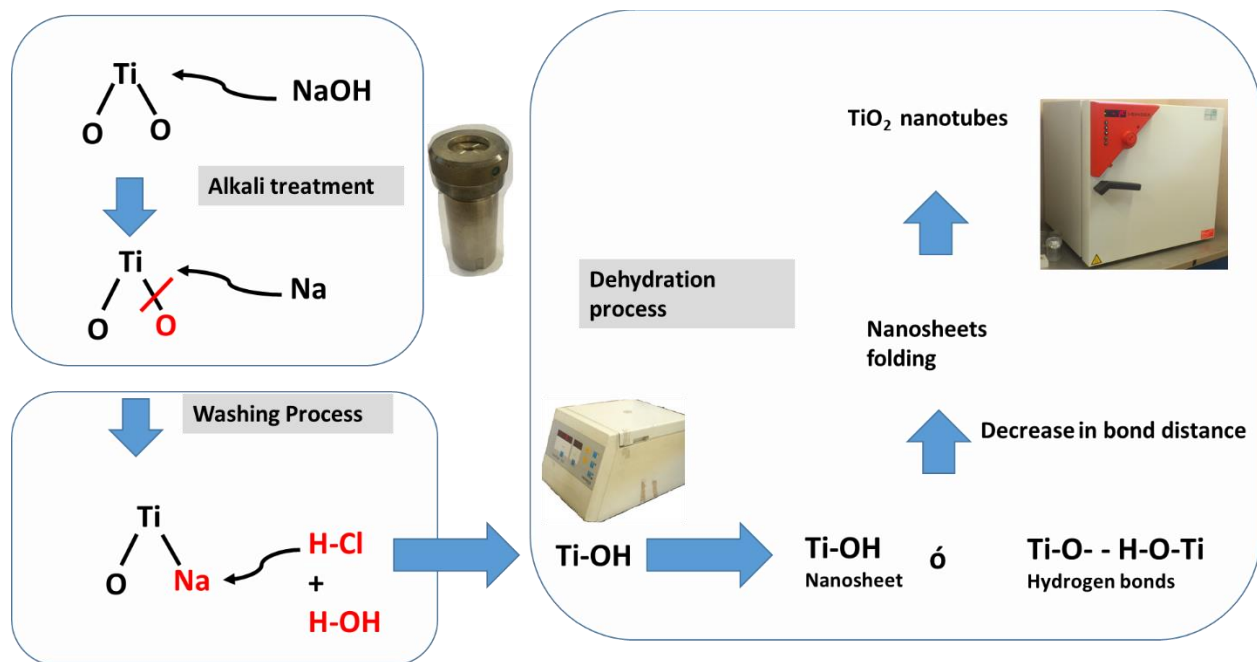


Fig. 56. Formation mechanism of  $\text{TiO}_2$  nanotubes using hydrothermal method

Kasuga and his workers subsequently introduced an acid washing treatment step following the hydrothermal process to form tri-titanate nanotubes. The purpose of the acid treatment was to remove the  $\text{Na}^+$  ions from the samples and to form new  $\text{Ti-O-Ti}$  bonds that would improve photocatalytic activity of the titania nanotubes. When the samples were treated with hydrochloric acid, the electrostatic repulsions disappeared immediately. The charged components were only gradually removed upon further washing with deionized water. The  $\text{Na}^+$  ions were displaced by  $\text{H}^+$  ions to form  $\text{Ti-OH}$  bonds in the washing process. Next, the dehydration of  $\text{Ti-OH}$  bonds produced  $\text{Ti-O-Ti}$  bonds or  $\text{Ti-O}\cdots\text{H-O-Ti}$  hydrogen bonds. The bond distance between one  $\text{Ti}$  and

another on the photocatalyst surface consequently decreased, facilitating the folding sheet process. The electrostatic repulsion from Ti-O-Na bonds enabled a joint at the ends of the sheets to form the tube structure. Kasuga et al. concluded that washing with acid and with deionized water were two principal crucial steps to produce high activity of titania nanotubes. The simple formation mechanism for titania nanotubes is shown in Fig. 56[1-3].

## 4.1 Experimental design.

Taguchi method is a very useful tool to solve the complex and confusing problems with fewest variables and fewer tests in many areas. It uses an orthogonal array to determine the effect of the variables on characteristic properties and to optimize conditions of selected variables. This statistical method was successfully utilized to optimize the preparation condition of ceramic materials which have been reported elsewhere. [4].

The Taguchi method uses orthogonal arrays to organize the parameters affecting the process and the levels at which they should be varied. It allows for the determination of factor mostly affecting a process performance characteristic with a minimum amount of experimentation [5].

Taguchi method has been employed to determine the best synthesis conditions to get TiO<sub>2</sub> nanotubes. The conditions variables studied were pressure, time, temperature and molar ratio TiO<sub>2</sub>/NaOH.

The experimental matrix is shown in Table 22 were formulated in accordant to the parameters that affect the morphology and the properties from the nanotubes during the synthesis, [6, 7].

Table 22. Parameter Level of process parameters.

		Parameters			
		Molar Ratio TiO <sub>2</sub> /NaOH	Time / hours	Temperature / °C	Pressure / bar
Levels	1	90	15	100	10
	2	70	18	110	15
	3	50	21	120	20

By the parameters and levels *used*, an L9 orthogonal array was employed and is shown in Table 23; it established 9 experiment to study the parameters effect.

Table 23. Taguchi L9 orthogonal array for TiO<sub>2</sub> nanotubes synthesis.

Experiment	Molar Ratios TiO <sub>2</sub> /NaOH	Time / hour	Temperature / °C	Pressure / bar
1	90	15	100	10
2	90	18	110	15
3	90	21	120	20
4	70	15	110	20
5	70	18	120	10
6	70	21	100	15
7	50	15	120	15
8	50	18	100	20
9	50	21	110	10

## 4.2 Synthesis of TiO<sub>2</sub> nanotubes.

### 4.2.1. Materials.

The TiO<sub>2</sub> nanotubes synthesis were made by the methodology employed for Kasuga, through a sol-gel method for TiO<sub>2</sub> nanoparticles and hydrothermal with control of pressure for TiO<sub>2</sub> nanotubes with an alkali treatment of NaOH at a temperature around the boiling point of the water.

- Titanium (IV) isopropoxide of Strem Chemicals.
- Acetic Acid.
- 2-propanol (99.5%) of Alfa Aesar GmbH.
- Triton X-100

### 4.2.2 Sol-Gel method.

The synthesis procedure for TiO<sub>2</sub> nanoparticles consisted in mixing 3.3 ml of titanium tetra isopropoxide with 5 ml of 2-propanol for 15 minutes with magnetic stirring at room temperature. Then 3.3 ml of acetic acid were added to the previous solutions and was kept it during 30 minutes for to get a very homogeneous solution.

In another recipe, 1,4 gr de Triton X-100 were mixed with 3.8 ml of 2-propanol. Both solutions were mixed and stirred until transparent solutions were obtained and then were dried at 120 °C for 12 hours and then were annealed in air at 500°C for three hours.

#### **4.2.3 Hydrothermal method.**

$\text{TiO}_2$  nanoparticles obtained by sol-gel were treated with a solution of NaOH in a time and temperature specified in the experimental design. The autoclave was pressurized with nitrogen at the pressure established in the experimental design at the beginning of the test. Subsequently, the product was washed with distilled water until reach a pH of 7. Then it was washed with 1 M of HCl. Again the product was washed with distilled water until reach a pH 7. The treated powders were separated by centrifugation. The solid was dried at 90°C and then annealed at 450°C for 30 minutes.



### 4.3 Results and discussion of TiO<sub>2</sub> nanotubes.

#### 4.3.1 Phase identification of TiO<sub>2</sub> nanotubes by X-ray Diffraction.

The TiO<sub>2</sub> powders treated by the hydrothermal method were analyzed by the X-ray diffraction for the phase analysis. The Fig. 57 shows that for the samples TG-1 to TG9 and TiO<sub>2</sub> nanoparticles have the characteristics peaks from the planes of anatase phase (JPDCS-01-089-4921). A small fraction of Brookite is presented with a peak in 30.8 grades; this peak was generated due to the presence of the surfactant Triton X-100. There is not the presence of another phase reported by other researchers, as titanates, H<sub>2</sub>Ti<sub>n</sub>O<sub>2n+1</sub>, NaOH or Na<sub>2</sub>Ti<sub>3</sub>O<sub>7</sub> among others. [6, 8, 9]. It could be due to the repetitive washing steps with HCl that can eliminate all the sodium in the systems. The post thermal treatment brings on the compositional change from H<sub>2</sub>Ti<sub>n</sub>O<sub>2n+1</sub> to TiO<sub>2</sub> [10].

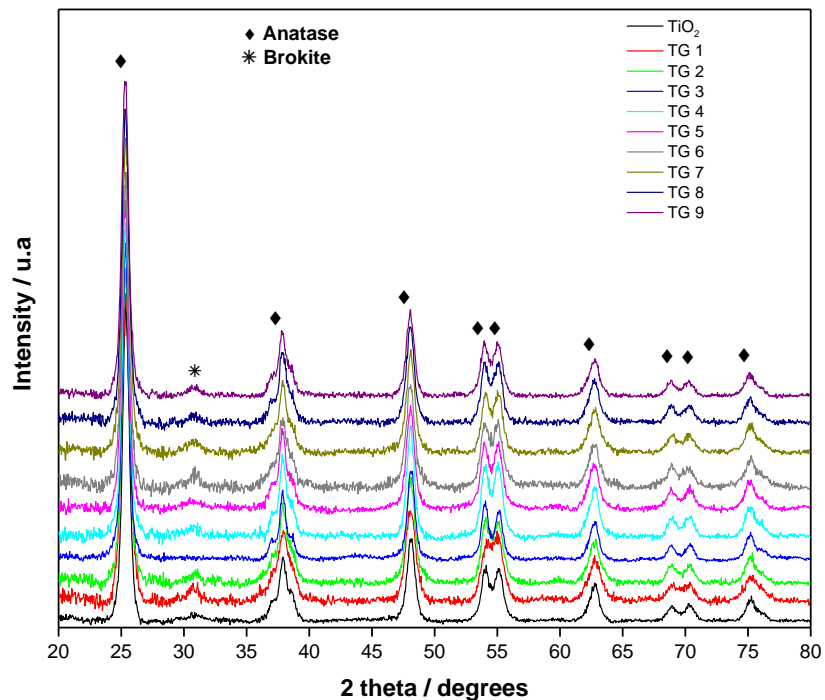


Fig. 57. X-ray diffractogram of TiO<sub>2</sub> nanotubes (TG1-TG9).

### 4.3. Phase identification of $\text{TiO}_2$ nanotubes by Raman spectroscopy.

The Raman spectroscopy was employed for the characterization of the vibration modes related to the crystalline phase of  $\text{TiO}_2$  y observe compound that could be formed during the hydrothermal process.

The Fig. 58 shows the Raman spectra of the pure  $\text{TiO}_2$  and  $\text{TiO}_2$  nanotubes, the presence of the signals at 150, 202, 404, 23, 645  $\text{cm}^{-1}$  confirm the presence of the anatase phase and there is not another peak related to a second compound.

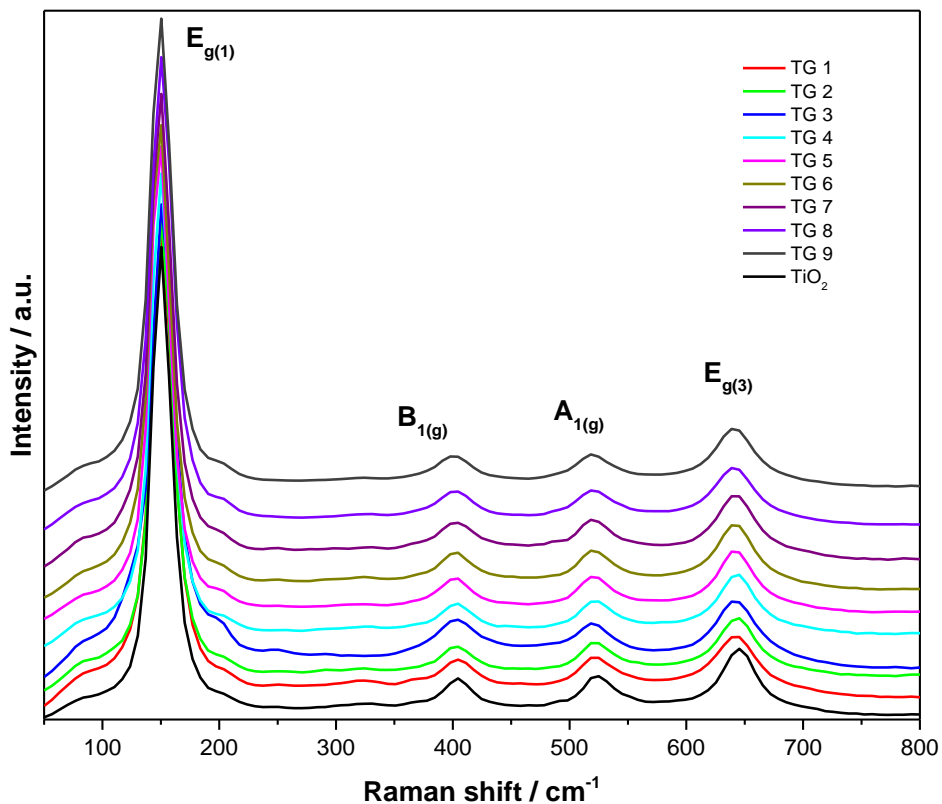


Fig. 58. Raman spectra of  $\text{TiO}_2$  nanotubes (TG1-TG9).

A nonlinear fitting of the main peak of the anatase phase ( $E_{g1}$ ), was realized using the Voigt function, to detect a shift in the Raman signal and a change in the dimensions of the Full width at half maximums (FWHM) is shown in Table 24. The peak  $E_{g1}$  is related to the symmetric vibration of O-Ti-O in the  $\text{TiO}_2$ . [11, 12]. A shift in the Raman peaks was observed for the samples from TG1 to TG9 in comparison of the pure  $\text{TiO}_2$  and a widely of the FWHM. This behavior is due to

the change in the particle size during the hydrothermal process and the presence of oxygen vacancies.

Table 24. Analysis of the main Raman peak for the anatase phase,  $E_{g1}$ .

Sample	Peak position ( $E_{g1}$ ) / cm <sup>-1</sup>	Full width at half maximum.
TiO <sub>2</sub>	150.44	20.59
TG 1	150.91	22.99
TG 2	150.98	21.49
TG 3	151.41	23.20
TG 4	150.26	21.25
TG 5	150.02	20.52
TG 6	149.33	21.37
TG 7	149.7	21.43
TG 8	150.54	22.65
TG 9	149.95	21.87

### 4.3.3 Optical analysis of TiO<sub>2</sub> nanotubes.

The diffuse reflectance spectroscopy was used to analyze the optical properties and calculate the band gap of the TiO<sub>2</sub> nanotubes.

The diffuse reflectance spectra of TiO<sub>2</sub> nanotubes has a similar behavior than TiO<sub>2</sub> nanoparticles, Fig. 59. No other peaks were observed except around 350 nm in the diffuse reflectance spectra of the TiO<sub>2</sub> systems, associated to the O<sup>2-</sup> (2p) → Ti<sup>4+</sup> (3d) charge transfer process [13].

The samples (TG1-TG9) increase their absorption in the visible region in comparison to the pure TiO<sub>2</sub>. It could be due to the presence of oxygen vacancies that can effectively extend the visible light absorption, and the band gap narrowing is closely related to the O vacancy concentrations. The oxygen vacancies were created by the hydrothermal process [14]. When the concentration of oxygen vacancies is increased, the impurity states become more delocalized and overlap with the valence band edge, resulting to the band gap narrowing [15].

Compared with the conventional doping methods, an oxygen vacancy is a kind of self-doping without introducing any impurity elements, which is more favorable for preserving the intrinsic crystal structures of the semiconductor and leads to enhanced photocatalytic performances under visible light irradiation [12, 15].

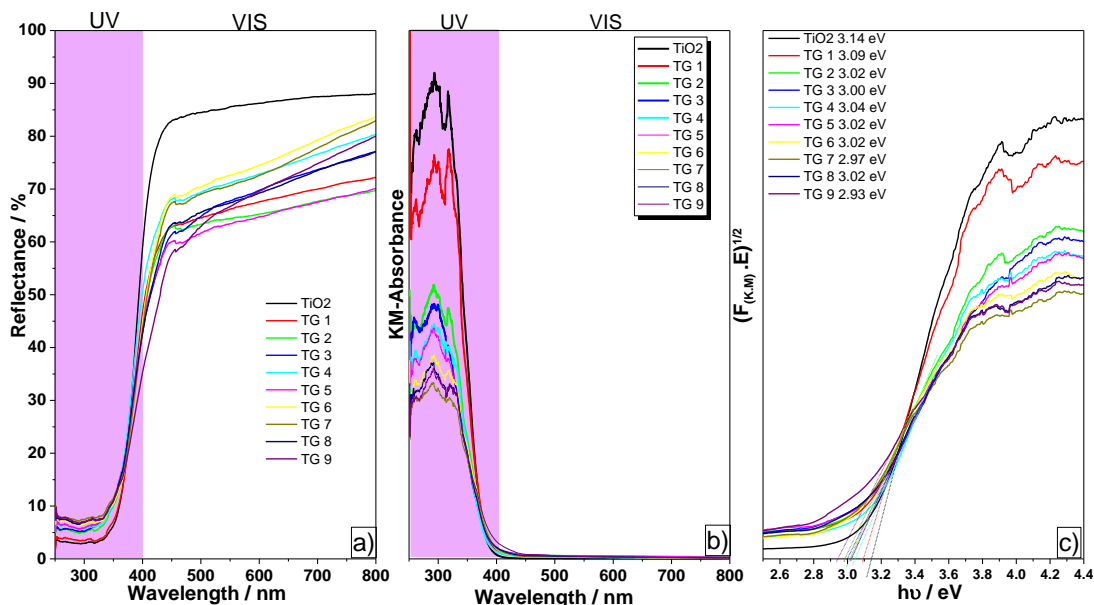


Fig. 59. Diffuse reflectance spectroscopy; a) Diffuse reflectance (%R) spectra, b) Kubelka-Munk absorption curves and determination of band gap of TiO<sub>2</sub> nanotubes.

#### 4.3.4 Morphology analysis of $\text{TiO}_2$ nanotubes.

The morphology analysis was made by Scanning electron microscopy and the Transmission electronic microscopy. The  $\text{TiO}_2$  nanoparticles synthesized by sol gel with the surfactant are shown in the Fig. 60. The surfactant was added for reducing the agglomeration of the particles. The particle size of  $\text{TiO}_2$  nanoparticles is around 20 nm.

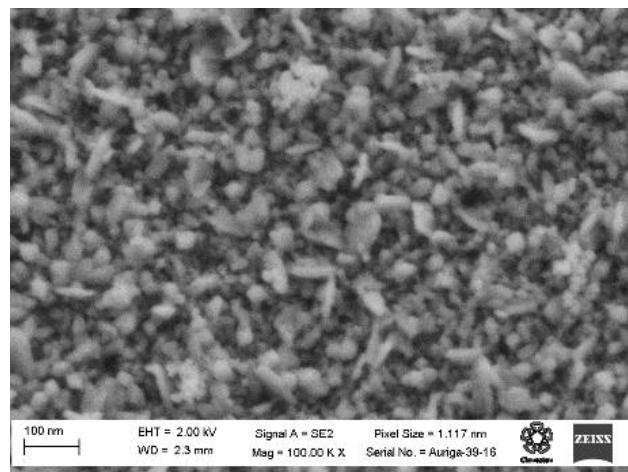


Fig. 60. SEM image of  $\text{TiO}_2$  nanoparticles annealed at  $500^\circ \text{C}$ .

The morphology of the samples treated by the hydrothermal process is shown in the Fig. 61. For the samples from TG2 to TG7 they present a morphology of one-dimensional (nanorods or nanotubes). However, THE SEM images are not able to precise the kind of morphology. For the samples TG8 and TG9 only nanoparticles were observed. For the TG1 only very dispersive nanoparticles can be observed.

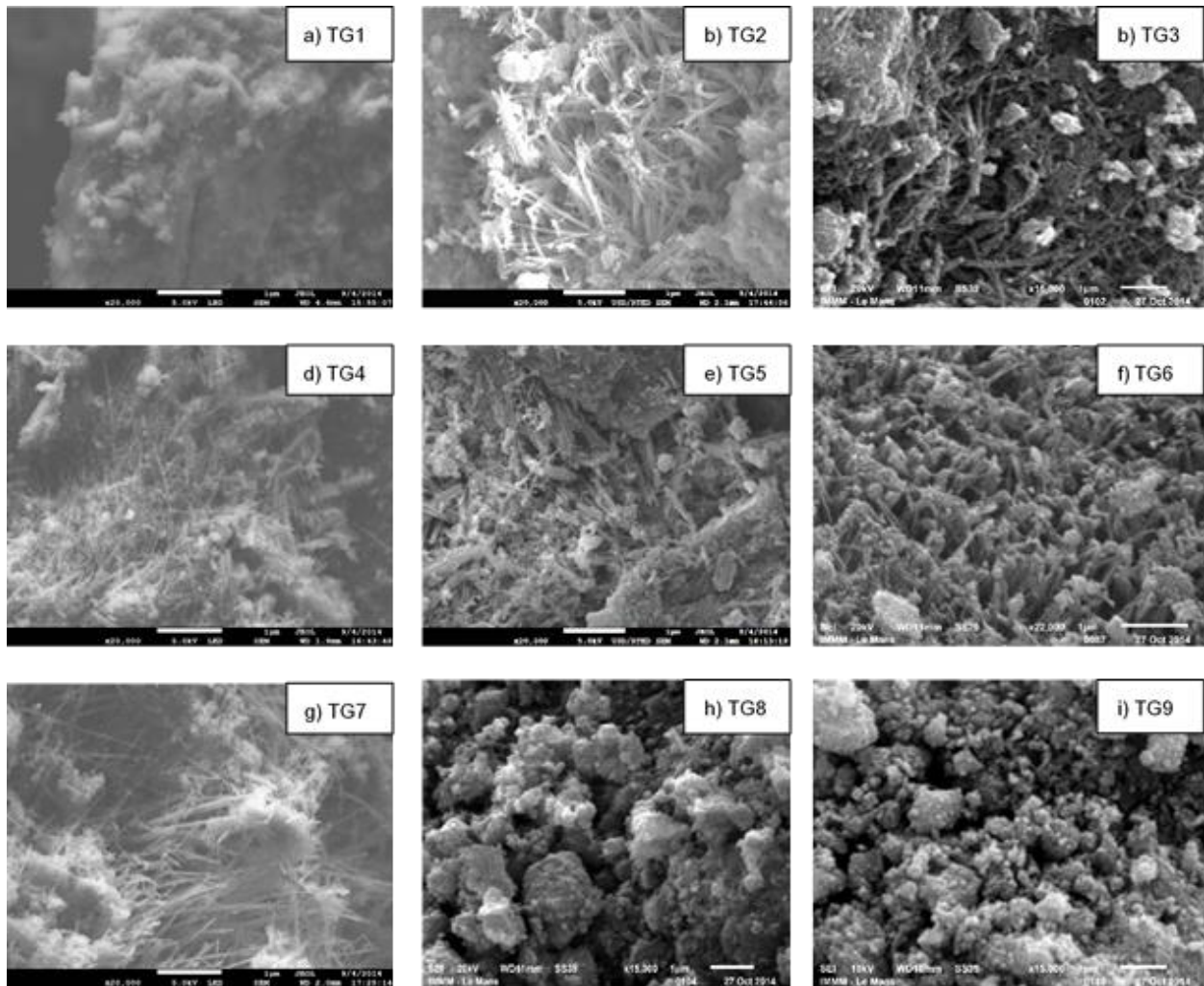


Fig. 61. SEM images of the samples treated by hydrothermal method (TG1-TG9).

The sample TG5 was analyzed by TEM to identify tubular morphology, shown in the Fig. 62. A diameter of around 20 nm can be observed; the nanotube has an open end. The length is around micrometers with a single-wall.

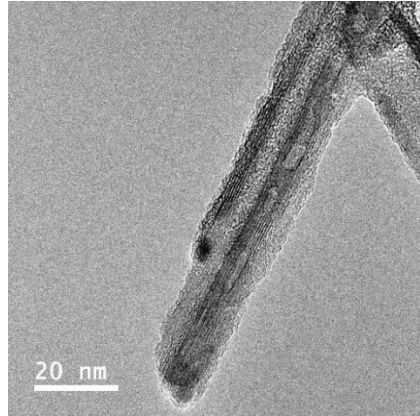


Fig. 62. TEM image of the  $TiO_2$  nanotube (TG5).

A qualitative analysis was made using the SEM images, to evaluate the percentage of nanotubes formation in the hydrothermal process.

The hydrothermal process with a controlled pressure mechanism has been barely using it; the conventional hydrothermal is the method widely used it for the obtention of  $TiO_2$  nanotubes. Due in the hydrothermal process exists many parameters to establish that is the reason for the employment of Taguchi method for to know the role of the parameter in the formation of nanotubes.

The analysis of the Taguchi method was made taking in account the formation of  $TiO_2$  nanotubes versus the parameter varied, as is shown in the Fig. 63. According to the results, the highest conditions of temperature, pressure and time promote the formation of  $TiO_2$  nanotubes. In the case of  $NaOH/TiO_2$ , the intermediate condition shows the highest value of  $TiO_2$  nanotubes formation. These results are in concordance with the obtained for others authors, employing a conventional hydrothermal method [16-18].

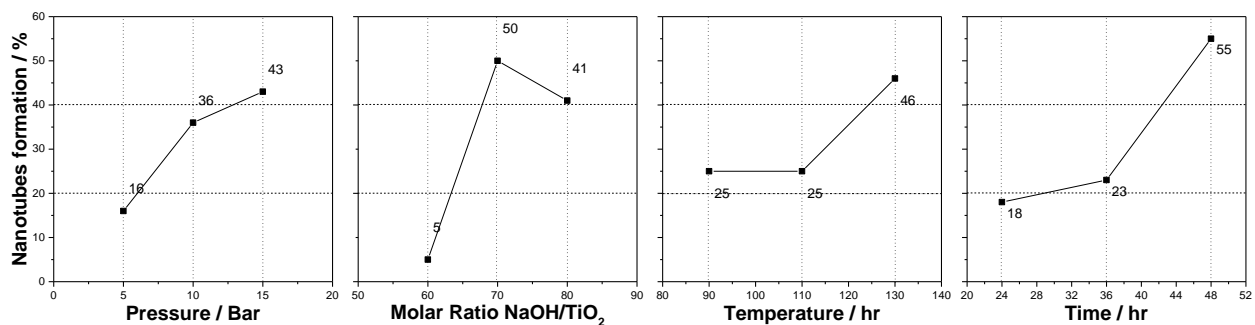


Fig. 63. Influence of design parameters on the formation of  $TiO_2$  nanotubes.

## Surface Area Determination of TiO<sub>2</sub> nanotubes by the BET method (Branauer, Emmet y Teller).

The BET surface area were determined by BET technique; the results are shown in Table 25. It is evident that the samples that were treated by the hydrothermal method have a BET surface area higher than pure TiO<sub>2</sub> synthesized by sol-gel method; even the samples with non-tubular morphology the surface area increased.

Table 25. BET results of TiO<sub>2</sub> nanotubes.

Muestra	BET Surface area / m <sup>2</sup> g <sup>-1</sup>	Pore volume / cm <sup>3</sup> g <sup>-1</sup>	Pore size / nm
TiO <sub>2</sub> a 500°C	25.24	0.09	14.4
TG 1	88.62	0.15	6.9
TG 2	83.9	0.16	7.8
TG 3	90.62	0.31	13.7
TG 4	72.93	0.23	12.9
TG 5	81.2	0.22	11.2
TG 6	80.68	0.16	8.1
TG 7	76.72	0.16	85.3
TG8	79.16	0.20	10.4
TG9	80.1	0.21	10.6



### 4.3.5 Photocatalytic degradation of methylene blue in water by TiO<sub>2</sub> nanotubes.

The methylene blue was degraded by the TiO<sub>2</sub> powder under irradiation from Xe lamp. The irradiation incident power on the samples was of 60 mW/cm<sup>2</sup>: and the distance between the lamp and the sample is 70 cm. The initial methylene blue concentration is 2x10<sup>-5</sup> Mol. During the test, a continuous magnetic stirring was done. The evolution of the optical absorption of methylene blue as from TiO<sub>2</sub> nanoparticles and TiO<sub>2</sub> nanotubes photocatalysis is illustrated in the Fig. 64 and Fig. 65 respectively. The peak integration is measured to obtain the kinetics of degradation.

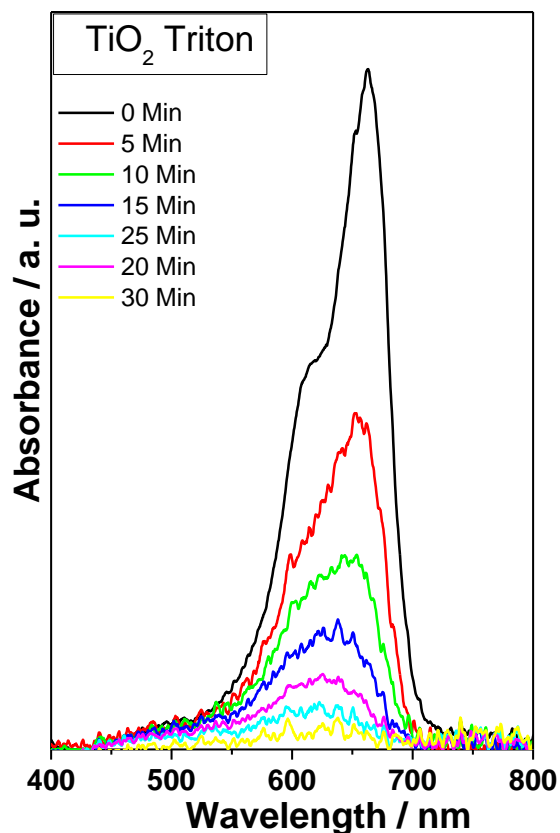


Fig. 64. Evolution of the optical absorption of methylene blue degradation by TiO<sub>2</sub> nanoparticles.

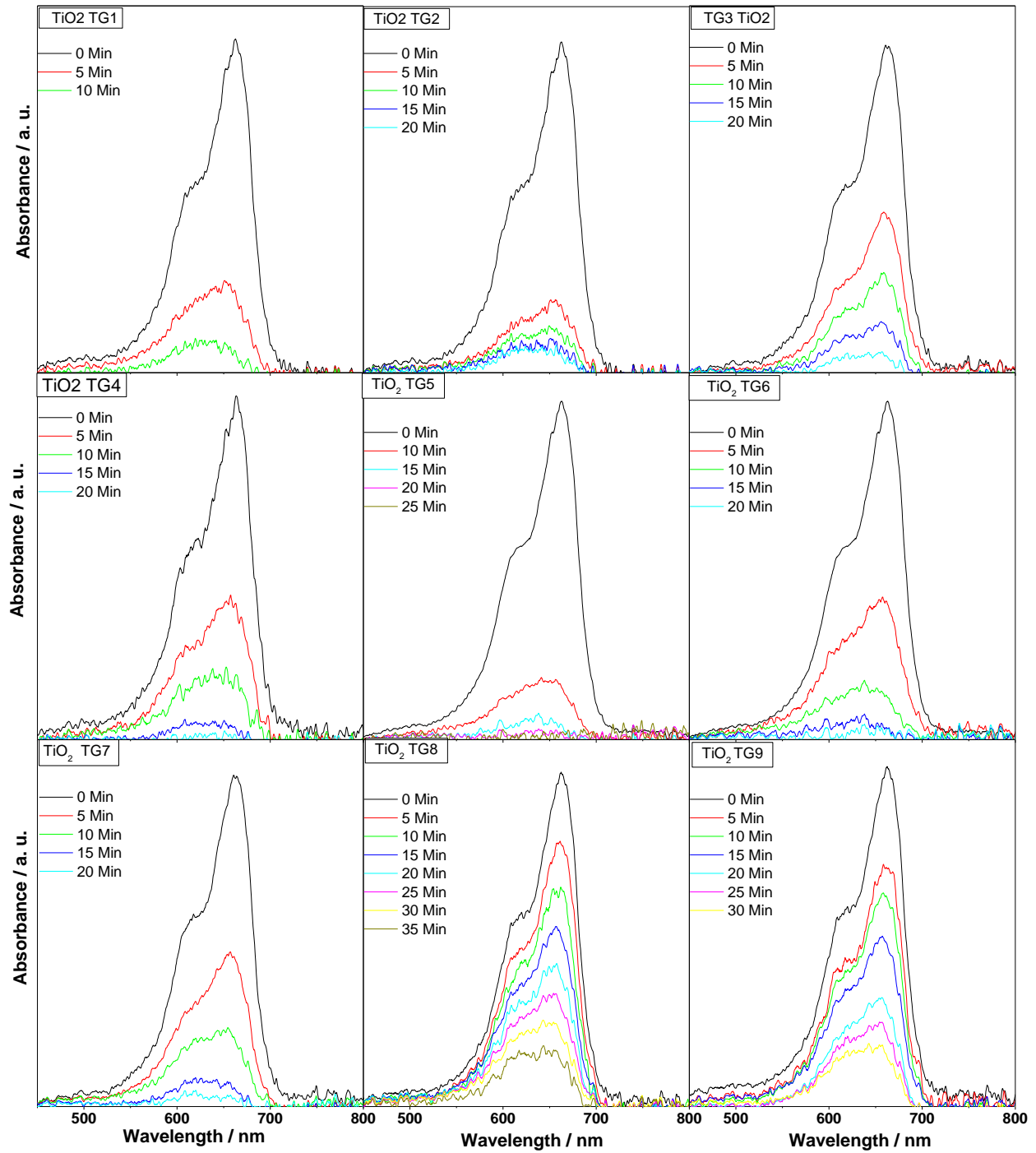


Fig. 65 Evolution of the optical absorption of methylene blue degradation by  $\text{TiO}_2$  nanotubes (TG1-TG9)

The photocatalytic efficiency is evaluated by the kinetics of degradation as is shown in the Fig. 66. It is evident that the morphology plays a very important role in the photocatalysis process. The samples with a nanotubular morphology (TG2 to TG7) have a higher constant rate in comparison with the pure TiO<sub>2</sub>. The samples TG8 and TG9 with a spherical morphology have a constant rate lower than pure TiO<sub>2</sub> even when they have a surface area similar than the samples with nanotubes; this is because the recombination rate is higher in nanoparticles than nanotubes.

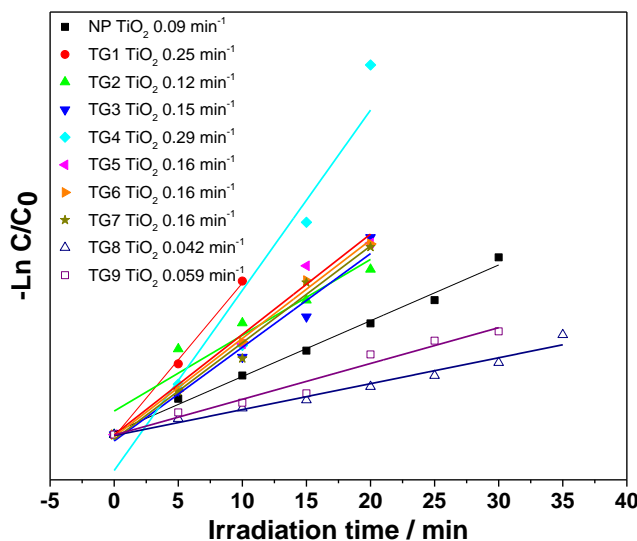


Fig. 66. Pseudo first-order kinetics of degradation of Methylene Blue solutions.

Sun et al. reported that tubular structure facilitates the electronic mobility due to the reduced grain boundaries, which is expected to improve the charge separation for photocatalytic reactions [19].

Nanotubular materials are of great interest because of their exceptional electronic and mechanical properties, high photocatalytic activity and superficial area and pore volume [20].

Compared to spherical particles, one-dimensional TiO<sub>2</sub> nanostructures could provide a high surface area and a high interfacial charge transfer rate. The carriers are free to move throughout the length of these nanostructures, which is expected to reduce the e<sup>-</sup>/h<sup>+</sup> recombination probability. Titania nanotubes have a relatively high surface area compared to non-porous titania, and time-resolved diffuse reflectance spectroscopy has shown that charge recombination is disfavored by the tubular morphology of the titania [21].

## 4.4 Conclusions.

The hydrothermal method offers an advantage as high reactivity, low energy requirements and simple control of aqua solutions in nanotubes fabrication. The Taguchi method leads to knowing the optimal parameters for nanotubes synthesis. It will be interested in consider higher intervals of parameters in a new experimental design to know the effect of the parameters in the tubular formation.

It has been shown that tubular morphology is more efficient for methylene blue degradation in comparison of TiO<sub>2</sub> nanoparticles. The presence of oxygen vacancies and the high surface area generated during the morphological change from spherical to tubular in the hydrothermal method can improve the degradation of the dye. Beside promote the decreasing of electron-hole recombination by the charge transfer trough the length of nanotubes.

Finally it is important to mention that tubular morphology is better photocatalyst in comparison with TiO<sub>2</sub> doped with silver.

## 4.5 Bibliography.

1. Wong, C.L., Y.N. Tan, and A.R. Mohamed, *A review on the formation of titania nanotube photocatalysts by hydrothermal treatment*. J Environ Manage, 2011. **92**(7): p. 1669-80.
2. Chen, X. and S.S. Mao, *Titanium dioxide nanomaterials: synthesis, properties, modifications, and applications*. Chem Rev, 2007. **107**(7): p. 2891-959.
3. Kasuga, T., M. Hiramatsu, A. Hoson, T. Sekino, and K. Niihara, *Titania nanotubes prepared by chemical processing*. Advanced Materials, 1999. **11**(15): p. 1307-1311.
4. Naghibi, S., M.A. Faghihi Sani, and H.R. Madaah Hosseini, *Application of the statistical Taguchi method to optimize TiO<sub>2</sub> nanoparticles synthesis by the hydrothermal assisted sol-gel technique*. Ceramics International, 2014. **40**(3): p. 4193-4201.
5. Jeng, M.-J., Y.-L. Wung, L.-B. Chang, and L. Chow, *Dye-Sensitized Solar Cells with Anatase TiO<sub>2</sub> Nanorods Prepared by Hydrothermal Method*. International Journal of Photoenergy, 2013. **2013**: p. 8.
6. Bavykin, D.V., V.N. Parmon, A.A. Lapkin, and F.C. Walsh, *The effect of hydrothermal conditions on the mesoporous structure of TiO<sub>2</sub> nanotubes*. Journal of Materials Chemistry, 2004. **14**(22): p. 3370-3377.
7. Sreekantan, S. and L.C. Wei, *Study on the formation and photocatalytic activity of titanate nanotubes synthesized via hydrothermal method*. Journal of Alloys and Compounds, 2010. **490**(1-2): p. 436-442.
8. Yuan, Z.-Y. and B.-L. Su, *Titanium oxide nanotubes, nanofibers and nanowires*. Colloids and Surfaces A: Physicochemical and Engineering Aspects, 2004. **241**(1-3): p. 173-183.
9. Ribbens, S., V. Meynen, G. Van Tendeloo, X. Ke, M. Mertens, B. Maes, P. Cool, and E. Vansant, *Development of photocatalytic efficient Ti-based nanotubes and nanoribbons by conventional and microwave assisted synthesis strategies*. Microporous and Mesoporous Materials, 2008. **114**(1): p. 401-409.
10. Weng, L.Q., S.H. Song, S. Hodgson, A. Baker, and J. Yu, *Synthesis and characterisation of nanotubular titanates and titania*. Journal of the European Ceramic Society, 2006. **26**(8): p. 1405-1409.
11. Ohsaka, T., F. Izumi, and Y. Fujiki, *Raman spectrum of anatase, TiO<sub>2</sub>*. Journal of Raman spectroscopy, 1978. **7**(6): p. 321-324.
12. Choudhury, B., M. Dey, and A. Choudhury, *Defect generation, dd transition, and band gap reduction in Cu-doped TiO<sub>2</sub> nanoparticles*. International Nano Letters, 2013. **3**(1): p. 1-8.
13. Colón, G., M. Maicu, M.C. Hidalgo, and J.A. Navío, *Cu-doped TiO<sub>2</sub> systems with improved photocatalytic activity*. Applied Catalysis B: Environmental, 2006. **67**(1-2): p. 41-51.
14. Coronado, J.M., F. Fresno, M.D. Hernández-Alonso, and R. Portela, *Design of advanced photocatalytic materials for energy and environmental applications*. 2013: Springer.
15. Wang, J., Z. Wang, B. Huang, Y. Ma, Y. Liu, X. Qin, X. Zhang, and Y. Dai, *Oxygen vacancy induced band-gap narrowing and enhanced visible light photocatalytic activity of ZnO*. ACS applied materials & interfaces, 2012. **4**(8): p. 4024-4030.
16. Yuan, Z.-Y. and B.-L. Su, *Titanium oxide nanotubes, nanofibers and nanowires*. Colloids and Surfaces A: Physicochemical and Engineering Aspects, 2004. **241**(1): p. 173-183.
17. Poudel, B., W.Z. Wang, C. Dames, J.Y. Huang, S. Kunwar, D.Z. Wang, D. Banerjee, G. Chen, and Z.F. Ren, *Formation of crystallized titania nanotubes and their transformation into nanowires*. Nanotechnology, 2005. **16**(9): p. 1935.

18. Ma, Y., Y. Lin, X. Xiao, X. Zhou, and X. Li, *Sonication–hydrothermal combination technique for the synthesis of titanate nanotubes from commercially available precursors*. Materials Research Bulletin, 2006. **41**(2): p. 237-243.
  19. Sun, Y., G. Wang, and K. Yan, *TiO<sub>2</sub> nanotubes for hydrogen generation by photocatalytic water splitting in a two-compartment photoelectrochemical cell*. International Journal of Hydrogen Energy, 2011. **36**(24): p. 15502-15508.
  20. Idakiev, V., Z.-Y. Yuan, T. Tabakova, and B.-L. Su, *Titanium oxide nanotubes as supports of nano-sized gold catalysts for low temperature water-gas shift reaction*. Applied Catalysis A: General, 2005. **281**(1): p. 149-155.
  21. Colmenares, J.C., R. Luque, J.M. Campelo, F. Colmenares, Z. Karpiński, and A.A. Romero, *Nanostructured photocatalysts and their applications in the photocatalytic transformation of lignocellulosic biomass: an overview*. Materials, 2009. **2**(4): p. 2228-2258.
- 
1. Wong, C.L., Y.N. Tan, and A.R. Mohamed, *A review on the formation of titania nanotube photocatalysts by hydrothermal treatment*. J Environ Manage, 2011. **92**(7): p. 1669-80.
  2. Chen, X. and S.S. Mao, *Titanium dioxide nanomaterials: synthesis, properties, modifications, and applications*. Chem Rev, 2007. **107**(7): p. 2891-959.
  3. Kasuga, T., M. Hiramatsu, A. Hoson, T. Sekino, and K. Niihara, *Titania nanotubes prepared by chemical processing*. Advanced Materials, 1999. **11**(15): p. 1307-1311.
  4. Naghibi, S., M.A. Faghihi Sani, and H.R. Madaah Hosseini, *Application of the statistical Taguchi method to optimize TiO<sub>2</sub> nanoparticles synthesis by the hydrothermal assisted sol–gel technique*. Ceramics International, 2014. **40**(3): p. 4193-4201.
  5. Jeng, M.-J., Y.-L. Wung, L.-B. Chang, and L. Chow, *Dye-Sensitized Solar Cells with Anatase TiO<sub>2</sub> Nanorods Prepared by Hydrothermal Method*. International Journal of Photoenergy, 2013. **2013**: p. 8.
  6. Bavykin, D.V., V.N. Parmon, A.A. Lapkin, and F.C. Walsh, *The effect of hydrothermal conditions on the mesoporous structure of TiO<sub>2</sub> nanotubes*. Journal of Materials Chemistry, 2004. **14**(22): p. 3370-3377.
  7. Sreekantan, S. and L.C. Wei, *Study on the formation and photocatalytic activity of titanate nanotubes synthesized via hydrothermal method*. Journal of Alloys and Compounds, 2010. **490**(1–2): p. 436-442.
  8. Yuan, Z.-Y. and B.-L. Su, *Titanium oxide nanotubes, nanofibers and nanowires*. Colloids and Surfaces A: Physicochemical and Engineering Aspects, 2004. **241**(1–3): p. 173-183.
  9. Ribbens, S., V. Meynen, G. Van Tendeloo, X. Ke, M. Mertens, B. Maes, P. Cool, and E. Vansant, *Development of photocatalytic efficient Ti-based nanotubes and nanoribbons by conventional and microwave assisted synthesis strategies*. Microporous and Mesoporous Materials, 2008. **114**(1): p. 401-409.
  10. Weng, L.Q., S.H. Song, S. Hodgson, A. Baker, and J. Yu, *Synthesis and characterisation of nanotubular titanates and titania*. Journal of the European Ceramic Society, 2006. **26**(8): p. 1405-1409.
  11. Ohsaka, T., F. Izumi, and Y. Fujiki, *Raman spectrum of anatase, TiO<sub>2</sub>*. Journal of Raman spectroscopy, 1978. **7**(6): p. 321-324.
  12. Choudhury, B., M. Dey, and A. Choudhury, *Defect generation, dd transition, and band gap reduction in Cu-doped TiO<sub>2</sub> nanoparticles*. International Nano Letters, 2013. **3**(1): p. 1-8.

13. Colón, G., M. Maicu, M.C. Hidalgo, and J.A. Navío, *Cu-doped TiO<sub>2</sub> systems with improved photocatalytic activity*. Applied Catalysis B: Environmental, 2006. **67**(1–2): p. 41-51.
14. Coronado, J.M., F. Fresno, M.D. Hernández-Alonso, and R. Portela, *Design of advanced photocatalytic materials for energy and environmental applications*. 2013: Springer.
15. Wang, J., Z. Wang, B. Huang, Y. Ma, Y. Liu, X. Qin, X. Zhang, and Y. Dai, *Oxygen vacancy induced band-gap narrowing and enhanced visible light photocatalytic activity of ZnO*. ACS applied materials & interfaces, 2012. **4**(8): p. 4024-4030.
16. Yuan, Z.-Y. and B.-L. Su, *Titanium oxide nanotubes, nanofibers and nanowires*. Colloids and Surfaces A: Physicochemical and Engineering Aspects, 2004. **241**(1): p. 173-183.
17. Poudel, B., W.Z. Wang, C. Dames, J.Y. Huang, S. Kunwar, D.Z. Wang, D. Banerjee, G. Chen, and Z.F. Ren, *Formation of crystallized titania nanotubes and their transformation into nanowires*. Nanotechnology, 2005. **16**(9): p. 1935.
18. Ma, Y., Y. Lin, X. Xiao, X. Zhou, and X. Li, *Sonication–hydrothermal combination technique for the synthesis of titanate nanotubes from commercially available precursors*. Materials Research Bulletin, 2006. **41**(2): p. 237-243.
19. Sun, Y., G. Wang, and K. Yan, *TiO<sub>2</sub> nanotubes for hydrogen generation by photocatalytic water splitting in a two-compartment photoelectrochemical cell*. International Journal of Hydrogen Energy, 2011. **36**(24): p. 15502-15508.
20. Idakiev, V., Z.-Y. Yuan, T. Tabakova, and B.-L. Su, *Titanium oxide nanotubes as supports of nano-sized gold catalysts for low temperature water-gas shift reaction*. Applied Catalysis A: General, 2005. **281**(1): p. 149-155.
21. Colmenares, J.C., R. Luque, J.M. Campelo, F. Colmenares, Z. Karpiński, and A.A. Romero, *Nanostructured photocatalysts and their applications in the photocatalytic transformation of lignocellulosic biomass: an overview*. Materials, 2009. **2**(4): p. 2228-2258.



# V GENERAL CONCLUSIONS



## V General conclusions.

The present work pretended to study to the TiO<sub>2</sub> in two mainly paths

1. Doping with metallic ions
2. Morphological Modification

Metallic doping was employed for the increasing of the optical absorption of TiO<sub>2</sub> in the Visible region, while the morphological modification option was used to overcome the nanoparticles issues, as the effective charge transfer due to the high quantity of grain boundary.

For TiO<sub>2</sub> doping with metallic ions, the main goal was to introduce the metallic ions inside the titania lattice for keep the integrity of the crystalline structure and produce favorable changes in the electronic structure, however depending on the dopant ion nature (electronegativity and ionic radio) will be its incorporation in the system. It could be substitutional (Cu doping), as metallic segregates (Ag doping) and phases segregations (Eu doping). Besides it could be observed that the presence of dopants elements influence on the phase transformation temperature of TiO<sub>2</sub>



when it transforms from anatase to rutile. Cu and Ag decrease the phase transformation temperature, for Eu, the opposite effect was observed.

For copper doping, a substitutional incorporation was done, and it increases the visible light absorption. Cu-doped TiO<sub>2</sub> showed a lower degradation efficiency in comparison with the pure TiO<sub>2</sub>, due copper in such concentrations act as a recombination center for photoinduced electrons and holes.

For silver doping, the visible light absorption and the photocatalytic efficiency is higher than the pure TiO<sub>2</sub>, due that silver is deposited on the titania surface, and allows for negative charge accumulation promoting the photoabsorption of the O<sub>2</sub> molecules, improving the dye degradation.

For europium doping, due to the ion size, favor the electron-hole recombinations at this doping concentrations.

The morphological modification by the hydrothermal method with pressure control allows the formation of TiO<sub>2</sub> nanotubes starting form nanoparticles. An experimental design 2<sup>k-1</sup> based on the Taguchi philosophy was employed to study the effect of the parameter in the nanotubes formation and the dye degradation efficiency. The methylene blue degradations were higher for the samples submitted at high conditions as pressure, time, temperature and concentrations, due to the fact they allow the nanotubes formation in the hydrothermal process. Results are related the efficient electronic transport of the 1D structures, the high surface area and the vacancies generation in comparison with the TiO<sub>2</sub> nanoparticles.

Methylene blue degradation was higher for when TiO<sub>2</sub> nanotubes were employed in comparison with the metal doped-TiO<sub>2</sub> and pure TiO<sub>2</sub>. The morphological modification seems to be the option for increase the photocatalytic efficiency of TiO<sub>2</sub>, however, must consider the long synthesis process for its formation.

# Appendix.

## VI. Appendix

### 6.1 Synthesis methods

#### 6.1.1 Sol-Gel.

Sol-gel refers to solution-gelation and is a widely used method for producing ceramic materials with high purity and homogeneity. This approach offers control of the composition and structure at the molecular level. The process involves the generation of a colloidal suspension, which is subsequently converted to gel. In the process, reactive metal precursors are initially hydrolyzed, followed by condensation and polymerization reactions. The metal alkoxides are organometallic compounds with an organic ligand attached to a metal or metalloid atom. These alkoxides are the result of direct or indirect reactions between a metal (M) and alcohol (ROH); typical examples include methoxide (OMe;  $\text{MOCH}_3$ ) and ethoxide (OEt;  $\text{MOC}_2\text{H}_5$ ). During hydrolysis, the alkoxy groups (OR) are replaced by hydroxy ligands (OH), i.e.



where R is the alkyl group ( $\text{C}_n\text{H}_{2n+1}$ ). The mechanism of this reaction involves the addition of a negatively charged  $\text{HO}^-$  group to the positively charged metal center ( $\text{M}^{d+}$ ) followed by the removal of ROH. Several factors are known to affect the hydrolysis reaction: (a) the nature of the alkyl group, (b) the nature of the solvent, (c) the concentration of each species in the solvent, (d) temperature, (e) the water to alkoxide molar ratio, and (f) the presence of acid or base catalysts.

Subsequent condensation eliminates either water or alcohol to produce metal oxide or hydroxide linkages. In this process, the two mononuclear complexes of M, each comprising only one metal M, can react with each another to form a polynuclear complex consisting of two metal atoms. Condensation only occurs when at least one hydroxo ligand is bonded to the cation M; this is designated as M-OH for simplicity. Condensation can proceed via olation and oxolation reactions. Olation is a reaction in which a hydroxo or an “ol” bridge M-OH-M bond is formed between two cations whereas oxolation involves the formation of oxo bridges M-O-M between to metal cations. The “ol” or “oxo” bridges between the two metal atoms lead to the formation of condensed oxide or hydroxide species. Under acid conditions, three-dimensional solid phase networks consisting of extended linear M-O-M chain polymers are fabricated. Inorganic polymerization is believed to occur in three stages during the acid catalyzed condensation: (a) polymerization of monomer units to form particles, (b) particle growth, and (c) particles linking to form chains then solid networks that extend throughout the liquid medium, which thickens it to a gel. The removal of the solvents and appropriate drying techniques are important steps to achieve gel densification. When a solvent evaporates from the gel under atmospheric conditions, the capillary pressure due to the interfacial tension of the solvent puts high stress on the gel network. This leads to considerable shrinkage and fracture of the gel during the drying process. The resulting hard, glassy, and porous product is called a xerogel. When the liquid within the gel is removed above its critical temperature and pressure (hypercritical) in an autoclave, the capillary pressure can be eliminated. The product obtained from this process is referred to as an aerogel. The crystalline nature of the amorphous aerogel was achieved after heat treatment. This transition exhibits crystallites with high surface areas and unique properties [1].

## 6.1.2 Hydrothermal method.

The hydrothermal technique has been most popular, garnering interest from scientists and technologists of different disciplines, particularly in the last fifteen years. The term hydrothermal is purely of geological origin. It was first used by the British Geologist, Sir Roderick Murchison (1792–1871), to describe the action of water at elevated temperature and pressure in bringing about changes in the earth's crust leading to the formation of various rocks and minerals.

The term hydrothermal usually refers to any heterogeneous reaction in the presence of aqueous solvents or mineralizers under high pressure and temperature conditions to dissolve and recrystallize (recover) materials that are relatively insoluble under ordinary conditions [2].

Fig. 67 shows a conventional autoclave type Tuttle Roy developed for the hydrothermal method [3].



*Fig. 67. Conventional autoclave type Tuttle Roy*

### *6.1.2.1 Water as a reaction medium.*

Water is one of the most important solvents present in nature in abundant amount and has remarkable properties as a reaction medium under hydrothermal conditions. Water shows different characteristics under hydrothermal conditions than that of standard conditions. One of the biggest advantages of using water is the environmental benefit and cheaper than other solvents, and it can act as a catalyst for the formation of desired materials by tuning the temperature and the pressure. It is nontoxic, nonflammable, noncarcinogenic, nonmutagenic, and

thermodynamically stable. Another advantage is that water is very volatile so that it can be removed from the product very easily.

Hydrothermal solvents have different properties at above 100°C and above 1 atm, especially at the critical point. To understand hydrothermal reactions, the properties of the solvent under hydrothermal conditions must be known very well.

In the Fig. 68, the critical point marks the end of liquid-vapor coexistence curve at the critical temperature,  $T_c$ , and pressure,  $P_c$ , in a phase diagram for a pure homogenous substance. A fluid is defined as being supercritical if it is maintained at conditions above its critical temperature and pressure. The properties of supercritical fluids (SCFs) vary depending on the pressure and temperature and frequently described as being intermediate between those of a gas and a liquid. As the temperature increases, the liquid becomes less dense due to thermal expansion, and at the same time, the gas becomes denser. At the critical point, the densities of both phases become the same. The compound is neither liquid nor gas any longer above the critical point, and it becomes a supercritical fluid. After that, the phases of liquid and gas are not distinguishable, and properties of SCF will be between gas and liquid.

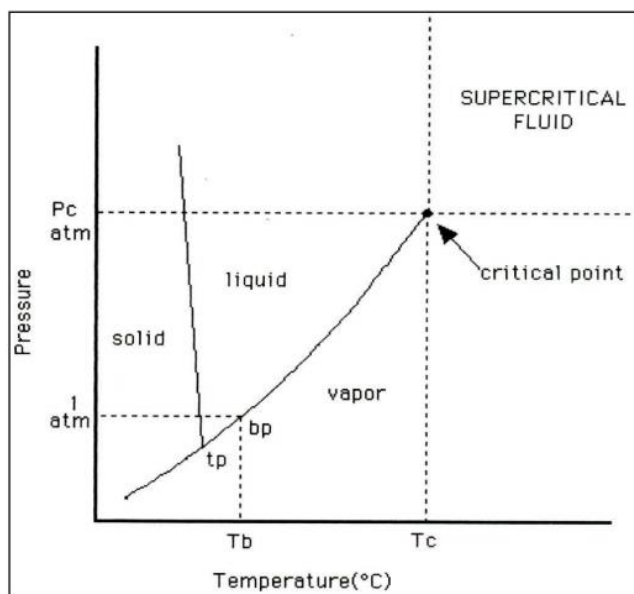


Fig. 68. Phase diagram of water.

Diffusivity and viscosity symbolize transport properties that influence rates of mass transfer. Diffusivity is at least an order of magnitude higher, and viscosity is lower compared with a liquid

solvent. This means that diffusivity of reactants in SCF will occur faster than that in a liquid solvent, which means that solids can dissolve and migrate more rapidly in SCFs. High diffusivity, low viscosity and intermediate density of water increase the rate of the reaction [4].

The dielectric constant that is defined as the ability of a solvent to charge separate increases sharply with the pressure in the compressible region that refers to the area around the critical point in which compressibility is considerably greater than would be forecasted from the ideal gas law. This behavior is also parallel to a change in density, as shown in Fig. 69. Density changes sharply but continuously with pressure in the compressible region. One of the most important advantages of hydrothermal solvents is that a change in density affects the solvating power. A decrease in the density results in a significant change in solvating ability [4].

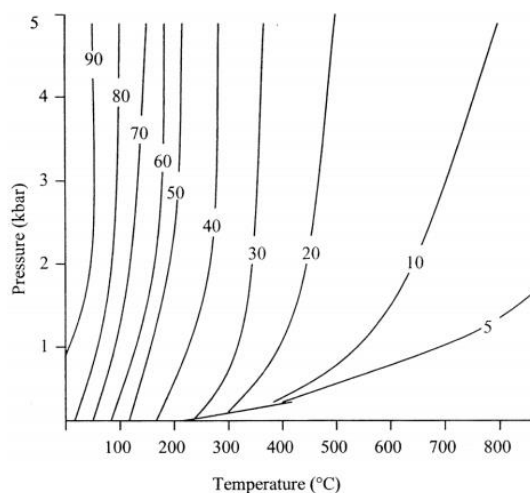


Fig. 69. Variation of the dielectric constant of water with temperature and pressure.

## 6.2 Characterization techniques.

### 6.2.1 X-ray Diffraction.

X-ray powder diffraction (XRD) is a rapid analytical technique primarily used for phase identification of a crystalline material and can provide information on unit cell dimensions. The analyzed material is finely ground, homogenized, and average bulk composition is determined.

Max von Laue, in 1912, discovered that crystalline substances act as three-dimensional diffraction gratings for X-ray wavelengths similar to the spacing of planes in a crystal lattice. X-ray diffraction is now a common technique for the study of crystal structures and atomic spacing.

X-ray diffraction is based on constructive interference of monochromatic X-rays and a crystalline sample. These X-rays are generated by a cathode ray tube, filtered to produce monochromatic radiation, collimated to concentrate, and directed toward the sample. The interaction of the incident rays with the sample produces constructive interference (and a diffracted ray) when conditions satisfy Bragg's Law ( $n\lambda=2d \sin \theta$ ). This law relates the wavelength of electromagnetic radiation to the diffraction angle and the lattice spacing in a crystalline sample. These diffracted X-rays are then detected, processed and counted. By scanning the sample through a range of  $2\theta$  angles, all possible diffraction directions of the lattice should be attained due to the random orientation of the powdered material. Conversion of the diffraction peaks to d-spacings allows identification of the mineral because each mineral has a set of unique d-spacings. Typically, this is achieved by comparison of d-spacings with standard reference patterns

All diffraction methods are based on generation of X-rays in an X-ray tube. These X-rays are directed at the sample, and the diffracted rays are collected. A key component of all diffraction is the angle between the incident and diffracted rays. Powder and single crystal diffraction vary in instrumentation beyond this.

X-ray diffractometers consist of three basic elements: an X-ray tube, a sample holder, and an X-ray detector. X-rays are generated in a cathode ray tube by heating a filament to produce electrons, accelerating the electrons toward a target by applying a voltage, and bombarding the target material with electrons. When electrons have sufficient energy to dislodge inner shell electrons of the target material, characteristic X-ray spectra are produced. These spectra consist

of several components, the most common being  $K_{\alpha}$  and  $K_{\beta}$ .  $K_{\alpha}$  consists, in part, of  $K_{\alpha 1}$  and  $K_{\alpha 2}$ .  $K_{\alpha 1}$  has a slightly shorter wavelength and twice the intensity as  $K_{\alpha 2}$ . The specific wavelengths are characteristic of the target material (Cu, Fe, Mo, Cr). Filtering, by foils or crystal monochromators, is required to produce monochromatic X-rays needed for diffraction.  $K_{\alpha 1}$  and  $K_{\alpha 2}$  are sufficiently close in wavelength such that a weighted average of the two is used. Copper is the most common target material for single-crystal diffraction, with  $\text{Cu}K_{\alpha}$  radiation =  $1.5418\text{\AA}$ . These X-rays are collimated and directed onto the sample. As the sample and detector are rotated, the intensity of the reflected X-rays is recorded. When the geometry of the incident X-rays impinging the sample satisfies the Bragg Equation, constructive interference occurs and a peak in intensity occurs. A detector records and processes this X-ray signal and converts the signal to a count rate which is then output to a device such as a printer or computer monitor [5, 6].

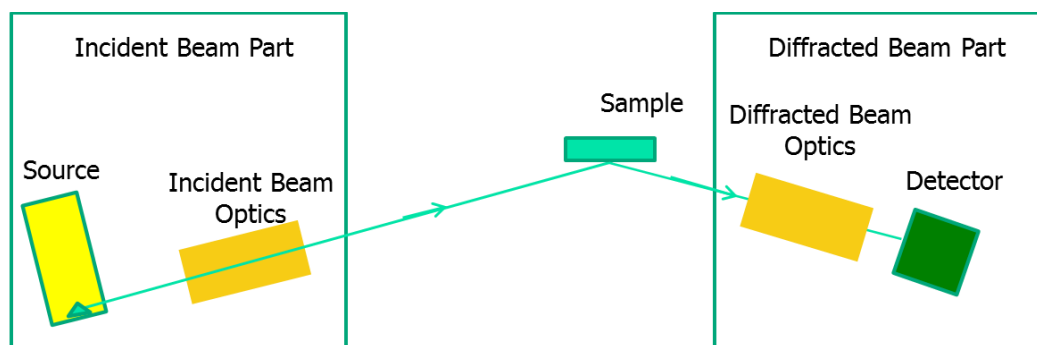


Fig. 70. Schematic diagram of an X-ray diffractometer.

For the powders samples, the analysis was made at room temperature in a PANalytical  $\theta/\theta$  Bragg-Brentano X'pert MDP PRO diffractometer with a radiation of  $\text{Cu-K}\alpha$  ( $\lambda=1.5406\text{ \AA}$ ) and a X'Celerator detector. The diagrams were recorded in a range of 2 theta from  $10^{\circ}$  to  $80^{\circ}$ , see Fig. 71.





*Fig. 71. PANalytical  $\theta/\theta$  Bragg- Brentano X'pert MDP PRO diffractometer for measurements of powders.*

Thin-film measurements were done on a PANalytical diffractometer with a design of low incidence X-ray.



*Fig. 72. PANalytical diffractometer with a design of low incidence X-ray.*

## 6.2.2 BET surface area analysis.

### 6.2.2.1 Adsorption.

Similar to surface tension, adsorption is a consequence of surface energy. Most atoms that make up a solid are bound on all sides by other atoms in the bulk of the solid. The atoms on the surface of the solid, however, are incompletely bound. Due to van der Waals forces of interaction, these surface atoms are more reactive and they attract gas, vapor, and liquids to satisfy the imbalance of atomic forces.

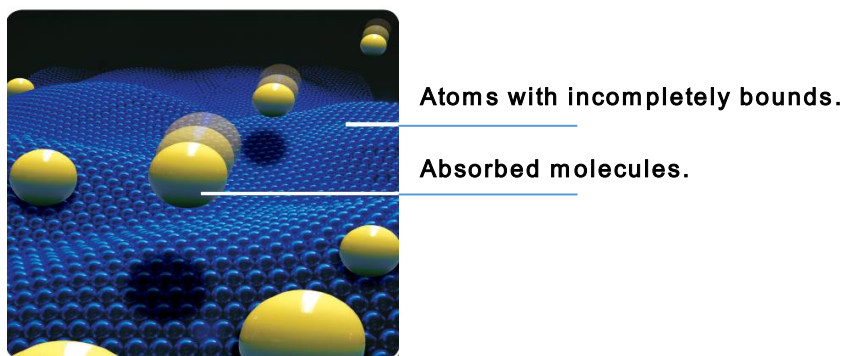


*Fig. 73. Molecules on the surface (in blue) are experiencing a bond deficiency, thus it is energetically favorable for them to adsorb molecules (in yellow).*

### 6.2.2.2 Surface analysis.

Surface area helps determine such things as how solids burn, dissolve, and react with other materials. To determine the surface area, solid samples are pretreated by applying some combination of heat, vacuum, and/or flowing gas to remove adsorbed contaminants acquired (typically water and carbon dioxide) from atmospheric exposure. The solid is then cooled, under vacuum, usually to cryogenic temperature (77 K,  $-195^{\circ}\text{C}$ ). An adsorptive (typically nitrogen) is dosed to the solid in controlled increments. After each dose of adsorptive, the pressure is allowed to equilibrate and the quantity adsorbed is calculated. The quantity adsorbed at each pressure (and temperature) defines an adsorption isotherm, from which the quantity of gas required to form a monolayer over the external surface of the solid is determined. With the area covered by each adsorbed gas molecule known, the surface area can be calculated.

### 6.2.2.3 Porosity, pore size and pore distributions.

Surface area determinations involve creating the conditions required to adsorb and average monolayer of molecules onto a simple. By extending this process so that the gas is allowed to condense in the pores, the sample's fine pore structure can be evaluated. As pressure increases, the gas condenses first in the pores with the smallest dimensions. The pressure is increased until saturation is reached, at which time all pores are filled with liquid. The adsorptive gas pressure then is reduced incrementally, evaporating the condensed gas from the system. Evaluation of the adsorption and desorption branches of these isotherms and the hysteresis between them reveals information about the size, volume, and area [7].

The steps for surface area measurements, porosity, pore size and pore distributions are described in the Fig. 74.



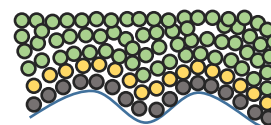
**Stage 1.**  
Isolated sites on the simple surface begin to adsorb gas molecules at low pressure.



**Stage 2.**  
As gas pressure increases, coverage of adsorbed molecules increases to form a monolayer (one molecule thick).



**Stage 3.**  
Further increasing gas pressure will cause the beginning of multi-layer coverage. Smaller pores in the sample will fill first. BET equation is used to calculate the surface area.



**Stage 4.**  
A further increase in the gas pressure will cause complete coverage of the simple and fill all the pore. The BJH calculation can be used to determine pore diameter, volume and distribution.

*Fig. 74. Working steps of the BET equipment.*

The particle size was determined according to

$$D = \frac{6000}{S_{BET} * \rho}$$

Equation 21

Where it assumes that all the particles are spherical with the same size [8-11].

### 6.2.3 Atomic force microscope.

An atomic force microscope is a type of high-resolution scanning probe microscope that has a resolution that you can measure in fractions of a nanometer. It was pioneered in 1986 by Nobel Prize Winner Gerd Binnig along with Calvin Quate and Christoph Gerber.[12].

One of the most important tools for imaging on the nanometer scale, Atomic Force Microscopy uses a cantilever with a sharp probe that scans the surface of the specimen. When the tip of the probe travels near to a surface, the forces between the tip and sample deflect the cantilever according to Hooke's law. Atomic force microscopy will measure a number of different forces depending on the situation and the sample that you want to measure. As well as the forces, other microscopes can include a probe that performs more specialized measurements, such as temperature. The force deflects the cantilever, and this changes the reflection of a laser beam that shines on the top surface of the cantilever onto an array of photodiodes. The variation of the laser beam is a measure of the applied forces.

There are two primary modes of operation for an atomic force microscope, namely contact mode and non-contact mode depending on whether the cantilever vibrates during the operation. In contact mode, the cantilever drags across the sample surface, and it uses the deflection of the cantilever to measure the contours of the surface. To eliminate the noise and drift that can affect a static signal, low stiffness cantilevers are used, but this allows strong attractive forces to pull the tip to the surface. To eliminate this attraction, the tip is in contact with the surface where the overall force is repulsive.

In non-contact mode, the tip vibrates slightly above its resonance frequency and does not contact the surface of the sample. Any long range forces, like van der Waals forces, decreases the resonant frequency of the cantilever.

A feedback loop system helps to maintain the oscillation amplitude constant by changing the distance from the tip to the sample. Recording the distance between the tip and sample at each point allows the software to construct a topographic image of the sample surface.

Most samples will form a layer of moisture on the surface if stored at ambient conditions, and this can make it difficult to measure the sample accurately.

If the probe tip is close enough to detect the short-range forces then it is close enough to stick to the moisture. One way around this is tapping, or dynamic contact mode.

In tapping mode, the cantilever uses a piezoelectric element mounted on the top to oscillate it at near to its resonance frequency with an amplitude of up to 200nm. The forces cause the amplitude to decrease as the tip gets close to the surface, and the height of the cantilever adjusts to keep the amplitude constant. This tapping results in less damage to the sample than contact mode and is more accurate than non-contact mode when moisture is present in a sample [13].

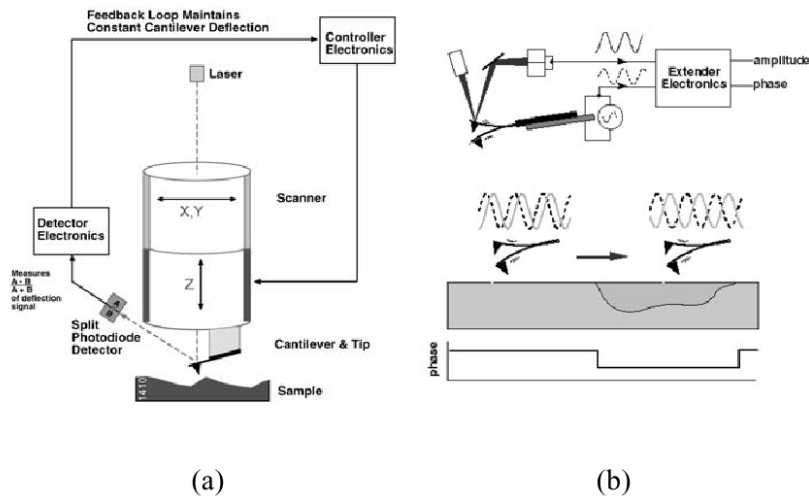


Fig. 75. Schematic representation of the AFM, a) contact mode and b) tapping mode

## 6.2.4 Electron Paramagnetic Resonance.

Electron Paramagnetic Resonance (EPR), sometimes referred to as Electron Spin Resonance (ESR), is a widely used spectroscopic technique to study paramagnetic centers on various oxide surfaces.

Diamagnetic oxide materials can also be studied using suitable paramagnetic probes, including nitroxides and transition metal ions. These observable paramagnetic centers may include surface defects, inorganic or organic radicals, metal cations or supported metal complexes and clusters. Each of these paramagnetic species will produce a characteristic EPR signature with well defined spin Hamiltonian parameters. However, the magnetic properties, stability and reactivity of these centers may vary dramatically depending on the nature of the support or the measurement conditions. In some case, radicals stable on one surface may be transient on another, while variations in the EPR spectra of these radicals may be observed simply by altering the pretreatment conditions of the support. Furthermore, the spin Hamiltonian parameters for a particular paramagnetic species may vary greatly from one support to another. A number of “external” perturbations, such as the specific location of the species on a surface, the presence of other interaction species in the catalytic system, the size of the metal particles, and so on, can alter the spin Hamiltonian parameters, resulting in a significantly modified EPR profile.

Finally, the accurate analysis of the experimental spectrum can only be achieved by simulation and the resulting spin Hamiltonian parameters can then be compared to values obtained by theoretical treatments.

### 6.2.4.1 The electron Zeeman Interaction.

The electron is a negatively charged particle which possesses orbital angular momentum as it moves around the nucleus. The electron also possesses spin angular momentum  $S$  as it spins about its own axis. The magnitude of  $S$  is given by

$$S = \left(\frac{h}{2\pi}\right)[S(S + 1)]^{1/2}$$

Equation 22

where  $S$  = the spin quantum number and  $h$  = Planck ' s constant. By restricting the dimension to one specified direction, usually assigned the  $z$  direction, then the component of the spin angular momentum can only assume two values

$$S = M_s h / 2\pi \quad \text{Equation 23}$$

The term  $M_s$  can have  $(2S + 1)$  different values:  $+S, (S - 1), (S - 2)$  and so on. If the possible values of  $M_s$  differ by one and range from  $-S$  to  $+S$  then the only two possible values for  $M_s$  are  $+1/2$  and  $-1/2$  for a single unpaired electron.

The most important physical consequence of the electron spin is the associated magnetic moment,  $\mu_e$ . This magnetic moment is directly proportional to the spin angular momentum and one may therefore write

$$\mu_e = -g_e \mu_B S \quad \text{Equation 24}$$

The negative sign arises from the fact that the magnetic momentum of the electron is collinear but antiparallel to the spin itself. The factor  $(g_e \mu_B)$  is referred to as the magnetogyric ratio and is composed of two important factors. The Bohr magneton,  $\mu_B$ , is the magnetic moment for one unit of quantum mechanical angular momentum:

$$\mu_B = \frac{e\hbar}{2m_e} \quad \text{Equation 25}$$

where  $e$  is the electron charge,  $m_e$  is the electron mass and  $\hbar = h / 2\pi$ . The factor,  $g_e$ , is known as the free electron  $g$ -factor with a value of 2.002319304386.

This magnetic moment interacts with the applied magnetic field. In classical terms the energy of the interaction between the magnetic moment ( $\mu$ ) and the field ( $B$ ) is described by

$$E = -\mu \cdot B \quad \text{Equation 26}$$

For a quantum mechanical system one must replace  $\mu$  by the corresponding operator, giving the following simple spin Hamiltonian for a free electron in a magnetic field:

$$\hat{H} = g_e \mu_B \mathbf{S} \cdot \mathbf{B} \quad \text{Equation 27}$$

If the field is defined along the z-direction, then the scalar product simplifies to the following Hamiltonian:

$$\hat{H} = g_e \mu_B S_z \cdot B \quad \text{Equation 28}$$

The  $S_z$  value in the above equation can then be replaced by  $M_s$  (in quantum mechanical terms the only operator in the right-hand term above is  $S_z$ ), giving

$$E = g_e \mu_B B M_s \quad \text{Equation 29}$$

Since  $M_s = \pm 1/2$  only two energy states are available, which are degenerate in the absence of a magnetic field, but as  $B$  increases this degeneracy is lifted linearly as illustrated in . The separation of the two levels can be matched to a quantum of radiation through the Bohr frequency condition:

$$\Delta E = h\nu = g\mu_B B \quad \text{Equation 30}$$

The existence of two Zeeman levels, and the possibility of inducing transitions from the lower energy level to the higher energy level is the very basis of EPR spectroscopy [14].

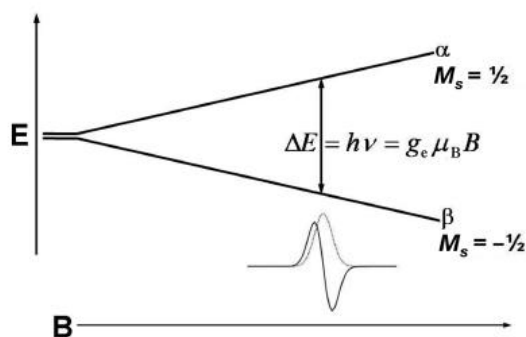


Fig. 76 Energy levels for an electron spin ( $S=\pm 1/2$ ) in an applied magnetic field  $B$ .



The experiments were carried out on Bruker EMX equipped with a X-band (9.5 GHz) and a cryostat from Oxford Instruments for low-temperature measurements. The EPR spectra were recorded by using modulation frequency of 100 kHz, 1 Gauss for modulation field and microwave power about 10 mW. The choice of these parameters satisfies the requirement to prevent any line shape distortion and allows resolving all the spectral details due to anisotropy of the paramagnetic ions environments and to the hyperfine structure from nuclear spins of copper ions ( $3/2$ ) or silver ( $1/2$ ). Irradiation experiments were also carried out under UV from (Xe) lamp with nominal power of 200W dedicated to reveal photoinduced charge transfer which modifies the oxidation state of titanium ions.



*Fig. 77. EPR equipment, Bruker EMX.*

## 6.2.5 Raman spectroscopy.

When a laser is used to probe a sample, light impinges upon a molecule and interacts with the electron cloud of the bonds of that molecule. When light is scattered from a molecule most photons are elastically scattered (Rayleigh scatter), meaning that the scattered photons have the same energy (frequency) and, therefore, wavelength, as the incident photons and no change in the molecular status of the molecule is observed. However, a small fraction of light (approximately 1 in  $10^7$  photons) is scattered at optical frequencies different from, and usually lower than, the frequency of the incident photons. The process leading to this inelastic scatter is termed the Raman effect. In quantum mechanics the scattering is described as an excitation to a virtual state lower in energy than a real electronic transition with nearly coincident de-excitation and a change in vibrational energy. The scattering event occurs in  $10^{-14}$  seconds or less. The difference in the energy level between the excited and ground level are shown in Fig. 78. At room temperature the thermal population of vibrational excited states is low, although not zero. Therefore, the initial state is the ground state, and the scattered photon will have lower energy (longer wavelength) than the exciting photon. Since more photons undergo Stokes scatter, this Stokes shift is what is usually observed in Raman spectroscopy.

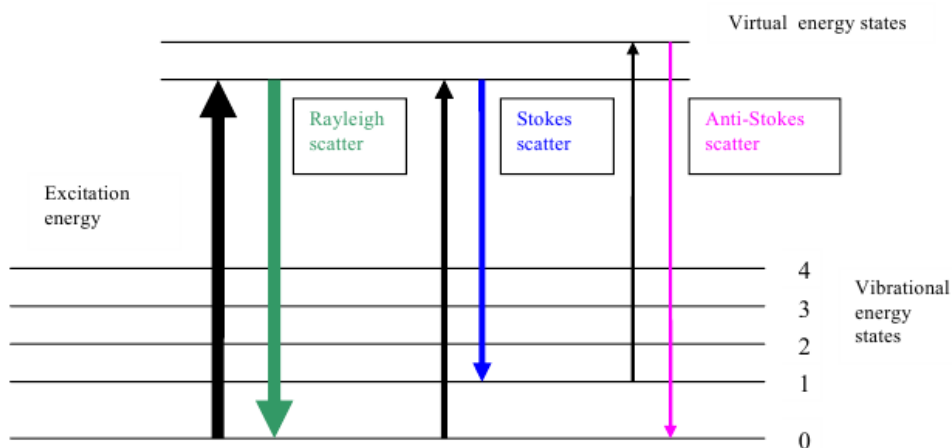


Fig. 78. Scattering events occurring in an excited material.

According to the law of conservation of energy, the change in energy between the incident photon ( $h\nu_0$ ) and the scattered photon ( $h\nu_s$ ) corresponds to the energy change of the molecule, which

refers to the transition between two vibrational states, the initial ( $h\nu_i$ ) and the final excited state ( $h\nu_f$ ) according to the equation:

$$h\nu_0 - h\nu_s = h\nu_f - h\nu_i \quad \text{Equation 31}$$

where  $h$  is the constant of Planck and  $\nu$  is the frequency of the electromagnetic wave. Therefore the change in the vibrational status of the molecule ( $\Delta E_{f-i}$ ) can be expressed as:

$$\Delta E_{f-i} = h(\nu_0 - \nu_s) \quad \text{Equation 32}$$

If in Equation 32 we substitute the definition of frequency with the number of waves in the distance light travels in one second, where  $c$  is the velocity of light and  $\lambda$  is the wavelength of the radiation, we find that

$$\Delta E_{f-i} = h\left(\frac{c}{\lambda_0} - \frac{c}{\lambda_s}\right) \quad \text{Equation 33}$$

and since  $c$  is constant and  $h$  is constant, the change in the difference of energy can be expressed in terms of the reciprocal of the wavelength, whose dimension is  $\text{cm}^{-1}$ , and it is denominated the wavenumber, this is the normal unit used both in Raman and Infrared spectroscopy [15].

The Raman experiments were carried out on XploRA (Jobin-Yvon-Horiba) at room temperature under microscope Olympus with a magnification 50X and using the laser radiation (532 nm) as the excitation source with a nominal power at the sample of about 1.24 mW, Fig. 79.

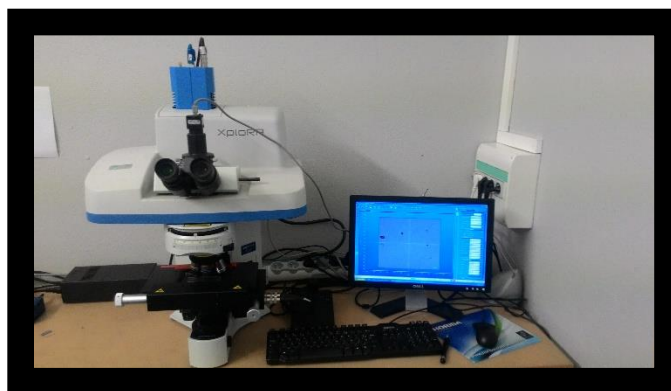


Fig. 79. Raman spectroscopy equipment XploRA (Jobin-Yvon-Horiba).

## 6.2.6 Diffuse reflectance spectroscopy.

An Ocean Optics HR2000 spectrometer with a D<sub>2</sub>/halogen light source and reflection probe to investigate the optical reflectance and absorbance of TiO<sub>2</sub>. The reflection probe measures the diffuse reflectance (light scattered to all angles) as a function of wavelength in a close approximation to the signal obtained from an Integrating Sphere system.

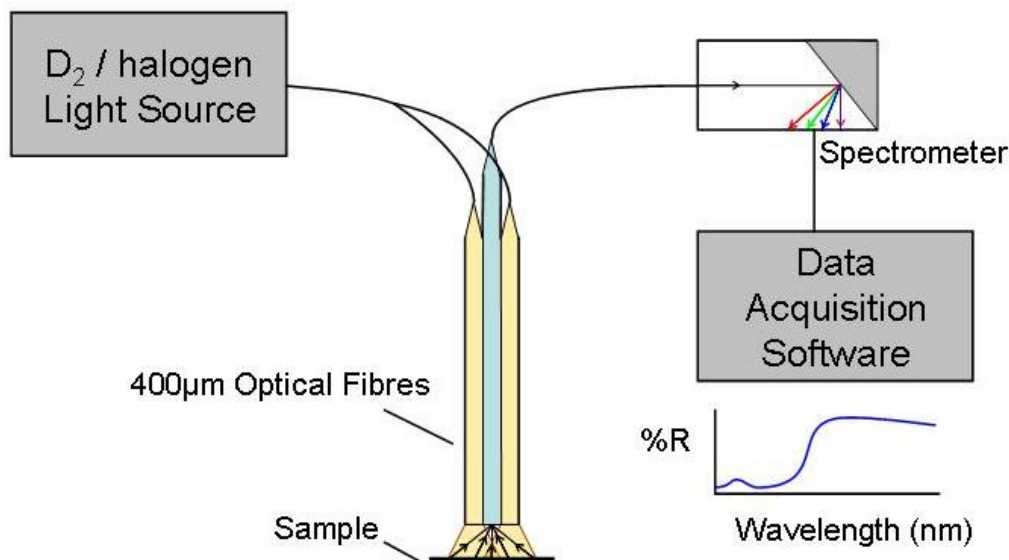


Fig. 80. Schematic diagram of UV-vis diffuse reflectance measurement system.

The Kubelka-Munk function,  $F(R)$ , allows the optical absorbance of a sample to be approximated from its reflectance:

$$F(R) = \frac{(1 - R)^2}{2R} \quad \text{Equation 34}$$

For a semiconductor sample this allows the construction of a Tauc Plot -  $(F(R) \cdot hv)^n$  vs  $hv$ . For a direct band gap semiconductor the plot  $n=1/2$  will show a linear Tauc Region just above the optical absorption edge. Extrapolation of this line to the photon energy axis yields the semiconductor band gap a key indicator of its light harvesting efficiency under solar illumination. Indirect band gap materials show a Tauc Region on the  $n = 2$  plot [16].

Optical reflectance measurements was realized on powders samples by using Micropack DH-2000-Bal UV-VIS-NIR light source and an Ocean Optics HR4000 spectrophotometer.

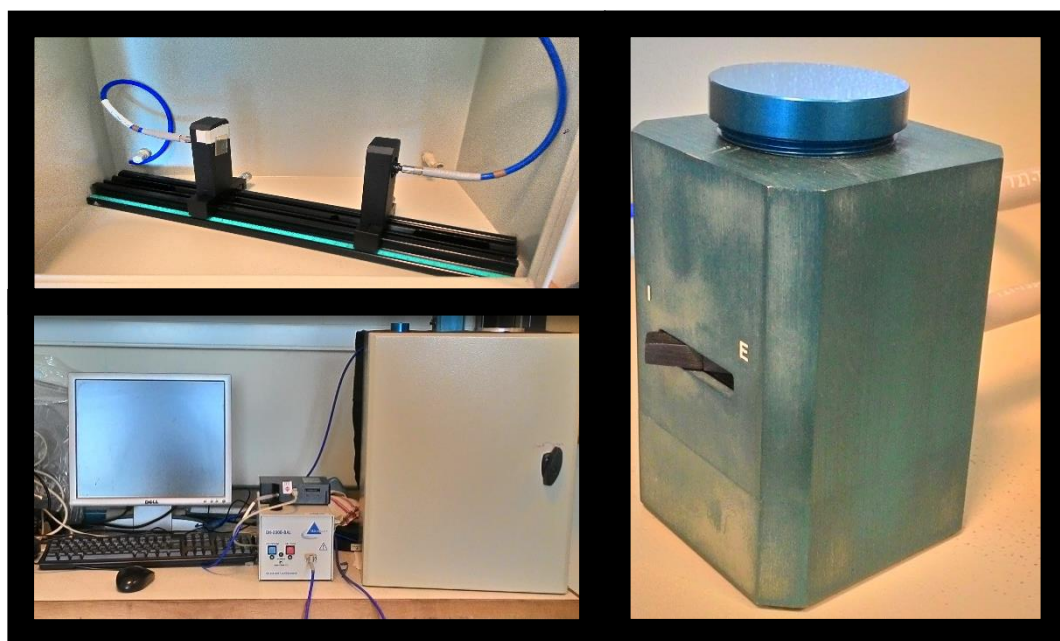


*Fig. 81. UV-Vis spectrometer Ocean Optics HR4000.*

### 6.2.7 Photocatalysis test.

The measurements of the photoactive properties of the metal doped  $\text{TiO}_2$  powders were carried out through a heterogeneous catalysis process which consists in photoinduced degradation of organic dyes such as methylene blue (MB) in solutions. In this aim, an Oriel Xenon Lamp (200 W) was used as light source without a UV-cut off filter, and a near UV-Vis absorption spectrophotometer (Ulice Optronique) working in the spectral range 350 - 900 nm used to monitor the kinetic of MB concentration change under irradiation. A precise calibration of the photocatalysis setup was carried out in order to define the working parameters and mainly the light power per unit surface of the sample which was fixed to  $120 \text{ mW}\cdot\text{cm}^{-2}$ .

In a 25 ml Baker, 20 ml of  $2 \times 10^{-5} \text{ M}$  of methylene blue solution were added. Then 20 mg of powder of  $\text{TiO}_2$  were added to the solution. A magnetic stirring were employed during the test.

It has been agreed that the expression for the rate of degradation of dyes with irradiated TiO<sub>2</sub> follows the Langmuir –Hinshelwood (L-H) law of heterogeneous photocatalytic reactions. According to L-H model, when initial concentration C<sub>0</sub> (ppm) is very small the following pseudo-first order rate equation is followed

$$\ln \frac{C}{C_0} = -kt \quad \text{Equation 35}$$

where k is pseudo- first order rate constant (hr<sup>-1</sup>) and t is time (hr). A plot of ln (C/C<sub>0</sub>) versus time represents a straight line, the slope of which upon linear regression equals the pseudo-first order rate constant k (hr<sup>-1</sup>) [17].

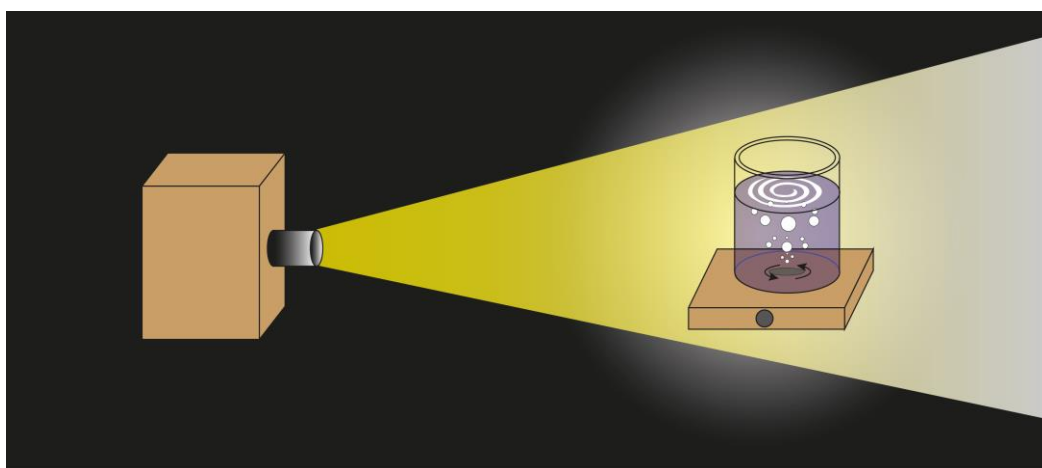


Fig. 82. Illustration of the photocatalysis test design-

### 6.3 Bibliography.

1. Prakash, T., *Review on nanostructured semiconductors for dye sensitized solar cells*. Electronic Materials Letters, 2012. **8**(3): p. 231-243.
2. Byrappa, K. and M. Yoshimura, *Hydrothermal Technology Principles and Applications*, in *Handbook of Hydrothermal Technology (Second Edition)*, K. Byrappa and M. Yoshimura, Editors. 2013, William Andrew Publishing: Oxford. p. 1-49.
3. Margarita, G.H., *SISTEMAS LUMINISCENTES DE POLVOS Y PELICULAS NANOESTRUCTURADOS DE BaTiO<sub>3</sub>:Ln (Ln=Eu<sup>3+</sup>, Er<sup>3+</sup>, Yb<sup>3+</sup>) PREPARADOS POR METODOS DE QUIMICA SUAVE*. 2009, Centro de Investigación en ciencia aplicada y tecnología avanzada. p. 228.
4. Tawde, D.V., *Structural and optical studies of cerium doped lead tungstate nano phosphor*, in *Physics*. 2012, Maharaja Sayajirao University of Baroda.
5. Dutrow, B.L. and C.M. Clark. *X-Ray Powder Diffraction*. 2017; Available from: [http://serc.carleton.edu/research\\_education/geochemsheets/techniques/XRD.html](http://serc.carleton.edu/research_education/geochemsheets/techniques/XRD.html).
6. Gurao, A.G.a.N., *X-ray Diffraction: Principles and Practice*, in *Department of Materials Science and Engineering*. Indian Institute of Technology Kanpur.
7. Corporation, M.I., *Gas adsorption Theory*. 2017.
8. Jena, A. and K. Gupta, *A novel technique for surface area and particle size determination of components of fuel cells and batteries*. New York, NY: Porous Material Inc, 2000.
9. Thiele, G., M. Poston, and R. Brown, *A case study in sizing nanoparticles*. Micromeritics Analytical Services, 2010. **1**.
10. Raj, K. and B. Viswanathan, *Effect of surface area, pore volume and particle size of P25 titania on the phase transformation of anatase to rutile*. 2009.
11. Jiqiao, L. and H. Baiyun, *Particle size characterization of ultrafine tungsten powder*. International Journal of Refractory Metals and Hard Materials, 2001. **19**(2): p. 89-99.
12. Binnig, G., H. Rohrer, C. Gerber, and E. Weibel, *Surface Studies by Scanning Tunneling Microscopy*. Physical Review Letters, 1982. **49**(1): p. 57-61.
13. Master, M. *The Atomic Force Microscope*. 2017 [cited 2017; Available from: <http://www.microscopemaster.com/atomic-force-microscope.html>].
14. Murphy, D.M., *EPR (Electron Paramagnetic Resonance) Spectroscopy of Polycrystalline Oxide Systems*, in *Metal Oxide Catalysis*. 2009, Wiley-VCH Verlag GmbH & Co. KGaA. p. 1-50.
15. Codrich, D., *Applications and limits of raman spectroscopy in the study of colonic and pulmonary malformations*. 2008.
16. ASCG, *Uv-vis Spectrometry*. University of Cambridge.
17. Kumar, J. and A. Bansal. *Photocatalytic Degradation of Amaranth Dye in Aqueous Solution Using Sol-gel Coated Cotton Fabric*. in *Proceedings of the World Congress on Engineering and Computer Science*. 2010.